NONSTEADY CRACK PROPAGATION AND CRAZE BEHAVIOR IN PMMA

Thesis by

Guillermo C. Pulos

In Partial Fulfillment of the Requirements

for the Degree of

Doctor of Philosophy

California Institute of Technology

Pasadena, California

1993

(Submitted June 1, 1993)

A las Rafaelas, Guillermos y Leticias de mi vida.

Acknowledgments

I would like to thank Professor Knauss for all his guidance, patience, and understanding; Professor Ravichandran for the use of his equipment; Professor Rosakis for his support; and the other members of my thesis committee, Professors Iwan and Christman, for their comments in reviewing the thesis.

I would also like to acknowledge the support of the E.I. DuPont de Nemours Company through initial contact with Dr. Manuel Panar. I am also grateful for the support of Caltech's Program in Advanced Technologies, which was sponsored by Aerojet General, General Motors and TRW. In addition some support derived during the final stages of research from ONR grant # N00014-91-J-1427, with Dr. Peter Schmidt as the technical monitor as well as NASA Grant # NAG-1-1203, with Dr. Tom Gates as the technical monitor.

I would also like to thank my friends and colleagues Dr. Richard Pfaff, Dr. Carl Schultheisz and Dr. Peter Washabaugh for many helpful as well as enlightening discussions.

Finally, I would like to thank my family for all their love and support. And above all, I thank God for making all this possible.

Abstract

This work is devoted to the study of nonsteady crack propagation under cyclic loading in polymers, specifically PMMA. The first part deals with the delineation of a precision loading facility allowing ultra-precise load or displacement control commensurate with the high resolution measurements of crack tip material response.

A method of determining the advance of crack tip through combined microscope and computer-analyzed observation is presented. In particular, the experimental set up and software development is described by which these measurements are achieved. It is shown that automated crack tip location is possible with a precision of one to two microns, which is amply sufficient for present purposes to make definitive statements about the smoothness or discontinuity of crack propagation.

The craze and crack opening displacements are measured near the free surface of the specimen both under quasi-static step loading and cyclic loading. Eleven craze opening profiles for equal load increments are acquired during a single cycle under fatigue loading. A multi-linear craze stress model is used to match the opening displacements to the measurements. While the primordial thickness can be defined from the Lorentz-Lorenz equation and from the assumption of a constant index of refraction for the quasi-static loading, the effect of load history may prevent such determinations for cyclic loading. The damage accumulated through cyclic deformation reduces the strength of the fibrils in the middle of the craze and produces a drop in the middle of the stress distribution. The craze and crack opening displacement are monitored in connection with a jump-like crack/craze advance constituting 50% of the craze length. The newly-drawn craze fibrils after the jump show mechanical behavior that is different from their behavior before the jump and exhibit no deterioration in their stress-displacement relation.

Table of contents

Acknowledgments iv

Abstract v

Table of contents vi

List of figures x

Introductory Remark xv

I. PRECISION LOADING FACILITY

Abstract I.1

1 ..... Introduction. I.2

2 ..... Miniature Hydraulic Loading Device I.5

2.1 ..... Design Parameters I.7

2.2 ..... Servovalve I.11

2.3 ..... Symmetrical Loading I.12

3 ..... Data Acquisition and Analysis I.14

3.1 ..... Real Time Data Collection I.14

3.1.1 ..... Program Design I.16

3.1.2 ..... Timers and Interrupts I.16

3.1.3 ..... Video Signal and Data Storage I.17

3.2 ..... Secondary Analysis I.18

4 ..... Summary I.19

5 ..... References I.20

Appendix A: Specimen Geometry and Preparation I.22

Appendix B: Transfer Function of a Hydraulic Actuator I.24

Appendix C: Schematic of the Electronic Circuits I.26

II. HIGH RESOLUTION CRACK LENGTH MEASUREMENTS THROUGH COMPUTER VISION

Abstract II.1

1. ..... Introduction II.2

2. ..... Experimental Set-up II.5

2.1 ..... Optical Arrangement II.5

2.2 ..... Illumination II.7

2.3 ..... Data Acquisition and Analysis II.7

2.3.1 ..... Real-time Measurement II.9

2.3.2 ..... Secondary Analysis II.10

3. ..... Crack Growth Analysis II.11

3.1 ..... Crack Length Deviation II.14

3.2 ..... Fourier Analysis II.16

4. ..... Fracture Surface Morphology II.19

4.1 ..... Variable Stress Intensity Factor Experiment II.19

4.2 ..... Constant Stress Intensity Factor Experiment II.22

5. ..... Summary and Conclusions II.32

6. ..... References II.35

III: CRAZE BEHAVIOR IN PMMA: EFFECT OF LOAD HISTORY AND CRAZE DETERIORATION

Abstract III.1

1. ..... Introduction III.2

2. ..... Experimental Set-up III.5

2.1 ..... Optical Configuration III.5

2.2 ..... Data Acquisition III.7

3. Calculation of The Opening Displacement Profiles III.10
3.1 Preliminary Considerations III.10
3.2 Craze Geometry III.12
3.3 Constant Index of Refraction and the Primordial Thickness III.17
3.4 Variable Index of Refraction III.20
4. Stress Calculation III.21
5. Results and Discussion III.30
5.1 Quasi-Static Results III.30
5.1.1 Primordial Thickness III.31
5.1.2 Opening Profiles and Extension Ratios III.33
5.1.3 Stresses III.37
5.1.4 Stress-Displacement Relations and Stress-Extension-ratio Plots III.41
5.2 Results from Fatigue Loading III.45
5.2.1 Primordial Thickness III.46
5.2.2 Opening Profiles III.49
5.2.3 Stresses III.49
5.2.4 Stress-Displacement Relation III.53
5.2.5 Crack Length Record III.53
5.2.6 Damage Accumulation III.56
5.2.7 Surface Morphology III.62
6. Conclusions III.65
7. References III.67
Appendix: Stress-Displacement Relation for an N-segment Linear Craze Stress Distribution III.71

APPENDIX: CLOSED-LOOP CONTROL OF CONSTANT STRESS INTENSITY FACTORS

Abstract A.1

1. ..... Introduction A.2

2. ..... Theory A.5

3. ..... Experimental Results A.13

4. ..... Discussion A.15

5. ..... Other Types of Feedback A.20

6. ..... Conclusions A.22

7. ..... Acknowledgments A.23

8. ..... References A.24

List of figures

I. PRECISION LOADING FACILITY

Figure 1 ... Schematic and photograph of the loading facility. I.6

Figure 2. .. Typical position servo. I.8

Figure 3 ... Standard flow-control servovalves for industrial applications. I.11

Figure 4 ... Arrangement of hydraulic lines for symmetrical loading. I.13

Figure 5 ... Schematic of data collection. I.15

Figure A1. Compact tension geometry and initial crack detail. I.23

Figure B1. Hydraulic actuator. I.24

Figure C1. LVDT signal conditioner. I.27

Figure C2. Load cell signal conditioner. I.28

Figure C3. Combined feedback schematic. I.29

Figure C4. Servoamplifier. I.30

Figure C5. Limit detection. I.31

Figure C6. Servovalve current driver. I.32

II. HIGH RESOLUTION CRACK LENGTH MEASUREMENTS THROUGH COMPUTER VISION

Figure 1 ... Schematic and photograph of the optical arrangement to record the crack length on the surface of the specimen. II.6

Figure 2 ... Schematic of dark-field illumination. II.8

Figure 3 ... Digitized TV frame of the crack tip region. II.12

Figure 4 ... Crack length (a) and (b) crack length deviation records. II.15

Figure 5 ... Magnitude of the Fourier transform of the crack length deviation record. Crack length record was a function of the crack length (a) and a function of the number of cycles (b). II.18

Figure 6 ... Crack length deviation and fracture surface morphology at high stress intensity factors (0.8-1.0 Mpa m1/2). II.20

Figure 7 ... Crack length deviation and fracture surface morphology at high (0.8-1.0 Mpa m1/2) and lower (0.7 Mpa m1/2) stress intensity factors. II.21

Figure 8 ... Fracture surface morphology at a constant stress intensity factor (0.60 Mpa m1/2) and a test frequency of 1 Hz. II.24

Figure 9 ... Fracture surface morphology at a constant stress intensity factor (0.60 Mpa m1/2) and test frequencies of 3.2 Hz and 1 Hz. II.25

Figure 10 . SEM photographs of wegde-shaped regions. II.26

Figure 11 . Fracture surface morphology at a constant stress intensity factor (0.60 Mpa m1/2) and test frequencies of 0.32 Hz and 0.1 Hz. II.27

Figure 12 . Crack length deviation record (a) and the magnitude of its Fourier transform (b). II.30

III: CRAZE BEHAVIOR IN PMMA: EFFECT OF LOAD HISTORY AND CRAZE DETERIORATION

Figure 1 ... Schematic and photograph of the optical arrangement to record the fringe pattern of the craze and crack opening displacements. III.6

Figure 2 ... Digitized TV frame of the craze and crack opening displacements. III.8

Figure 3 ... Reflected optical interference. III.11

Figure 4 ... Craze/Crack schematic. III.13

Figure 5 ... Index of refraction in the craze as a function of the ratio of extrema in the craze to that of the "unloaded" craze. III.18

Figure 6 ... Schematic of the primordial craze. III.19

Figure 7 ... Crack of length 2c embedded in an infinite plate and loaded by 2 pairs of points loads. III.22

Figure 8 ... Elastic plate under far-field tension containing a crack of length 2c with a craze of length s at each crack tip. III.23

Figure 9 ... Discretization of the stress along the craze. III.26

Figure 10 . Profiles and deviations for different number of segments in the craze stress distribution as the craze is unloaded to K_I= 0.339 Mpa m1/2. III.28

Figure 11 . Stress distributions along the craze for different number of linear segments as the craze is unloaded to K_I= 0.339 Mpa m1/2. III.29

Figure 12 . Primordial thicknesses using a constant index of refraction for a static loading and unloading case. III.32

Figure 13 . Primordial thicknesses using a constant index of refraction for a static unloading case. III.33

Figure 14 . Profiles and extension ratios for a static loading and unloading case. III.35

Figure 15 . Profiles and extension ratios for a static unloading case. III.36

Figure 16 . Stress distribution along the craze for a static loading and unloading case. III.38

Figure 17 . Stress distribution along the craze for a static unloading case. III.39

Figure 18 . Stress-displacement relation for a static loading and unloading case. III.42

Figure 19 . Stress-displacement relation for a static unloading case. III.43

Figure 20 . Stress vs. extension ratio for a static loading and unloading case. III.44

Figure 21 . Stress vs. extension ratio for a static unloading case. III.45

Figure 22 . Primordial thicknesses using a constant index of refraction for a fatigue case. III.48

Figure 23 . Opening profiles for a fatigue case. III.50

Figure 24 . Stress distribution along the craze during the loading section of a fatigue cycle. III.51

Figure 25 . Stress distribution along the craze during the unloading section of a fatigue cycle. III.52

Figure 26 . Stress-displacement relation during a fatigue cycle. III.54

Figure 27 . Crack length (a) and crack length deviation (b) records of an experiment where the crack jumped by 20 mm. III.55

Figure 28 . Primordial thicknesses using a constant index of refraction during cycles 1017 (a) and 1202 (b). III.57

Figure 29 . Stress distribution along the craze during the loading section of cycle 1202. III.59

Figure 30 . Stress distribution along the craze during the unloading section of cycle 1202. III.60

Figure 31 . Stress-displacement relation during cycles 1017 (a) and 1202 (b). III.61

Figure 32 . Crack length record (a) and fracture surface morphology (b) of an experiment where the crack jumped by 20 mm. III.63

APPENDIX: CLOSED-LOOP CONTROL OF CONSTANT STRESS INTENSITY FACTORS

Figure 1 ... Comparison of calculated stress intensity factors K_I in a rectangular edge-cracked plate under combined feedback (a) and a tapered edge-cracked plate under load feedback (b) ($\alpha = a / W$). A.10

Figure 2 ... Mixing ratio (R) of load and displacement needed to minimize the variation of the stress intensity factor during crack propagation under combined feedback ($\alpha = a / W$). A.12

Figure 3 ... Experimentally obtained stress intensity factor amplitudes ΔK_I^{exp} for different mixing ratios R under combined feedback ($\alpha = a / W$). A.14

Figure 4 ... Relative deviation of the Stress Intensity Factor over a 5% crack length increase in a rectangular edge-cracked plate under combined feedback. The deviation is plotted versus the mixing ratio (a) and versus the crack length (b) (a =a/W). A.18

Introductory Remark

This doctoral dissertation is organized into 3 separate chapters and an appendix, each containing its own abstract, introduction, conclusion and bibliography. The first chapter is concerned with the design and operation of the loading device that was built and used to conduct the fatigue experiments.

In this second of three chapters on the referenced topic we describe the method of acquiring through computer vision the location of the tip of a crack under (cyclic) loading. These measurements serve to investigate the nonsteady crack propagation behavior of PMMA.

The third chapter describes the measurements of the (internal) crack and craze opening displacements in addition to the optical system used in the observations. A multi-linear stress distribution across the craze is calculated from the opening displacements; a stress-displacement relation is calculated from the stresses and displacements and is used to assess the damage that the craze fibrils sustain during the cyclic loading. These (internal) measurements are made close to the free surface of the specimen, that where the crack length is being recorded simultaneously, and are correlated to the nonsteady crack propagation.

Finally, the appendix describes a novel technique, which is based on the combined feedback of load and displacement, that produces a constant stress intensity factor for the rectangular compact tension geometry.

FIGURE 3.2 The constant states, which are to be used as the initial condition for the Riemann problem at the interface $j + 1/2$ 77

FIGURE 3.3 The geometry of a 2-D computational cell (i, j). 80

FIGURE 3.4 The locus of all points $\mathbf{x}_w$ in the cell (i, j) at time t, which are connected with point $(t + \delta t, \mathbf{x}_p)$ by the 1-D characteristic differential Equation (3.40). 84

FIGURE 4.1 Regular shock reflection. Pressure contour levels at time $t = 5$. . 92

FIGURE 4.2 Regular shock reflection at time $t = 5$. Pressure profile along the line $y = 0.525$. 93

FIGURE 4.3a Double Mach reflection. Density contours at time $t = 0.20$. Low resolution. 94

FIGURE 4.3b Double Mach reflection. Density contours at time $t = 0.20$. High resolution. 94

FIGURE 4.4a Double Mach reflection. Pressure contours at time $t = 0.20$. Low resolution. 95

FIGURE 4.4b Double Mach reflection. Pressure contours at time $t = 0.20$. High resolution. 95

FIGURE 4.5a Inviscid shear layer. Pressure contours at time $t = 1.0$. 96

FIGURE 4.5b Inviscid shear layer. U-velocity contours at time $t = 1.0$. 96

FIGURE 4.5c Inviscid shear layer. Density contours at time $t = 1.0$. 97

FIGURE 4.5d Inviscid shear layer. V-velocity contours at time $t = 1.0$. 97

FIGURE 4.6a Inviscid shear layer. Pressure contours at time $t = 2.0$. 98

FIGURE 4.6b Inviscid shear layer. U-velocity contours at time $t = 2.0$. 98

FIGURE 4.6c Inviscid shear layer. Density contours at time $t = 2.0$. 99

FIGURE 4.6d Inviscid shear layer. V-velocity contours at time $t = 2.0$. 99

FIGURE 4.7a Inviscid shear layer. Pressure contours at time $t = 3.0$. 100

FIGURE 4.7b Inviscid shear layer. U-velocity contours at time $t = 3.0$. 100

FIGURE 4.7c Inviscid shear layer. Density contours at time $t = 3.0$. 101

FIGURE 4.7d Inviscid shear layer. V-velocity contours at time $t = 3.0$. 101

FIGURE 4.8a Inviscid shear layer. Pressure contours at time $t = 4.0$. 102

FIGURE 4.8b Inviscid shear layer. U-velocity contours at time $t = 4.0$. 102

FIGURE 4.8c Inviscid shear layer. Density contours at time $t = 4.0$. 103

FIGURE 4.8d Inviscid shear layer. V-velocity contours at time $t = 4.0$. 103

FIGURE 4.9a Inviscid shear layer. Pressure contours at time $t = 5.0$. 104

FIGURE 4.9b Inviscid shear layer. U-velocity contours at time $t = 5.0$. 104

FIGURE 4.9c Inviscid shear layer. Density contours at time $t = 5.0$. 105

FIGURE 4.9d Inviscid shear layer. V-velocity contours at time $t = 5.0$. 105

I. PRECISION LOADING FACILITY

Abstract

This is the first of three chapters devoted to the study of nonsteady crack propagation under cyclic loading in polymers, specifically PMMA. The first chapter deals with the delineation of a precision loading facility allowing ultra-precise load or displacement control commensurate with the high resolution measurements of crack tip material response.

1 Introduction.

Glassy polymers have become very widely used materials in engineering. Because they are often employed in designs requiring long term sustaining of loads understanding their behavior under such conditions is important. Of particular interest is the relation of the microstructural (craze) behavior of these materials to the more global aspects of failure: A closer association of the molecular/micromechanical performance allows a better assessment of how these materials perform under a variety of load impositions. It is the intent here to contribute to this understanding by studying the history dependent cohesive forces offered by the craze material at the tip of a propagating crack.

In the present context we are primarily concerned with the crack advance under cyclic loading usually associated with the notion of fatigue. While the traditional engineering approach to fatigue design in the presence of crack is to work with the relation of the stress intensity factor to the average crack propagate rate (per cycle) there have been reports [1-3] that the crack does not propagate steadily but in spurts, the time frame of each spurt encompassing possibly many cycles. The question thus arises how the craze participates in this nonsteady behavior: Is the nonsteady "periodicity" associated with a total break down of the craze thus advancing the crack by the length of the craze, or is such periodicity associated with a break down within the craze so that advancement is only partial. Answers to these questions are clearly not obvious inasmuch as a large range of stress intensity loading at the crack/craze tip can generally be encountered in time dependent polymer fracture.

The aim in this study is to gain better knowledge of the underlying material behavior under cyclic loading through detailed observations with the aid of a microscope and optical interferometry. Because the size scale of these observations are at the micron level it is clear that conventional engineering test facilities are inadequately precise to guarantee sufficient

control over the test conditions and that special facilities must be designed and constructed that allow displacement control to the same level of precision as the measurements to be recorded. In addition, there exists the perennial question whether the observations made on the surface of a specimen truly reflect the behavior of the crack front throughout the thickness of the specimen. This latter concern is particularly important when one is concerned with the measurements attempting to distinguish differences at the micron scale. Because many such measurements are likely to be required a method must be found which allows (at least semi)automatic data acquisition in real time in order to reduce the inordinate amount of data reduction otherwise necessary.

We start here with the discussion of how precisely controlled loading conditions can be assured in order to perform correspondingly precise measurements. The objective is to provide displacement control in (a) arbitrarily prescribable time histories to (b) within at least the wave length of light (micron scale). Requirement (a) demands precision control which can only be achieved to this degree in the absence of vibrations. The latter constraint requires essentially that the loading device must be mounted on a vibration isolated optical table which, in turn, places limitations on its physical size. Precision can be readily guaranteed through the use of thermal deformations [4] or through piezzo electric devices [5]. The former are limited in the speed of deformations while the latter are typically limited to small loads. Although hydraulic devices and associated linkages are difficult to control at the tolerances desired here, hydraulics could provide the best overall answer for the present study if special care in the design of the loading device was exercised. All three methods mentioned here are all capable of being computer controlled in real time for prescribing arbitrary load histories. (condition b). It turned out ultimately that the primary histories used were for saw-tooth and sinusoidal loads or deformations. Thus the design ultimately settled on the choice of a computer controlled hydraulic loading device. However, the device needed to be light enough to be provide well defined boundary conditions for the test prescriptions.

In the sequel we delineate the evaluation of the design parameters for the system with special attention focusing on the displacement control in the micron range. Bearing in mind the need for microscope observation of the crack tip loading must be accomplished such that the crack tip does not move appreciably during loading. This feature is discussed in section 2.3 and the interfacing of the computer with real time data acquisition in section 3. The final section summarizes the design, also with a view towards the interaction with the optical interferometry described in the second chapter of this thesis.

2 Miniature Hydraulic Loading Device

This section discusses the design issues relevant to the construction of the loading facility to study the fatigue behavior of PMMA under the microscope. Discussed are the design specifications, the servovalve employed in the loading device and the physical arrangement to obtain symmetrical loading. The schematic and a photograph of the loading device are shown in figure 1. The loading facility is mounted on an optical breadboard to facilitate incorporating the optical components into the set-up.

The loading device consists of a single servovalve to control the position of two cylinders arranged hydraulically in series. A linearly variable differential transformer (LVDT) is attached to the back end of each hydraulic cylinder and serves to monitor its displacement. The range of the LVDTs is ±1.3 mm and they provide an output[1] of approximately 5 mV/μm. An 1100 N load cell attached to the left cylinder measures the load on the specimen and provides an output[2] of approximately 10 mV/N. The load cell resolution is pegged at 0.05N.

Two optical arrangements, each ending in a charge-couple-device (CCD) camera, are used to measure the crack length and the opening displacements of the crack and craze. The optical arrangements as well as the results obtained with them are discussed separately in chapter 2 and 3; section 3 of this chapter considers the output from the CCD cameras in terms of the data collection and storage requirements.

---

[1]The output comes from the signal conditioner that is attached to the LVDT.
[2]The output comes from the signal conditioner that is attached to the load cell.

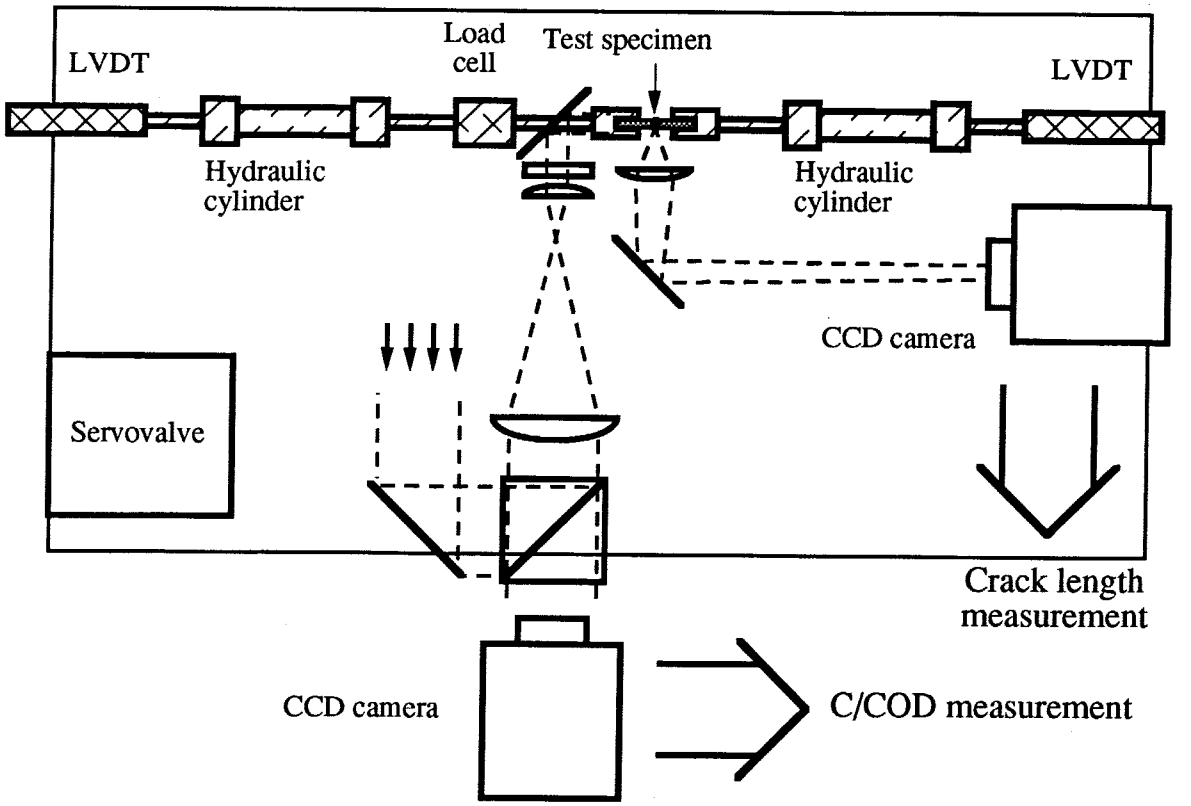

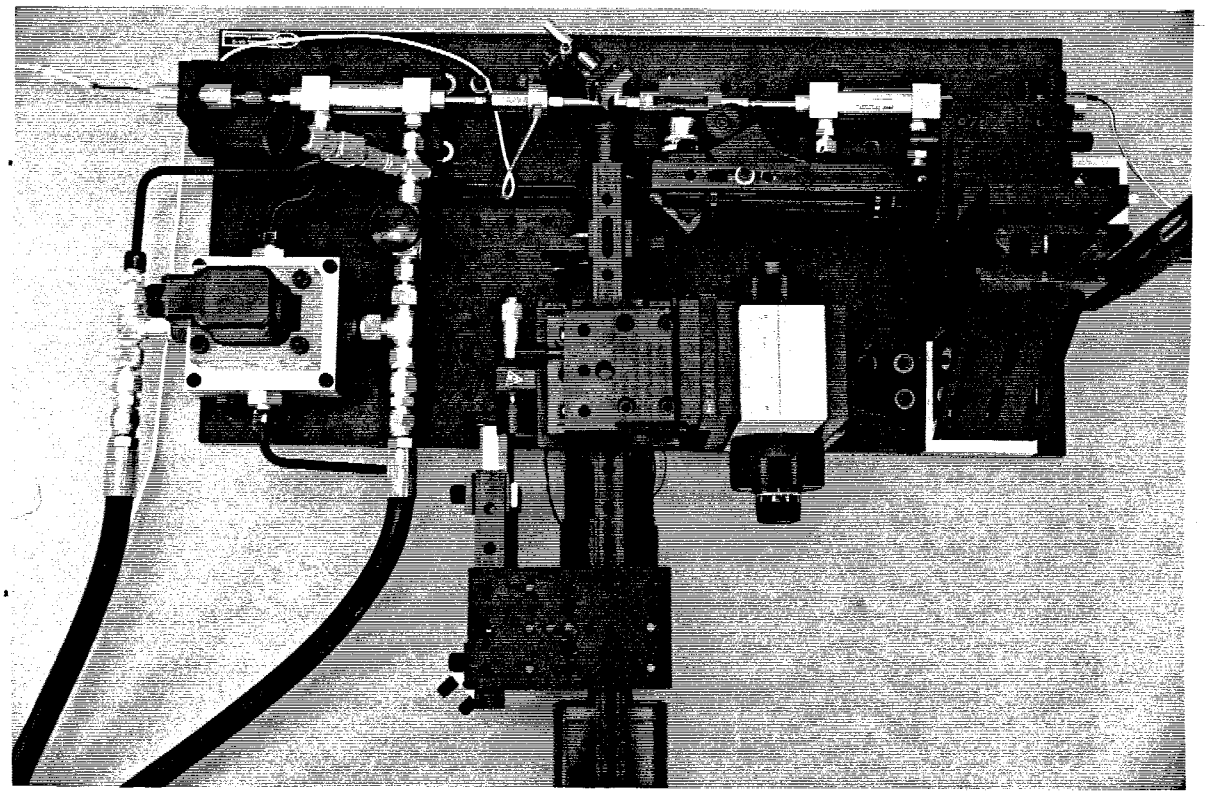

FIGURE 1 Schematic and photograph of the loading facility.

The most important figure of merit and the motivation for the design and construction of this loading device was its positional resolution. In addition, a facility with symmetrical loading was desired in order to retain the crack tip location in approximately the same position during any stage of the deformation cycle; this positioning assures that the microscopic tracking of the crack tip is always within the view of the microscope. The constructed symmetrical loading device has a positional resolution of ± 1 μm, a typical tracking error[3] of 0.5 μm and a typical rms error[4] of 0.4 μm. The rest of this section considers the design parameters, servovalve and the arrangement of the hydraulic lines.

2.1 Design Parameters

The type of valve used for this loading facility is a flow-control[5] servovalve; the relevant servomechanism has positional character. The schematic diagram for a servomechanism with a position transducer (position servo) for feedback is shown in figure 2. There are four essential components: the servoamplifier, the servovalve, the actuator (hydraulic cylinder) and the position transducer which measures the displacement (output variable) to provide the feedback. The position servo tends to make the displacement (output) follow the command signal (input). In order to delineate the degree of measurement refinement, this sub-section discusses the governing equation of the position servo, the expected errors and the factors that affect the performance.

The closed-loop transfer function T [6] for the position servo is:

$$T \equiv \frac{U}{V_C} = \frac{G_{SA}G_{SV}G_A}{1\text{-}H_{FB}G_{SA}G_{SV}G_A} \qquad (1)$$

where G_{SA} transfer function of the servoamplifier (mA/Volts),

G_{SV} transfer function of the servovalve (mm^3/sec/mA),

[3]The deviation (as measured from the LVDTs) from the prescribed (preset) displacement amplitude (at the beggining of the test) in a given period of time; in this case 5000 cycles at a frequency of 1 Hz.
[4]The rms error after the prescribed displacement and the tracking error have been subtracted.
[5]The output of this type of servovalve is a flow rate that is proportional to the current input.

G_A transfer function of the actuator (mm/mm^3/sec)

and H_{FB} transfer function of the position transducer (Volts/mm)
(feedback)

All transfer functions are the Laplace transfer functions, they are expressed as functions of the Laplace variable s.

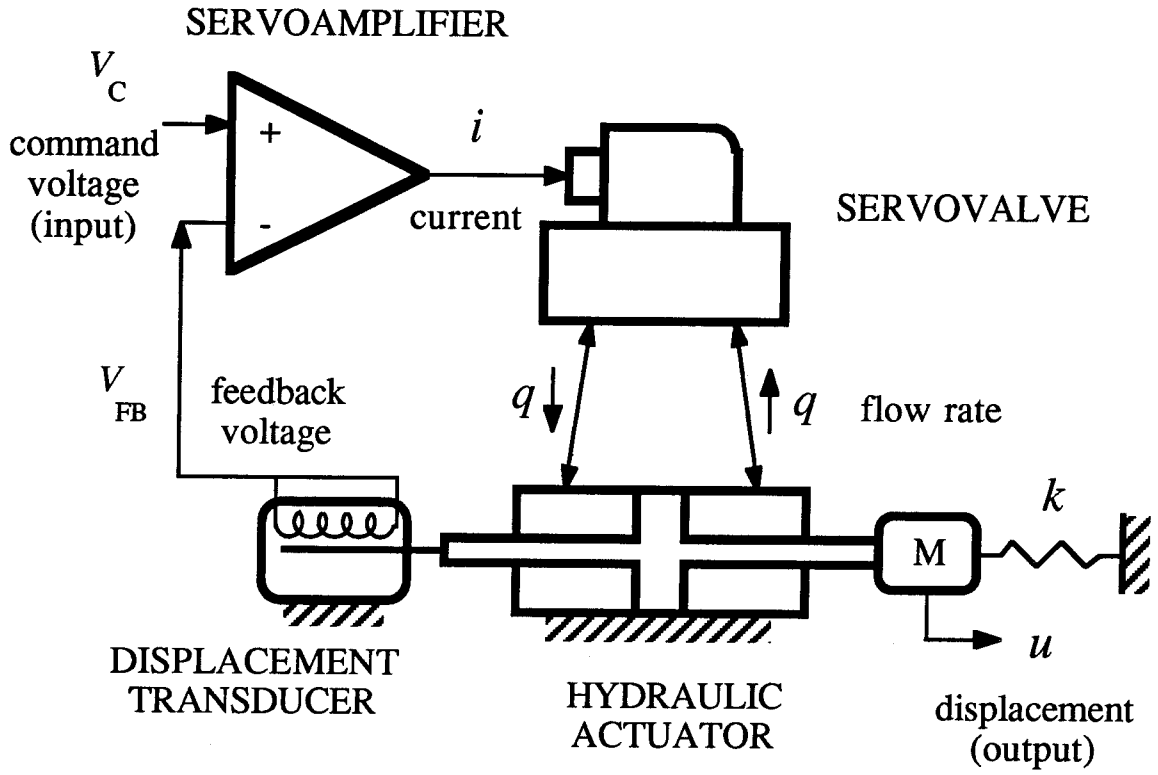

FIGURE 2. Typical position servo.

The transfer function for a flow-control servovalve [7] can be approximated by a second-order oscillator with a d.c. gain of q_R/i_R

$$G_{SV}(s) = \frac{\omega_{SV}^2}{s^2 + 2\zeta_{SV}\omega_{SV}\, s + \omega_{SV}^2} \frac{q_R}{i_R} \qquad (2)$$

where q_R is the rated flow
i_R is the rated current
ζ_{SV} is the servovalve's damping fraction
and ω_{SV} is the servovalve's natural frequency.

The transfer function for the hydraulic actuator is derived in appendix B. Here we show the final result

$$G_A(s) = \frac{\omega_{LR}^2}{s^2 + 2\zeta\omega_{LR}s + \omega_{LR}^2} \frac{k_F}{k_F + k} \frac{1}{As}. \qquad (B.9)$$

The two remaining transfer functions G_A and H_{FB} can also be represented by the same type of transfer function: a second-degree oscillator (or even a first-degree lag $1/(\tau s+1)$) with a constant d.c. gain. Let the d.c. gain of the servoamplifier be G_0 and the d.c. gain of the feedback transfer function be H_0. The transfer functions can be written as

$$G_{SA}=G_0 g(s) \qquad H_{FB}=H_0 h(s) \qquad (3)$$

where $g(s)$ and $h(s)$ are of the form ($g(s)$, $h(s) \rightarrow 1$ as $s \rightarrow 0$)

$$\frac{1}{\tau s + 1} \text{ or } \frac{\omega^2}{s^2 + 2\zeta\omega\, s + \omega^2}. \qquad (4)$$

The product $G_{SA}G_{SV}G_A H_{FB}$ is called the open-loop transfer function, denoted as $GH(s)$. Using the previous equations GH can be expressed as:

$$GH(s) = \frac{K_V}{s\, f(s)} \qquad (5)$$

where $f(s) \rightarrow 1 + k_F/(k_F+k) \approx 1$ $(k<<k_F)$ as $s \rightarrow 0$
and

$$K_V = \frac{G_0 H_0}{i_R} \frac{q_R}{A} = \text{velocity error constant } (\text{sec}^{-1}). \qquad (6)$$

Neal shows [8] that the output stiffness[6] is proportional to K_V while the uncertainty in position output[7]

$$x_u = \frac{q_R / A}{10 K_V} \tag{7}$$

and the steady-state error for a unit ramp input are inversely proportional to the velocity error constant. Thus, by maximizing K_V the stiffness is increased and the errors are reduced. The maximum value that K_V can attain is determined by the open-loop transfer function and while it will depend on the individual transfer functions of its four components one can obtain very useful information if one assumes that one of the four components has a resonant frequency which is well below the others; in that case, that particular component becomes the limiting factor in determining the maximum value that K_V can attain before the system becomes unstable. It can be shown [6] that if one of the components is the limiting factor so that f(s) is the corresponding second-degree oscillator for that component then the maximum value that K_V can attain will be proportional to the resonant frequency of that component. Thus, the lowest resonant frequency becomes the limiting factor in minimizing the positional (equation 7) and "following[8]" errors. Clearly, the lowest frequency will be either the load resonance frequency or the servovalve's since the servoamplifier, which is made up of electronic components, can be made to have extremely high resonant frequencies and the displacement transducer, although a electro-mechanical device, can be made small enough so that its resonant frequency will also be large.

Thus, the path to follow in optimizing the design is to choose components with the highest resonant frequencies and in addition, to consider equations 7, B.5-B.7 which determine the positional uncertainty and the load resonance frequency.

---

[6]The stifness in this context prevents outside forces (noise) from disturbing the system.
[7]This error does not appear in the calculations from a linear system; it is caused entirely by the non-linear characteristics of the servovalve at null.
[8]Another term for the steady-state error when the input is a unit ramp.

2.2 Servovalve

As discussed in the sub-section 2.1, that in order to obtain the best performance of the loading device in terms of positional resolution one should choose the resonant frequency of the servovalve as high as possible. The basis for selecting the servovalve for the loading device was the set of standard flow-control servovalves from Moog™; they are shown in figure 3. The abscissa shows the 90° phase lag frequency which, for the purpose of this discussion, can be considered proportional to the resonant frequency; the ordinate shows the flow-rate capacity of the servovalves.

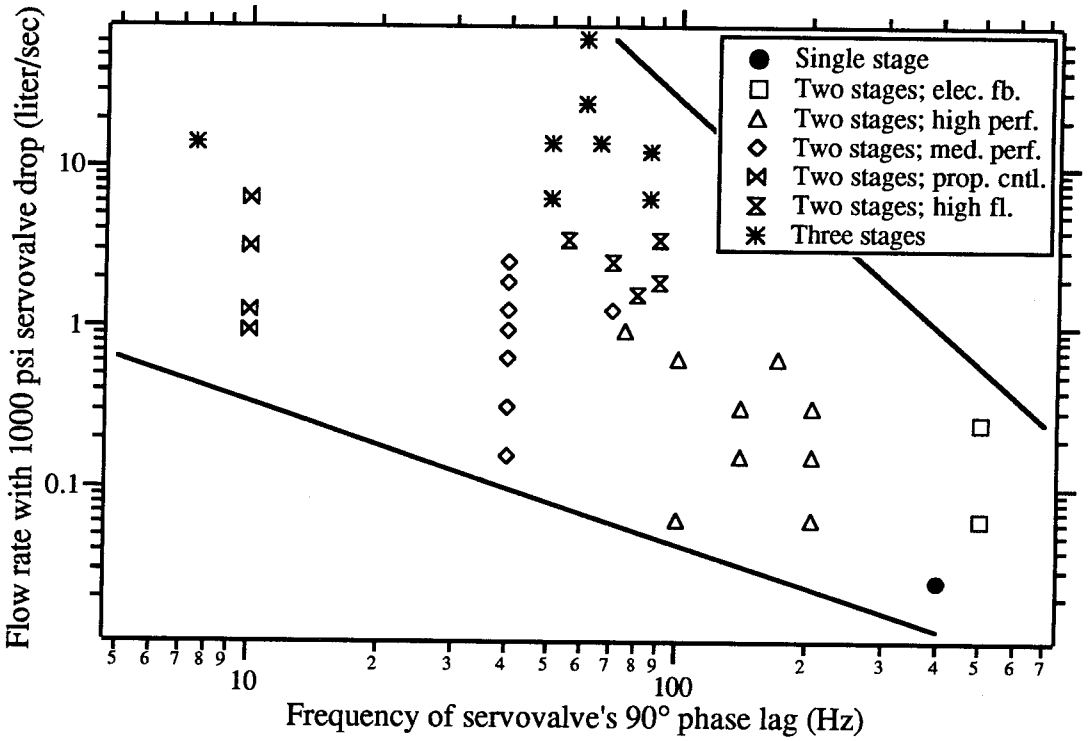

FIGURE 3 Standard flow-control servovalves for industrial applications.

Two choices stand out: the first is the two-stage servovalve with electrical feedback; it has a 90° phase lag of 500 Hz and a flow rate of 0.065 lt/s. The second choice is the single-stage (black dot) 400 Hz 0.025 lt/s servovalve. We opted for the single-stage[9] one since it

[9]For comparison purposes the tension MTS loading device of the Solid Mechanics group at Caltech uses the two-stage 100 Hz 0.65 lt/s with a larger q_R/A.

offers other advantages: The lack of a second stage indicates that there is no spool to cause internal friction. In addition, the smaller flow rate allows the use of smaller cylinders for the same q_R/A; thus, it helps increase the load resonance frequency by reducing the mass of the piston. The main disadvantage in the single-stage design is the wasted flow rate which is almost twice the flow that goes to the cylinders.

2.3 Symmetrical Loading

As pointed out briefly before, the need for symmetrical loading stems from the requirement that the craze and crack remain in focus at any time as the specimen is loaded; thus, due to this symmetry, the optical arrangement which records the fringes of the opening displacements[10] is able to acquire a frame during any portion of the loading cycle. In addition, the crack tip stays within the field of view of the side viewing microscope which tracks its position.

In this particular design, which uses a single servovalve,[11] the symmetric loading is accomplished through the use of double-sided cylinders. This type of cylinder, as it name implies, is designed with a two-sided pressure cavity and a piston protruding at each end; the consequence of this design is that the effective area is the same for both chambers of the cylinder. With this type of cylinder the amount of fluid entering into one chamber (as the piston moves) equals the amount of fluid that exits from the opposite chamber; thus, if one cylinder is connected in series to the second and the connection is filled with an incompressible fluid a displacement of the piston in one cylinder will create an equal displacement in the second.

---

[10]This optical arrangement is the topic of chapter III.

[11]A design that uses two servovalves to control two cyclinders would have the second servovalve controling the second cylinder under a displacement feedback with the command input being the negative of the displacement output of the first cylinder; thus, producing the symmetric loading.

The connection of the cylinders for producing symmetric loading is shown in figure 4. The servovalve controls the direction of the flow by redirecting the flow from the hydraulic supply to either one of two ports which are connected to the cylinders. As the fluid enters into one chamber of a cylinder, the amount of fluid that exits from the opposite chamber is directed into the second cylinder causing an equal amount of displacement in the opposite direction; thus, both cylinders move in opposite direction producing a symmetric loading displacement for the test specimen located in between the cylinders.

The symmetric operation works well, and did so, as long as there is no leakage from the loop. With age of operation that presumption is likely to be violated, but has not caused a major problem in these studies. Also, it should be noted the long tubes connecting the cylinders to the servovalve lower the load resonance frequency.

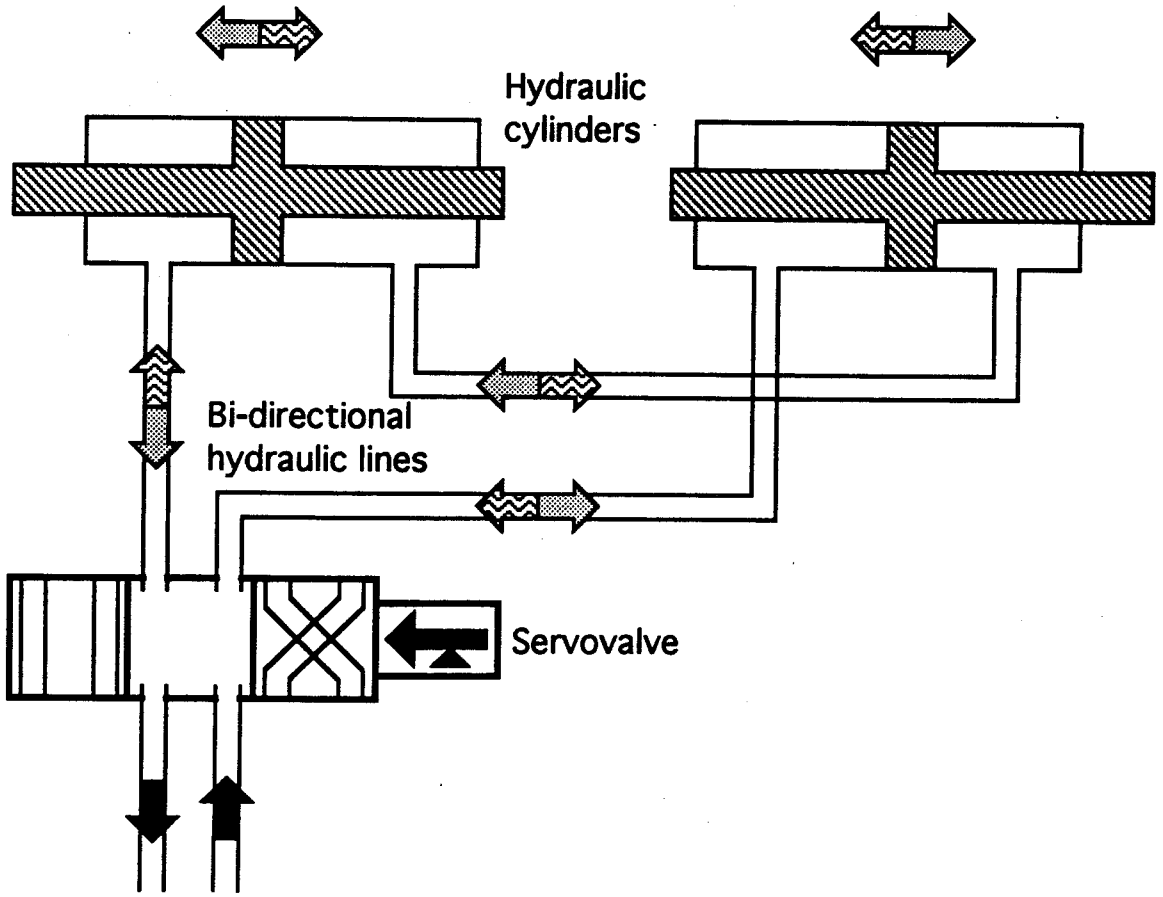

FIGURE 4 Arrangement of hydraulic lines for symmetrical loading.

3 Data Acquisition and Analysis

A PDP 11/73 computer controls the experiment by supplying the command signal to the servomechanism, while it simultaneously records and analyses two different types of information: pictorial information from the CCD cameras attached to the optical systems and one-dimensional information from the signal conditioners (i.e., load and displacements); a schematic of the data collection is shown in figure 5. All of the information is stored into two separate files. After the experiment finishes the stored information is separated into files containing a single type of information and prepared for further analysis and long term storage. The program that collects and analyses information while the experiment is in progress is discussed first.

3.1 Real-time Data Collection

The term "real-time" refers to the type of programming that must accomplish a given set of tasks in a preset amount of time and it differs from regular programming in that the emphasis is in executing and processing as much information as it is possible without exceeding the time constraints instead of processing all of the information without regards to time. In this sub-section are described the data recording while the experiment is in progress and the concepts behind the design philosophy are outlined.

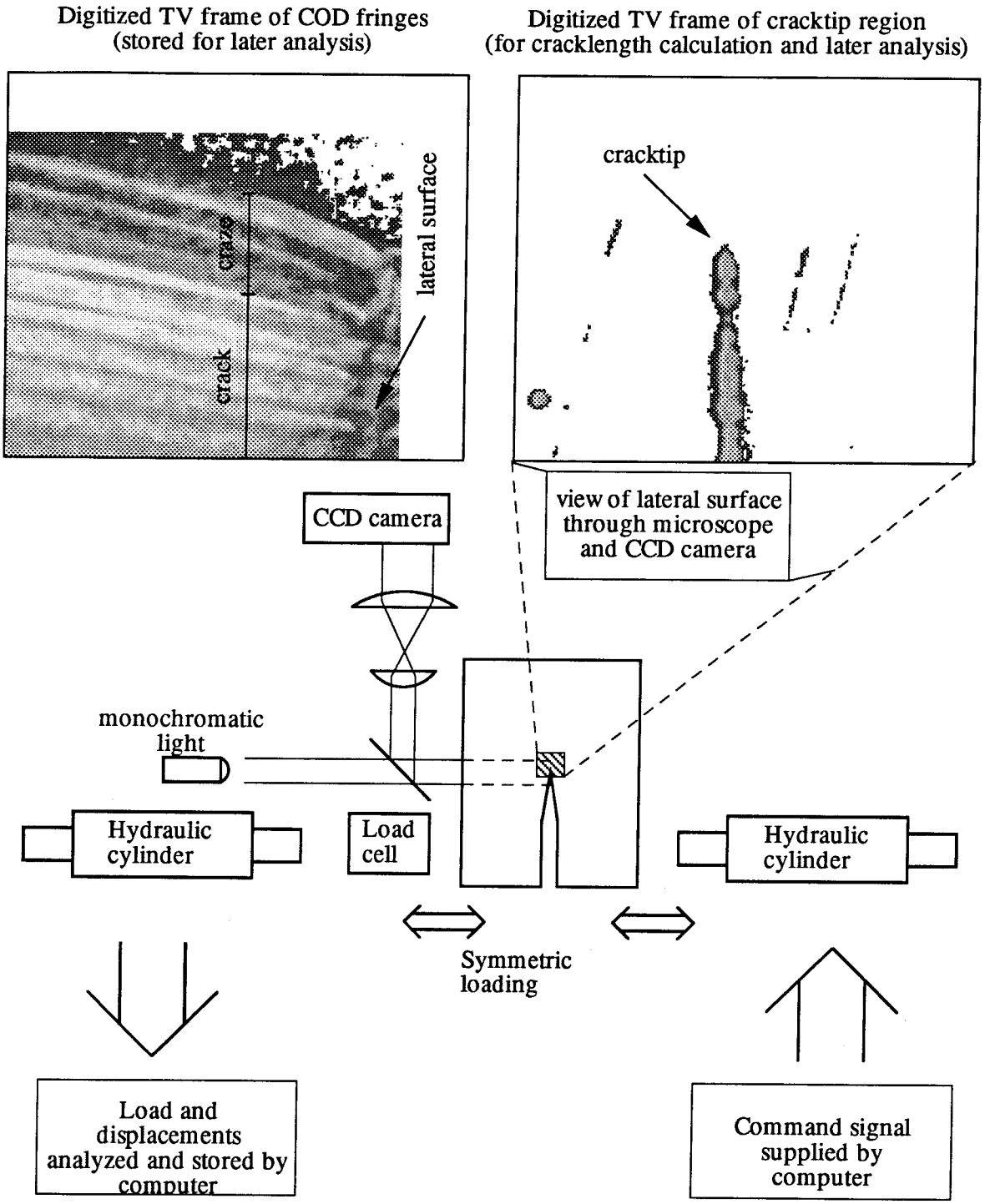

FIGURE 5 Schematic of data collection.

3.1.1 Program Design

The program is designed around the concept of the interrupt routine: a short program or subroutine that can suspend the (main) program in response to a signal (an interrupt) leaving the internal registers unchanged so that the main program can resume its execution at the point that it was suspended without any errors or additional programming considerations. Thus, the main program is simplified and relieved from having to execute tasks at specific times at the expense of writing separately the interrupt routines that handle those tasks.

3.1.2 Timers and Interrupts

The program controlling the experiment and collecting the data uses the interrupt routines to output the command signal through the digital-to-analog-to converter (D/AC) as well as to collect data from the load cell and the displacement of the cylinders through an analog-to-digital converter (A/DC).

The sources for the interrupts come from 15 separate timers that can be separately programmed to trigger at different times during the cycle. The load and displacement are digitized 60 times per cycle; those data together with some other various signals combine to approximately trigger the A/DC 200 to 250 times during each cycle. After the data is digitized by the A/DC, it is stored in a buffer along with the gain in the A/DC, the cycle number, and the fraction of the cycle when it was acquired; eight bytes of information are used for one reading. When the 1 kB buffer its full, the computer switches to a second buffer and writes the information of the full buffer to a hard disk with a 10 MB capacity; at 200 to 250 readings per cycle the hard disk fills up in 5100 to 6400 cycles.

3.1.3 Video Signal and Data Storage

The signal from the CCD cameras are digitized by a frame-grabber inside the computer. The output from the CCD camera that tracks the front surface of the specimen to measure the crack length is acquired once per cycle. After the TV frame is digitized the program looks for a reference mark and the location of the tip. Once the reference mark and the crack tip are found the program proceeds to store their location as well as a portion of the frame where they were found. Because the program tracks the location of the reference mark and the crack tip in real-time it only needs to store a portion of the digitized frame; in this particular case a rectangular area 16 x 32 pixels that includes the reference mark and an area 32 x 48 pixels that includes the crack tip are stored. The storage requirements of the two rectangular areas amount to 2 kB/cycle, or 1/120 of the storage requirements for the whole frame.

The signal from the CCD camera that records the crack and craze opening displacements is digitized in response to variables that are set by three different timers. Once one of these timers generates an interrupt, the corresponding interrupt routine sets-up a flag to instruct the main program to acquire and store images from the opening displacements. One of the flags instructs the program to store a full frame of the opening displacements at the minimum and maximum load; the timer for this flag usually triggers every 250 cycles which represents a storage requirement of 1.92 kB/cycle. The second flag instructs the program to store a portion of the frame (64 x 128 pixels or 8 kB) once during the minimum load of the cycle. Usually the timer for this flag is set to trigger once every four cycles; in this case the storage amounts to 2 kB/cycle. The third flag is usually triggered once every 100 cycles and it instructs the program to acquire 11 frames during a cycle; a 64 x 128 pixel area is stored from each frame or the equivalent of 0.88 kB/cycle.

Thus, the storage requirements for the pictorial information from both cameras amounts to 6.8 kB/cycle. This information is stored on a log file in a (separate) hard disk with a capacity of 26 MB; for this particular case the hard disk would fill up in approximately 3800 cycles. This discussion illustrates the importance of performing calculations in real-time which reduce the amount of information that needs to be stored; in particular, if a full frame from each of the CCD cameras is stored once per cycle the hard disk would fill up in only 54 cycles.

3.2 Secondary Analysis

After the experiment is finished the log files are transferred to a separate computer for analysis. First, the information on the log files is separated into individual files. The cyclic information (load and displacements) is analyzed to determine the extrema in each cycle; for each file the minima, maxima, amplitude and the phase lag relative to the command signal are calculated.

The images surrounding the reference mark are analyzed by the computer to obtain sub-pixel resolution by the use of weighted averages. The images from the crack tip are visually inspected to improve the resolution in the position of the crack tip.[12] The stress intensity factor and its amplitude are calculated from the crack length and the load records. In addition, the compliance of the specimen is calculated from the load and displacement records; from the crack length, the compliance records and an elastic analysis[9] the value of an effective Young's modulus can be obtained. The term effective implies that the material does, indeed, exhibit sometime or rate dependence; The effective modulus thus corresponds to the particular cycle frequency in use.

---

[12]The results from the crack length record are presented in chapter 2.

4 Summary

A miniature loading device was built with a positional resolution of 1 μm. A single servovalve controls two cylinders to maintain the crack tip of a specimen at approximately the same location while it is being loaded. Two optical systems attach to the breadboard where the loading device is mounted and are used to record the crack length and the craze and crack opening displacements.

A computer is used to control the experiment as well as to make real-time measurements of the load, displacement and crack length in an automated fashion. For the typical cyclic data acquisition the computer is able to record data for about 5000 cycles. The computer integrates the control of the loading facility with the measurements of one-dimensional data as well as two-dimensional (visual) information thus creating a multi-media recording and control facility.

5 References

1. Elinck, J.P., Bauwens, J.C., and Homes, G., "Fatigue Crack Growth in Poly (Vinyl Chloride)," *International Journal of Fracture Mechanics*, Vol. 7, 277-287, 1971.
2. Döll, W. and Könczöl, L., "Micromechanics of Fracture under Static and Fatigue Loading: Optical Interferometry of Crack Tip Craze Zones," in *Advances in Polymer Science: Crazing in Polymers,* H.H. Kausch, Editor, Volume 91/92, pp. 137-214, Springer-Verlag, Berlin, 1990.
3. Hertzberg, R.W. and Manson, J.A., *Fatigue of Engineering Plastics,* 1st Edition, Academic Press, New York, 1980.
4. Liechti, K.M. and Knauss, W.G., "Crack Propagation at Material Interfaces: I. Experimental Technique to Determine Crack Profiles," *Experimental Mechanics*, Vol. 22, No. 7, 262-269, 1982.
5. Vendroux, G. and Knauss, W.G., "Interface Mechanics Using Scanning Tunneling Microscope," Report SM 92-35, California Institute of Technology, Pasadena, October, 1992.
6. DiStefano, J.J.I., Stubberud, A.R., and Williams, I.J., *Feedback and Control Systems,* Second Edition, Schaum's Outline of Theory and Problems of, McGraw-Hill, New York, 1990.
7. Thayer, W.J., "Tranfer Functions for Moog Servovalves," Technical Bulletin 103, Moog Inc. Controls Division, East Aurora, January, 1965.
8. Neal, T.P., "Performance Estimation for Electrohydraulic Control Systems," Technical Bulletin 126, Moog Inc. Controls Division, East Aurora, November, 1974.
9. Broek, D., *Elementary Engineering Fracture Mechanics,* 4th Edition, Kluwer Academic Publishers, Dordrecht, 1986.
10. Washabaugh, P.D., *An Experimental Investigation of Mode-I Crack Tip Deformation*, Doctoral Thesis, California Institute of Technology, Pasadena, 1990.

11. Tada, H., Paris, P.C., and Irwin, G.R., *The Stress Analysis of Cracks Handbook,* Del Research Corporation, Hellertown, 1973.

Appendix A: Specimen Geometry and Preparation

Two different types of PMMA were used in the testing. Most of the specimens were prepared from commercial-grade PMMA (Plexiglas G from the Rohm and Haas Company) while some were cast from medium molecular weight PMMA from the Aldrich Company. The typical weight-average molecular weight was 10^6.

For the medium molecular weight PMMA that was obtained from Aldrich in the form of pellets a plate was cast in a mold constructed by Dr. Peter Washabaugh [10]. The procedure to cast the sheet consists of heating the pellets (under vacuum) to 150 °C and pressurizing the mold to 1.4 MPa for about 30 hours (10^5 s) before slowly cooling after the pressure is removed. The cooling rate was prescribed to be 10^{-3} °C/s.

The geometry used for the experiments is the compact tension shown in figure A1. The formula for calculating the stress intensity factor was taken from Tada et al. [11]. The thickness of the specimens were about 2.85 mm (1/8" nominal) for the commercial PMMA and 3.1 mm for the PMMA from Aldrich.

After the specimens were cut, the top and bottom sides were polished to obtain a clear view through the specimen that allows the measurement of the craze and crack opening displacements. The lateral surface of the specimens were coated with a thin (15 nm) layer of Aluminum to provide a focusing plane for the crack length measurements. Finally, a razor blade, the thickness of which is the same as the width of the slit, is used to make a sharp notch in the middle of the specimen from where a fatigue crack is started; the crack in the specimens is allowed to propagate for about 2.3 mm to obtain a sharp crack and eliminate the effects of the razor blade.

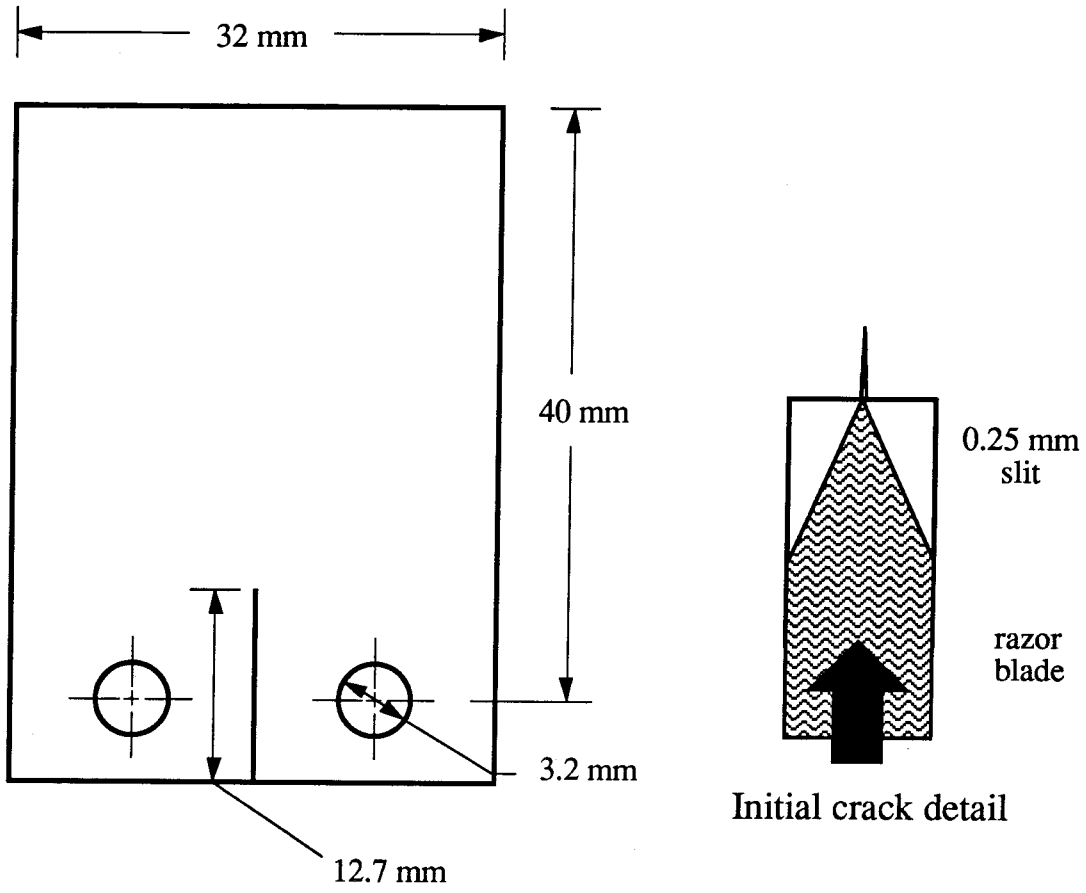

FIGURE A1 Compact tension geometry and initial crack detail.

Appendix B: Transfer Function of a Hydraulic Actuator

In this appendix we develop an expression for the transfer function of the hydraulic actuator shown in figure B1.

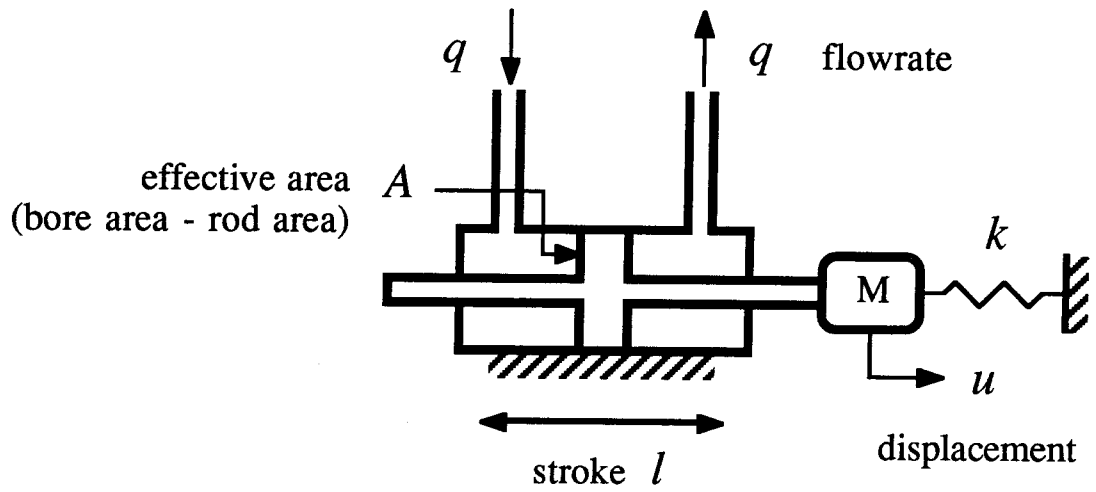

FIGURE B1 Hydraulic actuator.

The transfer function for the actuator can be derived in the following manner: Let the cylinder with effective area A and stroke l be in equilibrium at its center position and let the cylinder be connected to the servovalve through two tubes with volumes V_{T1} and V_{T2}. The change in volume due to a flow rate q and corresponding piston displacement u in each of the two chambers of the actuator is:

$$\Delta V_1 = Au - \int q\,dt \qquad \Delta V_1 = -Au + \int q\,dt. \tag{B.1}$$

The corresponding pressures for a fluid with a bulk modulus β are:

$$P_1 = P_1^0 - \beta\frac{Au - \int q\,dt}{Al/2 + V_{T1}} \qquad P_2 = P_2^0 - \beta\frac{-Au + \int q\,dt}{Al/2 + V_{T2}}. \tag{B.2}$$

The force F acting on the mass M is:

$$F = P_1A - P_2A - k(u^0 + u) = M\ddot{u}. \tag{B.3}$$

If $V_{T1}=V_{T2} \equiv V_T/2$ then equation B.3 becomes

$$\left[\left(P_1^0 - P_2^0\right)A - ku^0\right] - \left(4\beta\frac{A}{l}\frac{Al}{Al+V_T} + k\right)u + 4\beta\frac{A}{l}\frac{Al}{Al+V_T}\frac{1}{A}\int q\,dt = M\ddot{u}, \tag{B.4}$$

where the quantities with the superscript refer to the equilibrium state prior to q; thus, the quantity in the square brackets is zero.

Defining

$$\alpha \equiv \frac{Al}{Al+V_T} = \frac{\text{volume of cylinder}}{\text{total volume}} < 1 \tag{B.5}$$

$$k_F \equiv 4\beta\frac{A}{l}\alpha = \text{ stiffness of hydraulic actuator} \tag{B.6}$$

$$\omega_{LR}^2 \equiv \frac{k_F + k}{M} = \text{ load - resonance frequency} \tag{B.7}$$

and incorporating the effects of friction as modal damping, with a damping fraction ζ, equation B.4 becomes

$$\ddot{u} + 2\zeta\omega_{LR}\dot{u} + \omega_{LR}^2 u = \omega_{LR}^2\frac{k_F}{k_F+k}\frac{1}{A}\int q\,dt. \tag{B.8}$$

The corresponding transfer function $G_A(s)$ is

$$G_A(s) = \frac{\omega_{LR}^2}{s^2 + 2\zeta\omega_{LR}s + \omega_{LR}^2}\frac{k_F}{k_F+k}\frac{1}{As}. \tag{B.9}$$

Equation B.9 is the desired expression and consists of two parts: The first part is the dynamic effect of the load-actuator interaction which is modeled by a second-degree oscillator with a d.c. gain (gain as $s \rightarrow 0$) of $k_F/(k_F+k)$ and a natural frequency ω_{LR}. The second part is the consequence of the integrating action of the actuator and has a coefficient which is the inverse of the actuator's effective area A.

Appendix C: Schematic of the Electronic Circuits

This appendix includes the schematic diagrams of the circuits that control the loading device as well as the circuits that condition the output of the transducers so that they can be digitized by the computer.

All of the unmarked operational amplifiers are of the OP7 type. The power supplies for all the circuits are ± 15 V as it is also the additional power supply of the servovalve current driver.

Figures C1 and C2 are the signal conditioners for the LVDTs and load cell respectively. Figure C3 shows the circuit that produces the combined feedback. Figure C4 is the servoamplifier that closes the feedback loop while figure C5 details the limit detection circuit that provides an automatic shut-off of the servoamplifier when any of three signals exceeds its preset limits. Finally, figure C6 show the circuit that drives the servovalve.

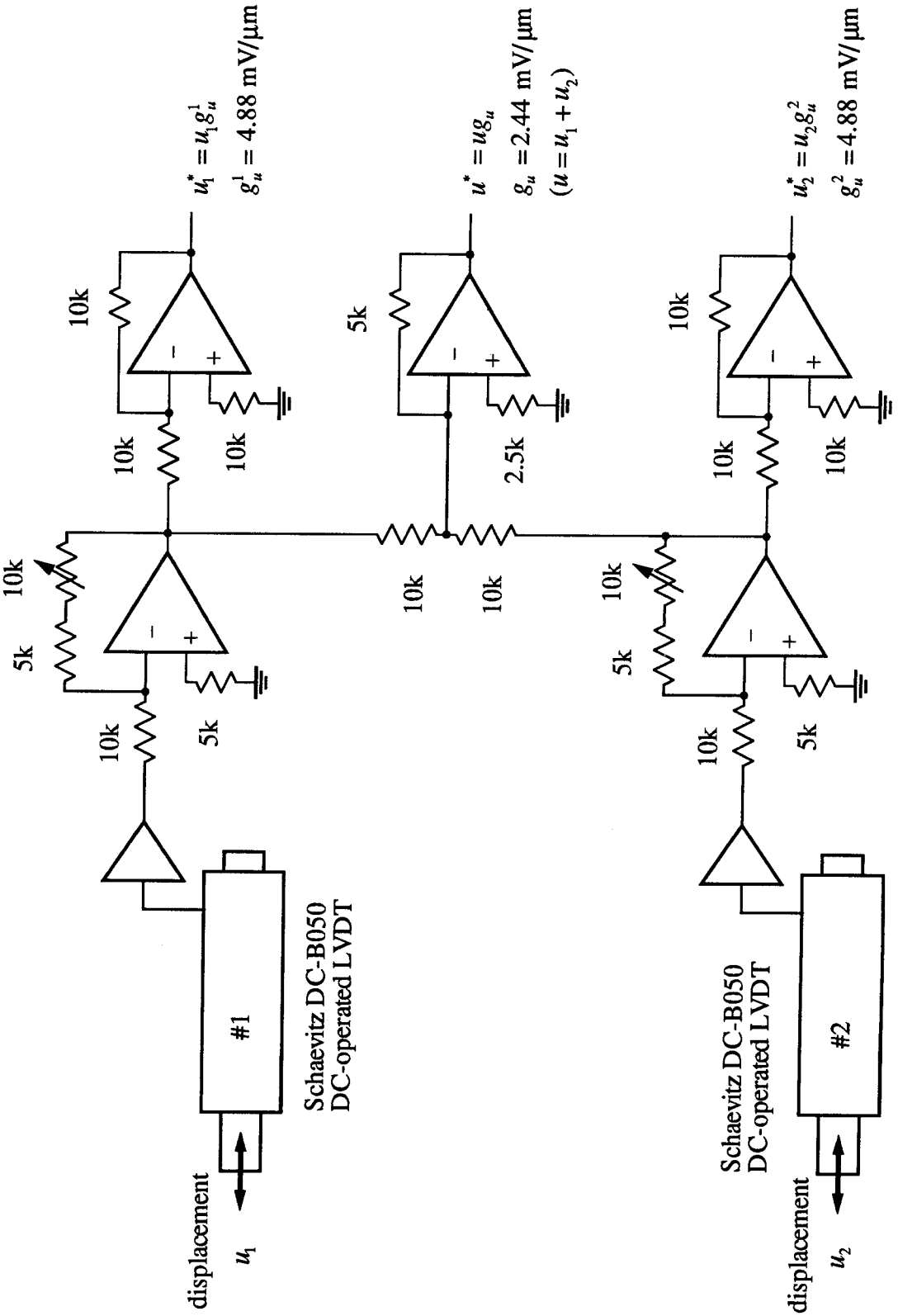

FIGURE C1 LVDT signal conditioner.

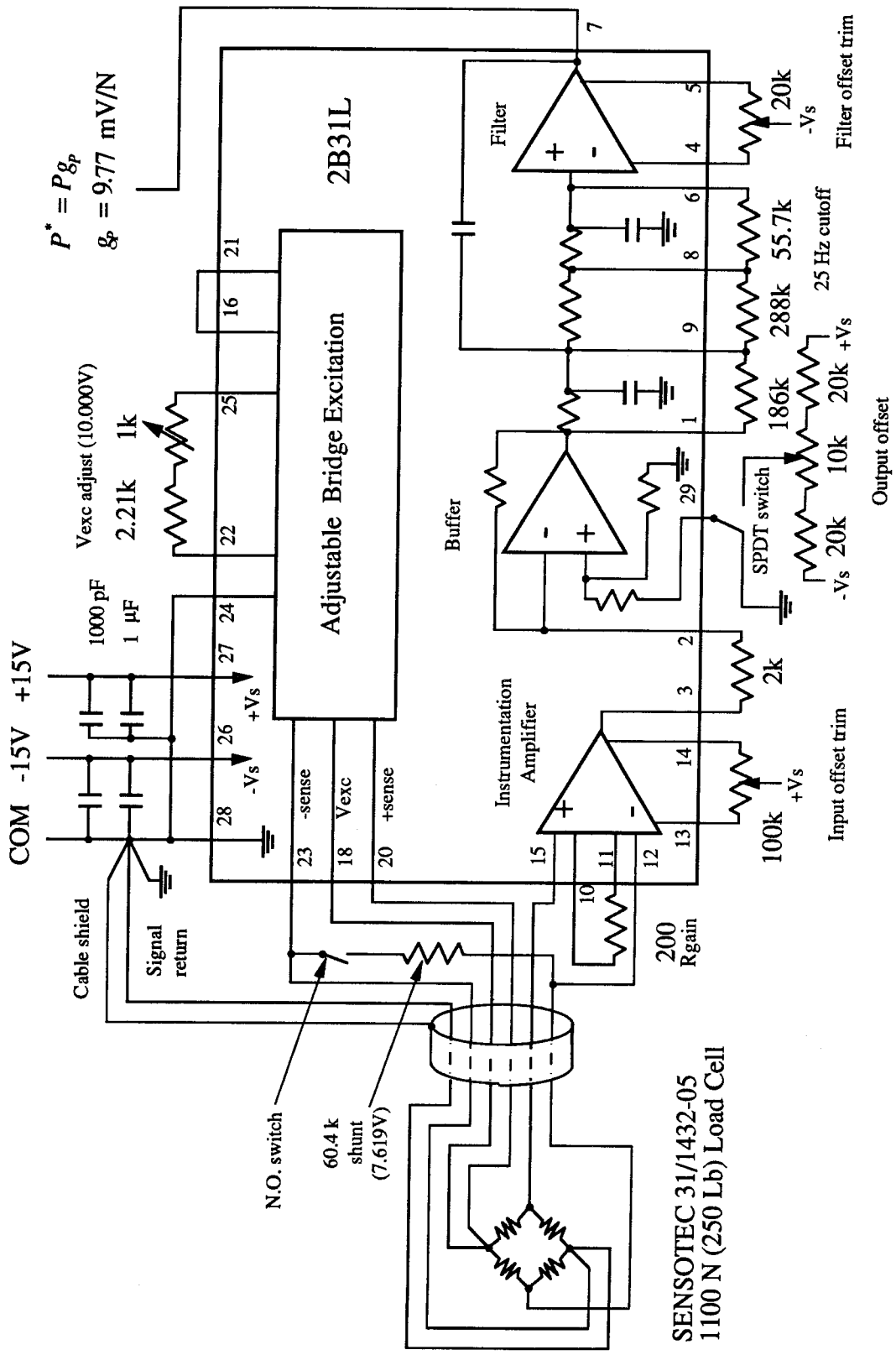

FIGURE C2 Load cell signal conditioner.

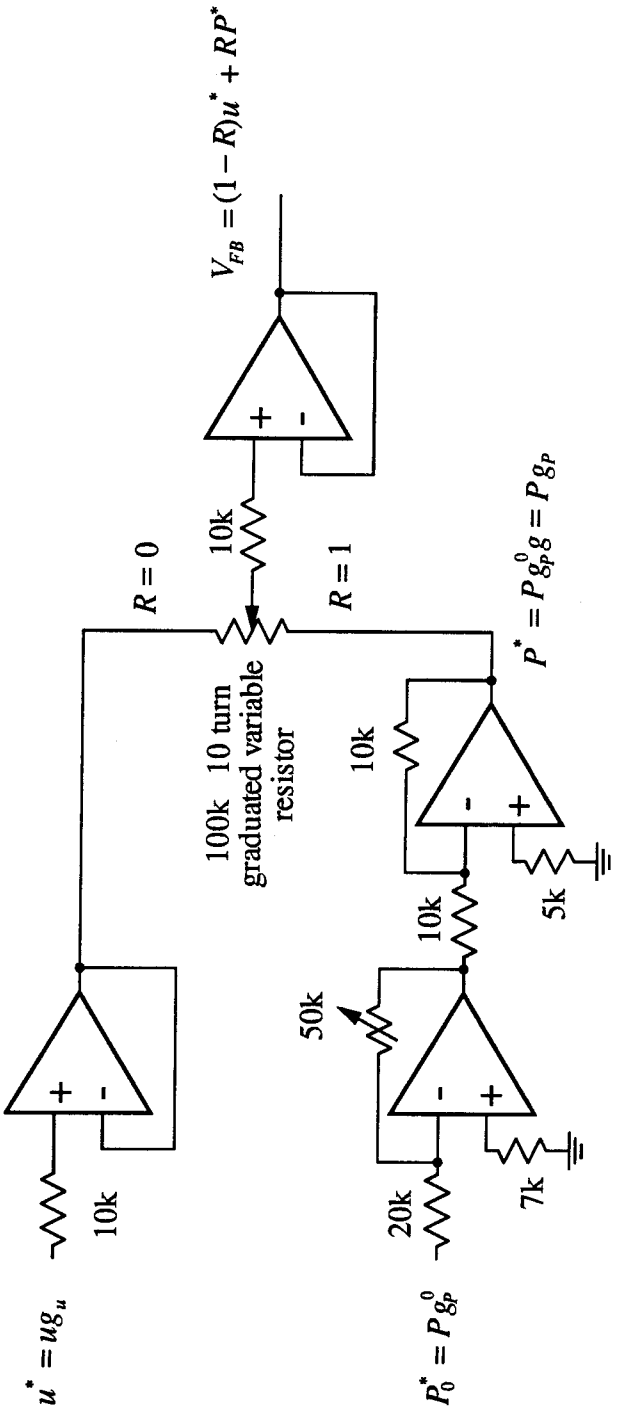

FIGURE C3 Combined feedback schematic.

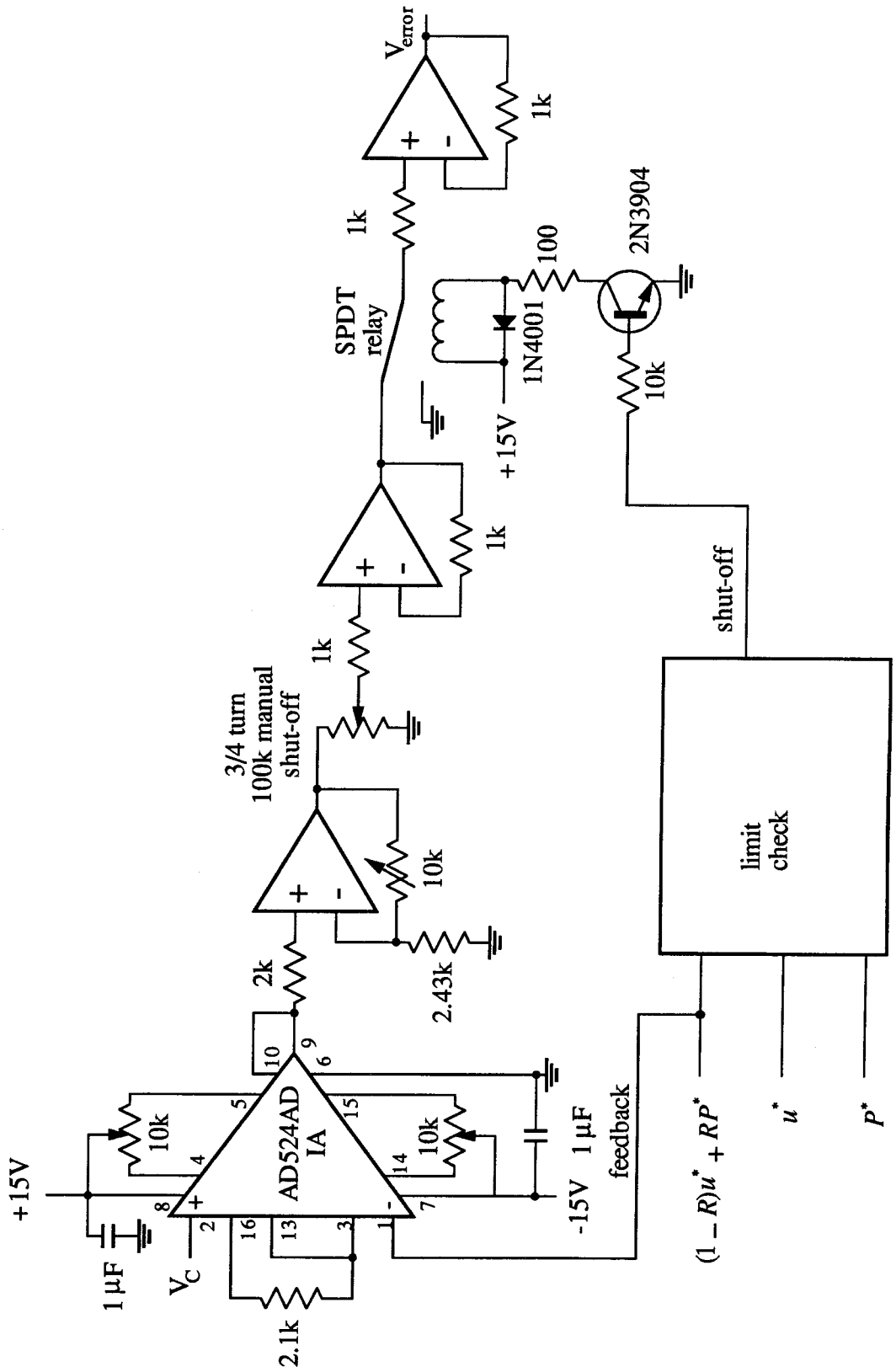

FIGURE C4 Servoamplifier.

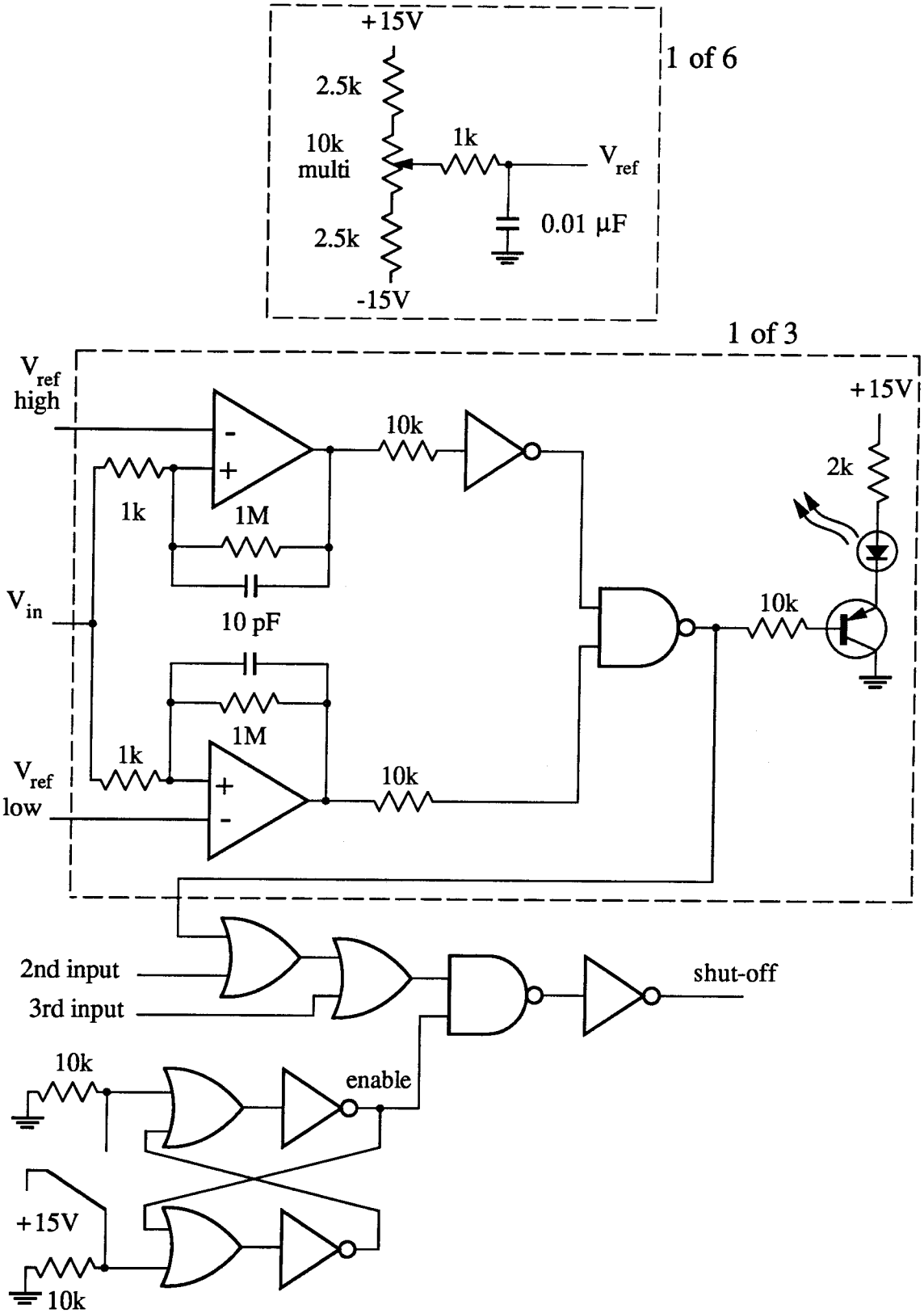

FIGURE C5 Limit detection.

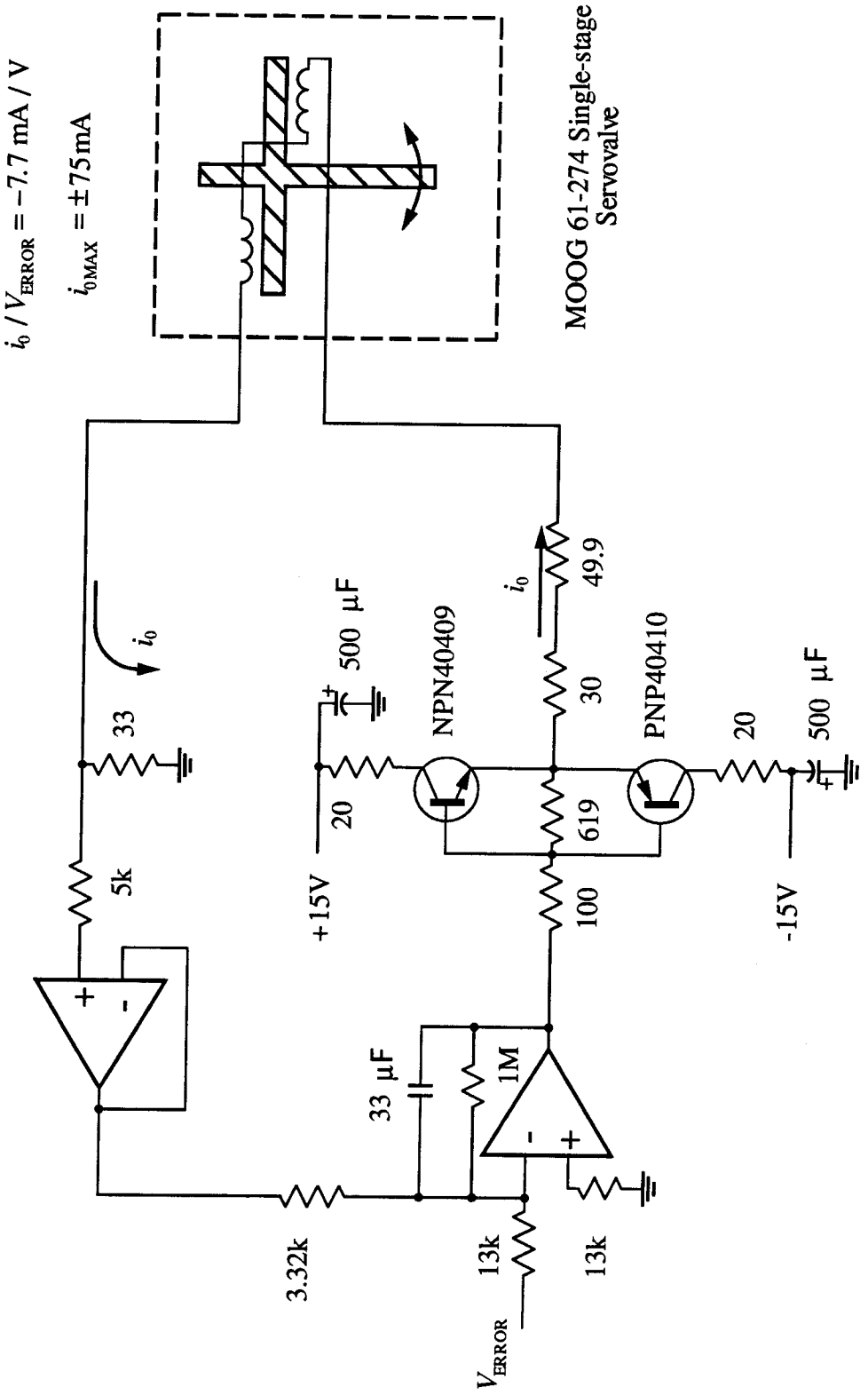

FIGURE C6 Servovalve current driver.

II. HIGH RESOLUTION CRACK LENGTH MEASUREMENTS THROUGH COMPUTER VISION

Abstract

This chapter summarizes discussions on the method of determining the advance of crack tip through combined microscope and computer-analyzed observation. In particular, the experimental set up and software development is described by which these measurements are achieved. It is shown that automated crack tip location is possible with a precision of one to two microns, which is amply sufficient for present purposes to make definitive statements about the smoothness or discontinuity of crack propagation.

1. Introduction

Failure of thermoplastics materials at the tip of propagating cracks involves the development of a craze ahead of the crack tip [1]. Usually, this zone is referred to in standard fracture mechanics parlance as the process zone. In this zone the material has reached a stress level which allows the molecular chains to become oriented into fibrils parallel to the (crack opening) tension stress. Because the craze formation and propagation involves a transition from the bulk polymer state into fracture it plays a key role in determining the fracture process. While the next chapter is devoted to the behavior and damage that occurs in the craze this chapter focuses on the length scale aspects of the craze.

The size of the craze zone is determined by two different processes: the first one involves the fibrillation conversion at the tip of the craze where bulk material is transformed into craze material. The second process is the failure of the fibrils at the base or trailing end of the craze as the crack propagates into the craze. Both of these processes not only determine the length of the craze but in addition determine the mode of propagation. Specifically, if both processes propagate in phase and at the same rate the propagation is the same on a cycle per cycle basis; this type of propagation mode is known as continuous[1] and constitutes a self-similar translation of the crack and craze tip with each cycle. In other words, it occurs without change in the length of the craze.

A second mode of crack and craze propagation occurs when both processes occur out of phase with respect to each other. In the extreme case the crack remains stationary for a number of cycles while fibrillation enlarges the craze; at a particular cycle the crack breaks through the craze or through a part of it. This mode is called discontinuous or

[1]In his second review article [2] Döll argues that all crack/craze propagation is discontinouos in nature since it only occurs during part of the loading cycle. Thus, he denotes the continuous mode of propagation normal (fatigue) crack growth (NCG) and the discontinouos mode as retarded crack growth (RCG).

retarded since the crack remains stationary for some number of cycles before it propagates during a single cycle; in this event the average crack growth is the jump distance divided by the number of cycles required to bring the crack to the propagation stage. Implicit in the notion of discontinuous crack propagation is the idea that the length scales involved are equal to or smaller than the length of the craze. The discontinuous or retarded mode of crack growth under fatigue loading was first observed by Elinck et al. [3], who measured the crack length as a function of time in PVC and by taking the frequency into account determined that the markings on the fracture surface corresponded to crack growth at approximately every 370 cycles.

These considerations prompted in part the question of how a crack/craze configuration propagates under various loading conditions. A further motivation in this quest was the observation that under truly dynamic crack propagation conditions (crack speeds on the order of hundreds of meters per second) the fracture surfaces in PMMA exhibited a periodic structure, which could be correlated with timewise periodically emitted surface waves [4]. However, it was particularly surprising that this spatial periodicity correlated well with periodicity observed under cyclic loading [5] even though the time scales in these phenomena are widely different.

In most studies of the propagation of a fatigue crack its growth is monitored by following the position of the crack tip on one of the test specimen surfaces. One important question that arises in such circumstances is whether the crack advance is non steady because of the fracture process near the specimen surface, and whether the crack advance on average through the thickness is more uniform. For example, it could be quite possible that the crack leads on one side of the specimen for some time, while it leads on the other side at a later time, thus giving the appearance of unsteady crack growth while still maintaining a steady growth averaged through the thickness.

We set out to investigate in detail the history of crack tip motion in PMMA. Specifically, the objective is to observe in real-time[2] the crack growth on a cycle per cycle basis. As was discussed in Chapter I, a miniature hydraulic loading device was constructed for this purpose; in this Chapter are discussed the high precision measurements made on the surface of PMMA compact tension specimens through an optical system. The experimental set-up, including the optical arrangement, illumination and data collection, is discussed in the next section. The procedure used in detecting the nonsteady crack growth is described in section three. Section four discusses the surface morphology resulting from two different types of loading conditions and the chapter ends with some conclusions in section five.

[2]In this context real-time refers to the time while the experiment is running.

2. Experimental Set-up

In order to achieve sufficiently high resolution for tracing differences in steady as opposed to discontinuous crack growth it is necessary to devise means by which crack tip location can be identified on a cycle per cycle basis. Certainly, the spatial resolution required for this objective must be measured in units substantially smaller than the length of the craze. Thus (optical) microscope methods are indicated. At the same time the large number of data points that are likely to be required for this purpose raise the need for (semi)automatic means of monitoring the crack tip position. The following description delineates these accomplishments.

2.1 Optical Arrangement

The optical system for tracking the crack length consists of a CCD camera, a mirror and a microscope objective lens. The optical system is mounted on a traversing mechanism attached to the breadboard of the loading device. A schematic and a photograph of the optical system are shown in figure 1. The traversing mechanism is used to focus the optical system as well as to maintain the crack tip within the field-of-view of the camera. By trade-off between resolution and the size of the field-of-view one obtains high resolution through reduction of the field-of-view. In this case one achieves a pixel dimension of about 2 μm by virtue of a microscope objective with a magnification of 5X together with a "1/2-inch" CCD sensor. The resulting field-of-view is approximately 1.3 mm by 1 mm.

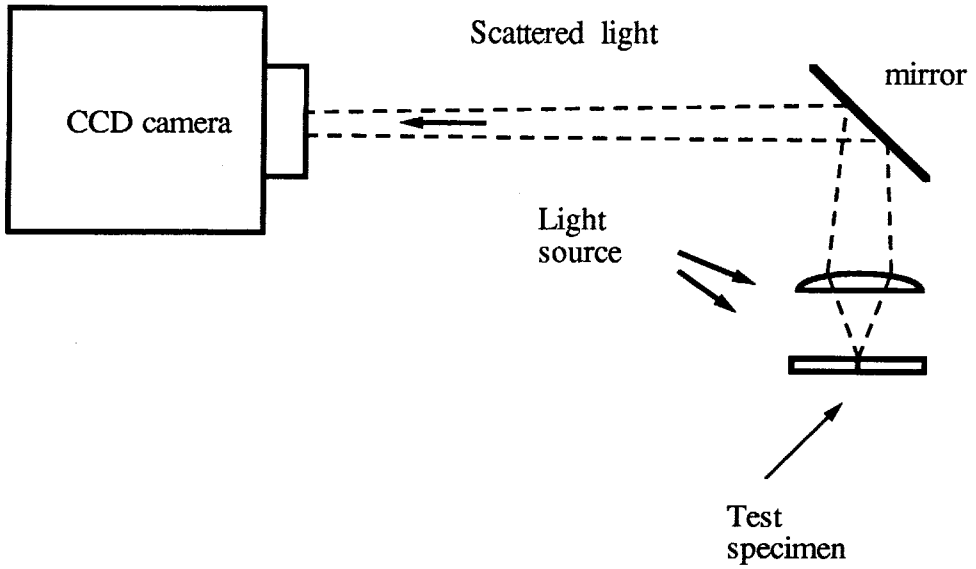

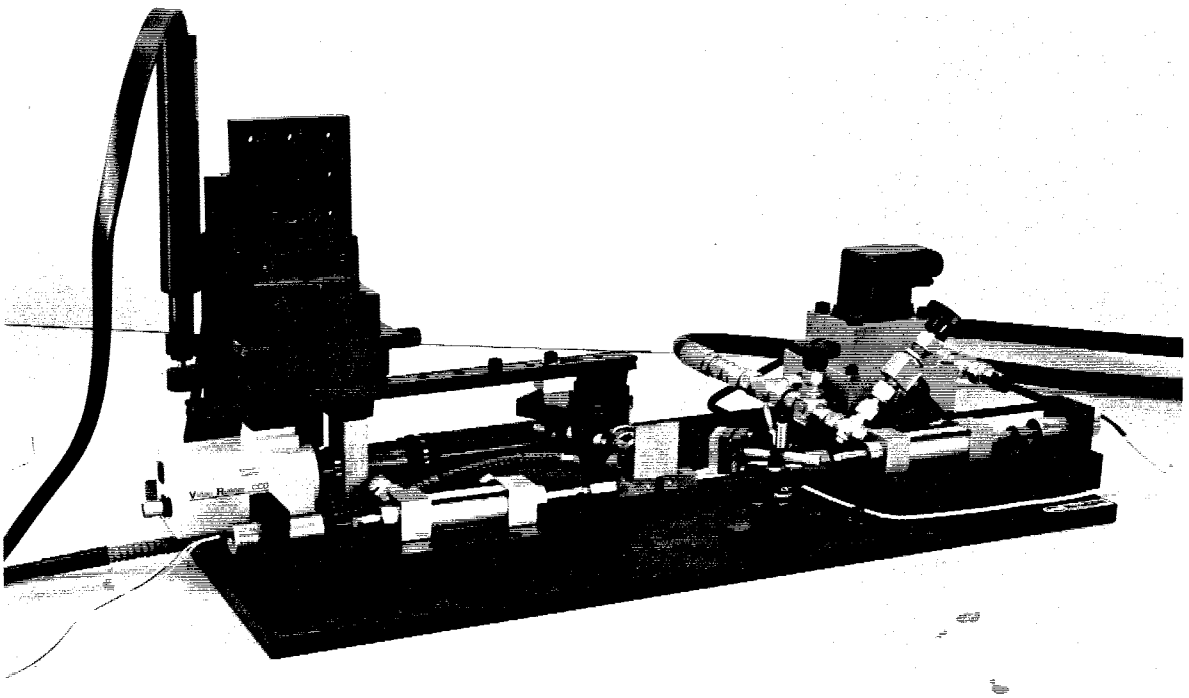

FIGURE 1 Schematic and photograph of the optical arrangement to record the crack length on the surface of the specimen.

2.2 Illumination

A fiber optic light guide provides white light illumination in a dark-field configuration. A beam of light strikes the surface of the specimen at an angle of approximately 45 degrees with respect to the surface normal; the projection of the beam onto the surface is perpendicular to the direction of crack propagation. As it is typical of dark-field illumination systems the image of the surface appears dark except at locations offering an abrupt change in the orientation of the surface, such as scratches or dimples, where light is scattered into the optical system. The schematic for the dark-field illumination is shown in figure 2. Also shown in the figure are the surface plots from two pixel arrays: one was produced by a small round-shaped dimple and the second by the crack.[3] The use of these arrays to obtain a high resolution measurement of the crack length is delineated next.

2.3 Data Acquisition and Analysis

As mentioned earlier a small field-of-view is required to achieve the high resolution crack length measurements desired for precise crack tip location evaluations. To obtain a high resolution measurement the position of the crack tip relative to a reference mark (within the field-of-view) is tracked in each cycle as the experiment progresses. Two types of measurements are made: the first, delineated in subsection 2.3.1, is made in real-time while the experiment is in progress and its purpose is to reduce the amount of storage;[4] the second is made after the experiment is finished and its purpose is to improve the resolutions in the crack length record and is described in subsection 2.3.2.

---

[3]Only the area surrounding the crack tip is shown.

[4]Prior to the development of the combined feedback technique the real-time crack length record was also used to control the stress intensity factor.

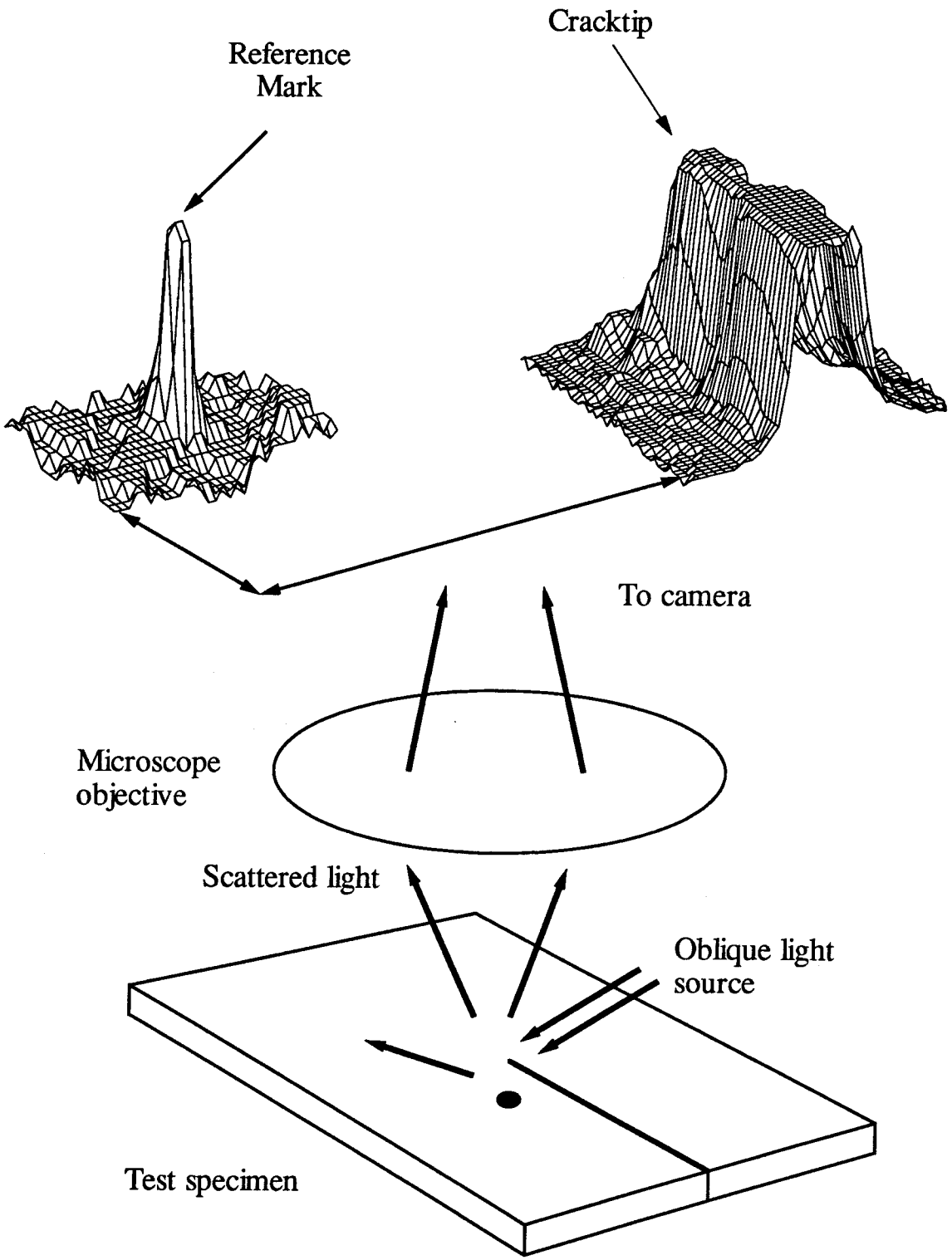

FIGURE 2 Schematic of dark-field illumination.

2.3.1 Real-time Measurement

Once during every loading cycle, at the maximum load during the cycle, the computer acquires a TV video frame and digitizes it into a 512 x 480 pixel array. The dimensions of each pixel are 1.94 μm x 1.59 μm where the smaller dimension corresponds to the direction of crack propagation. The computer obtains the crack length by tracking the location of two rectangles: a 16 x 32 pixel array centered around a reference mark and a 32 x 48 pixel array surrounding the crack tip.

The search for the reference mark is as follows: From the previous location of the reference mark, the computer searches in the surrounding area for the new location of the reference mark.[5] This is accomplished on a line-by-line basis as the computer looks for pixels with intensities above a given threshold as defined prior to starting the experiment. Due to the high contrast between the background and the reference mark, it is very simple to define a threshold so that the computer can quickly identify the location of the reference mark.

Once the new location of the reference mark is obtained a new search is started a few pixels behind the last known position of the crack tip and in the direction of crack propagation. The computer searches for pixels with intensities above the threshold and the scan where the search ends is logged as the new crack length. The computer then stores the rectangular areas surrounding the reference mark and the crack tip as well as the relative distance between the rectangles. The storage requirements are 2 kB/cycle or 1/120 of the 512 x 480 array. Thus, the calculations performed in real-time serve to obtain a crack length record as well as to reduce the amount of storage necessary to later reconstruct the crack length record.

---

[5]Due to small vibrations the relative position of the reference mark within the TV frame changes from cycle to cycle.

2.3.2 Secondary Analysis

The analysis performed after the experiment finishes improves on the previous computer record to produce a better resolution (of about 2 μm) in the crack length record for two reasons: The analysis of the reference mark is improved through a more detailed analysis involving the weighted average of all the pixels surrounding the reference mark; this analysis pinpoints the centroid of the reference mark to a higher resolution.

Second, a visual inspection of the rectangle surrounding the crack tip allows a higher (dynamic) threshold to be used in determining the crack tip position. Although there exists high contrast between the crack and its background, the threshold for the crack tip has to be kept low so that the computer (without the help from the operator) does not "loose" the crack tip during the experiment. This reduction in the threshold causes the program to introduce noise in the crack length record as it (incorrectly) responds to pixels in the background with a high intensity as belonging to the crack. This type of noise is eliminated as the rectangular pixel array is visually inspected by the operator.

3. Crack Growth Analysis

This section discusses crack length records obtained during fatigue experiments. The far field stress intensity factor was adjusted so that the average crack growth rates were on the order of 1 μm/cycle. It is in this regime where the crack tends to start propagating with decelerating and accelerating periods (discontinuous crack growth).

We first demonstrate the results from an experiment for which the crack length record is differentiated directly to determine the growth rate and then discuss a procedure that illustrates better the nonsteady crack propagation behavior in PMMA.

Figure 3 shows a full field digitized TV frame of the lateral surface for which the crack length was measured[6] at a test frequency of 0.5 Hz. Also shown in the figure are the rectangles surrounding the crack tip (32 x 48 pixels) and the reference mark (16 x 32 pixels). The data recorded in this particular record started when the crack length was 11150 μm and finished when the crack length reached 11750 μm (600 μm growth). The rate of crack growth was obtained by differentiating the crack length record and then plotting it against the crack length. The stress intensity factor was calculated from the load and crack length records; it is also plotted in figure 3. When the experiment started the crack grew with an average speed of 1 μm/cycle; as the crack length reached 1275 μm the loading was increased and the crack began to propagate with an average speed of 2 μm/cycle As the crack length reached 11500 μm the loading was reduced again and the average growth rate dropped to 0.5 μm/cycle.

---

[6]As it was discussed in section 2.2 the sytem uses dark-field illumination which renders the background dark. However, for display purposes the pictures has been digitally enhanced by the process of thresholding [6] where every pixel with an intensity below 105 had its intensity changed to 255 which prints as white.

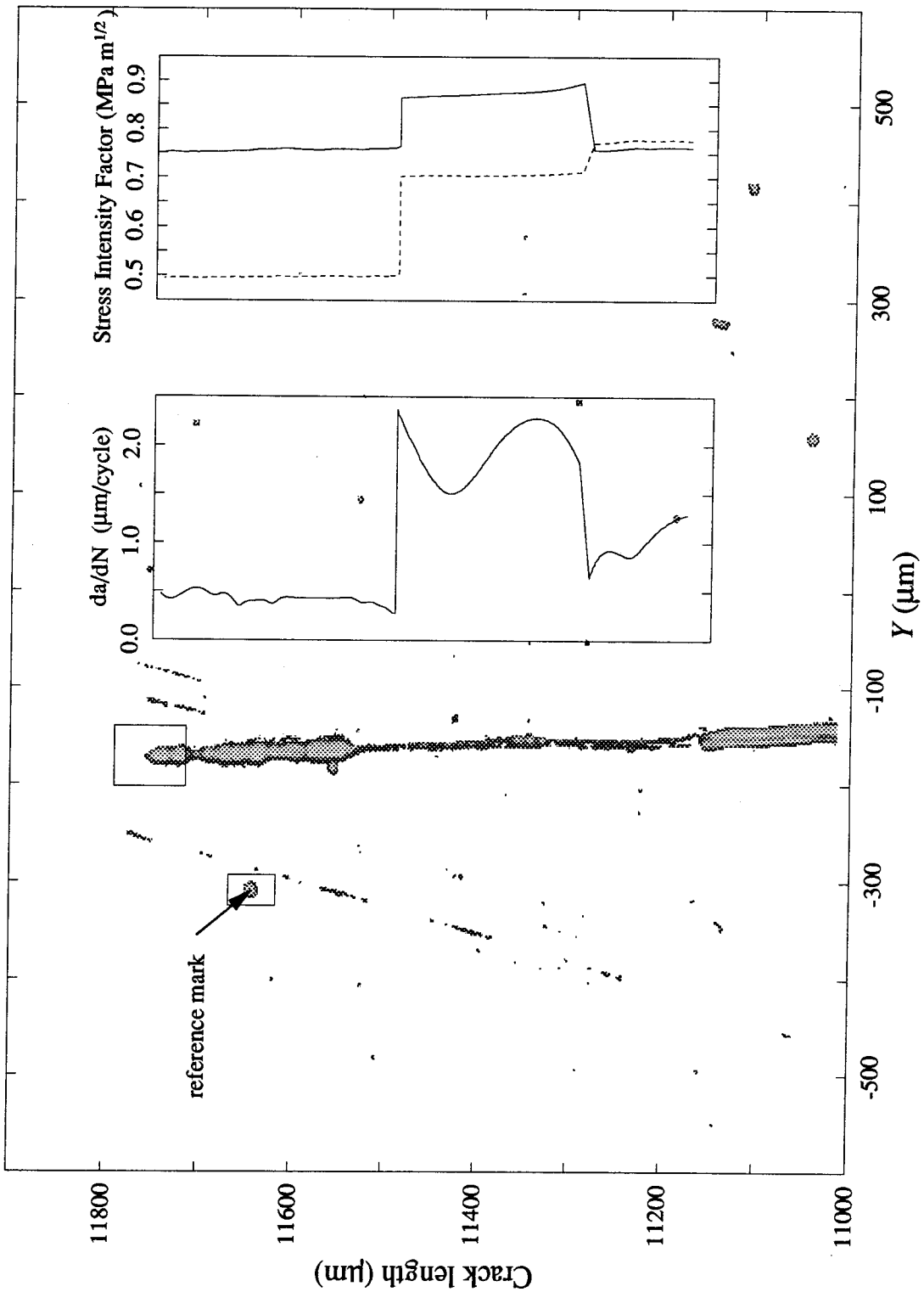

Figure 3 Digitized TV frame of the crack tip region.

Three comments are in order: First, one notes in figure 3 that a dark band accompanying the crack varies in correlation with the stress intensity factor or the crack speed. As the crack propagates at a slower rate this "crack band width" increases. The reason for this band is the optical effect of surface reflection of light as modified by the passing of the high stress/strain crack tip region: From the discussion about the dark-field illumination it is clear that the width is related to the permanent deformation which produces changes in the surface slope which allows the scattering of more light into the lens. Thus, this correlation suggests a damage model that is time-or rate-dependent so that a more slowly propagating crack generates more deformation or damage which then occurs over a wider area or is more severe. Second, the crack has not propagated in a straight line but deviated by 100 μm when its length was 11000 μm. The angle of deviation is approximately 2.5°[7]. However, the angle is small enough and this situation did not occur often enough that it presented a systematic problem in the analysis process. Third, differentiating the crack length enhances the inherent noise present in the data and it becomes necessary to "smooth" the noise before presenting the results. For this purpose a running polynomial[8] was used to filter the data. The filter (computer algorithm designed for this purpose) was applied several times until it was decided that the data contained very little noise and what was left over constitutes a real signal.[9] This procedure presents a problem in that a subjective judgment is needed to decide between signal content and noise. By way of explanation, it is clear that the oscillations in the growth rate between 11300 μm and 11500 μm are indeed the result of material behavior, but it is difficult to attach much meaning to the (small) oscillations in the growth rate after 11600 μm.

---

[7]The crack was started from a symmetric slit with an initial crack length of 8700 μm.

[8]A low-order polynomial such as a parabola is least-square-fitted to an odd number of points; the calculated ordenate for the center point replaces the original one; the fit is then performed on the next data point. If the filtering program takes care of the end points in such a way that the new data set has the same number of points then the program can run *ad-infinitum* and each new data set is smoother than the previous one.

[9]In the sense that it contains information.

Because of the uncertainty in distinguishing among signal and noise and the subjective judgment required in filtering the data, it was decided to search for a different way of analyzing the data so as to distinguish more readily between signal and noise. That analysis is described in the remainder of this section.

3.1 Crack Length Deviation

Instead of fitting a low-order polynomial to a small portion of the crack length record for differentiation purposes it is more useful to fit a low-order polynomial to the whole record[10] and subtract this curve-fitted data from the original record. Figure 4a shows the original data record as well as the fitted function. The fitted function is then used to determine its "deviation" from the real data ; a plot of this deviation against crack length as it is shown in figure 4b.

This procedure offers several advantages: First, the choice of the fitting function can be justified since the loading is prescribed and knowledge is available about the relation between loading and growth rate. Specifically, if the loading is such that the stress intensity factor remains constant[11] one expects the growth rate to be also constant so that fitting a first-or second-order polynomial could be justified on physical grounds. Second, separating the deviation from the average growth rate provides a better way of identifying nonsteady growth. Third, up to this point no subjective decision is needed which could obscure the boundary between signal and noise.

---

[10]In records where the loading is changed during the experiment the record is subdivided into portions and each portion is treated as a separate experiment.

[11]An appendix to this thesis describes a procedure in which a combination of load and displacement produce extremely small variations in the stress intensity factor for a compact tension geometry.

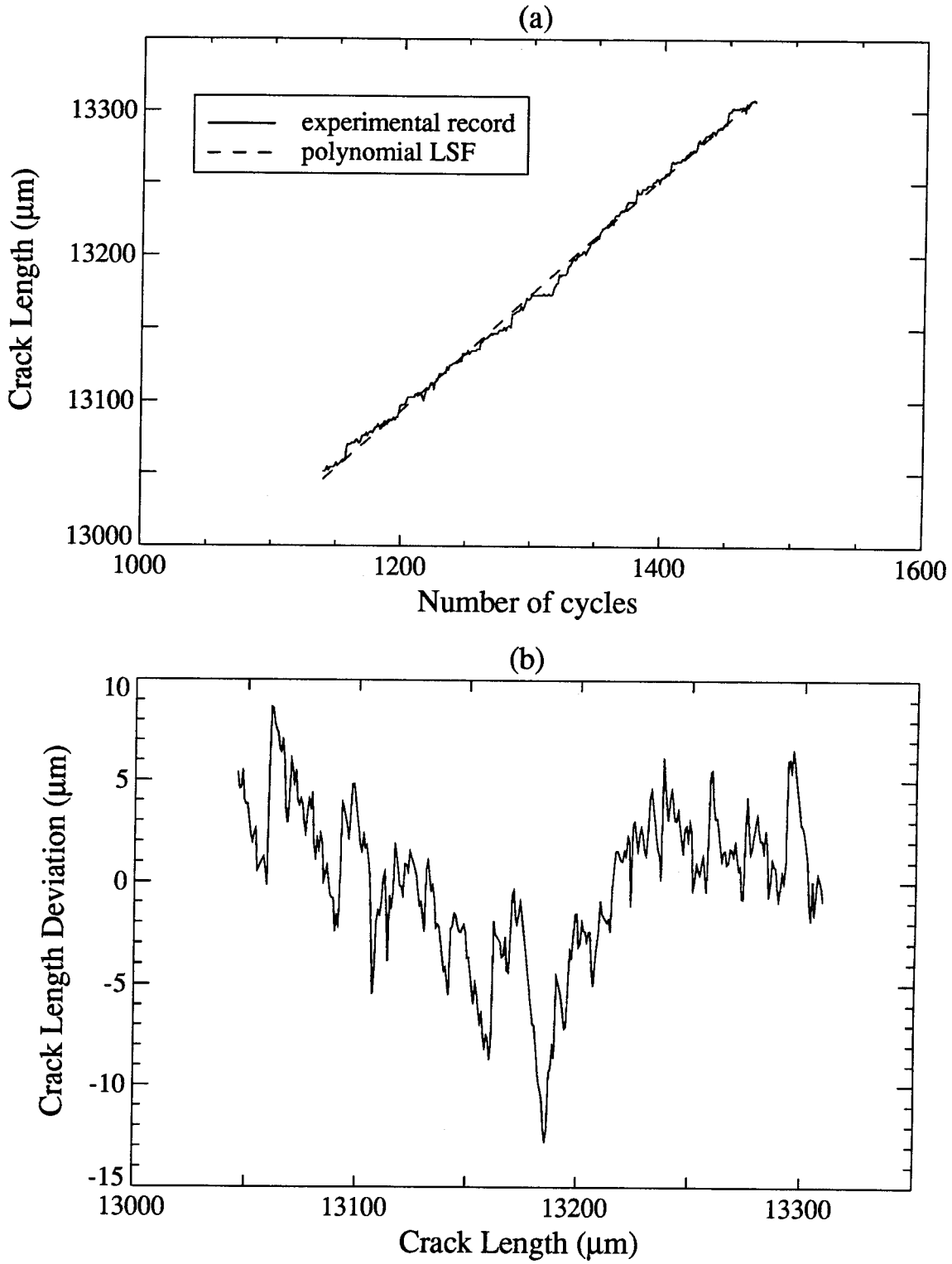

FIGURE 4 Crack length (a) and (b) crack length deviation records.

In interpreting the crack length deviation record we distinguish among two types of noise and one signal: Small "wiggles," the size of which are about 1-2 μm, clearly represent noise in digitizing the video signal (each pixel is 1.6 μm in size); the frequency of this occurrence is very high. There is also present a very low frequency noise introduced by the choice of the fitting function: The deviation is mostly positive in the beginning, mostly negative in the middle and becomes positive at the end. This very low frequency noise can even be identified from the crack length record. If we had chosen a parabola instead of a straight line this type of noise would have been reduced. In this case the choice was made to fit a straight line for two reasons: First, it illustrates clearly the presence of this type of noise and second, unless the relation between loading and growth rate is perfectly known, there will always be some uncertainty in the choice of function which will then introduce this type of noise.

The signals present in the record are the variations, in crack tip position relative to the average location which represent decelerating and accelerating stages. In the example shown these have amplitudes of about 5 to 10 μm. In a later example, it will be shown how they correlate with the markings present in the fracture surface. While it is easy to identify the amplitude of these variations from the record itself, the determination of their period is performed with the aid of Fourier analysis.

3.2 Fourier Analysis

If one takes the Fourier Transform [7] of the crack length deviation record (c.f. figure 4b) the frequency content of the record can be investigated. Let us plot the magnitude of the Fourier transform against the inverse of frequency, rather than against the frequency itself as is usually done. Such a plot is shown in figure 5. Figure 5a shows the results of the Fourier transform of the crack length deviation record of figure 4b. The abscissa in this case is the period in microns since the abscissa of figure 4b was the crack

length (measured in microns). The plot of figure 5b shows the result of the transform with the input data as the deviation plotted against the number of cycles. Thus, in this case the period corresponds to the number of cycles.

The peaks in the middle of the plot represent the desired information. However, due to the low frequency noise introduced by the choice of the fitting function, the information is mixed with the harmonics of low frequency noise. While it may seem that one has traded the problem of the smoothing for this type of problem, it is possible to discern between the harmonics of the low frequency noise and the periods of the variations caused by the nonsteady crack propagation. At the end of the next section, after a discussion of the features in the fracture surface, an example is shown in which, after identification of the harmonics of the low frequency noise, the periods associated with the nonsteady growth are correlated with the small scale features in the fracture surface.

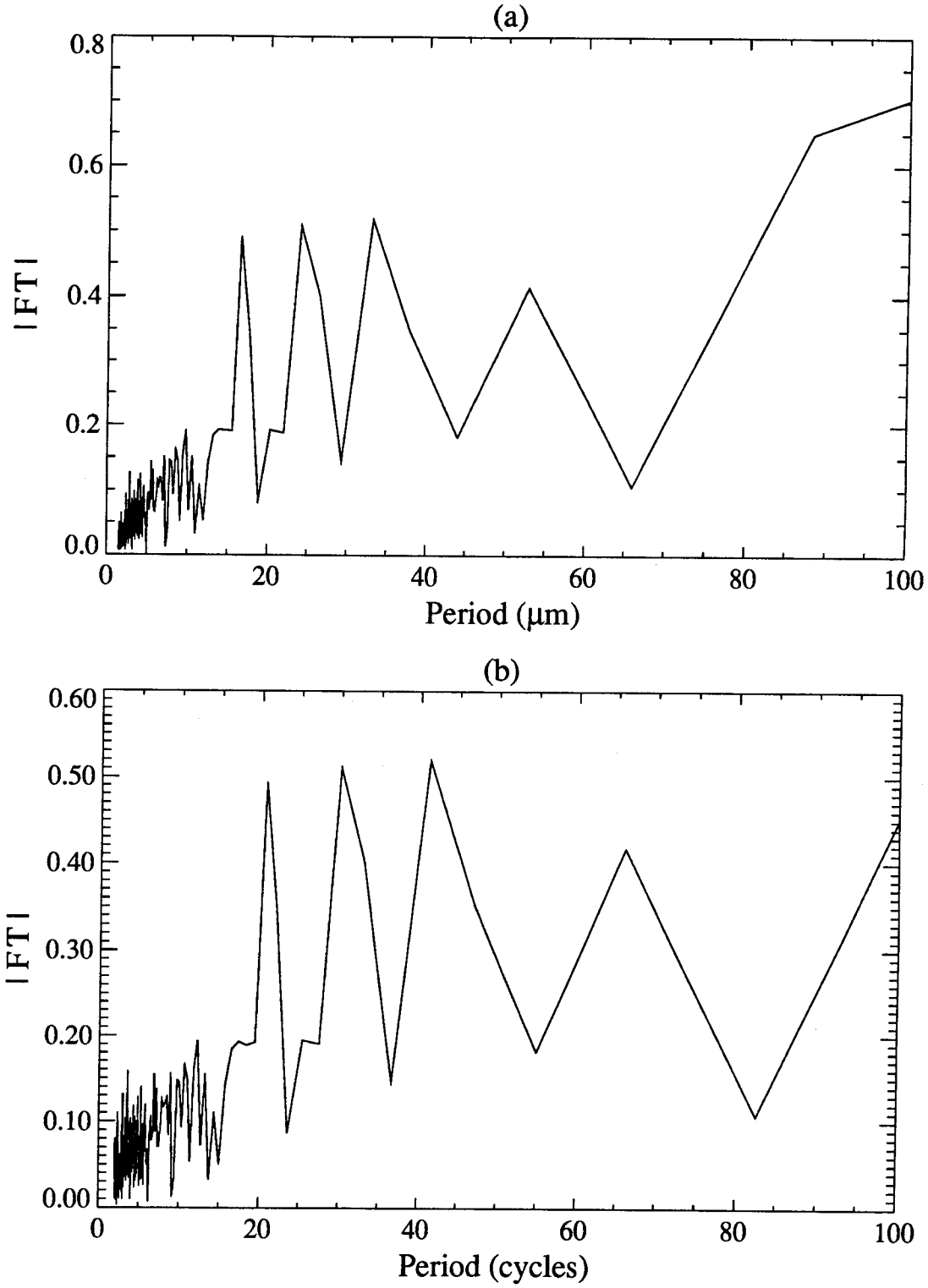

FIGURE 5 Magnitude of the Fourier transform of the crack length deviation record. Crack length record was a function of the crack length (a) and a function of the number of cycles (b).

4. Fracture Surface Morphology

This section discusses the results from two different experiments. In the first experiment the stress intensity factor is varied between different tests and it is chosen large enough so that multiple crazes form in front of the crack with the crack jumping between the different crazes as it propagates [8]. The second experiment is conducted under a constant stress intensity factor and the test frequency is varied producing different stress intensity factor rates.

4.1 Variable Stress Intensity Factor Experiment

The fracture surface morphology (obtained from optical microscopy) of the experiment is shown in figures 6 and 7. Plotted along with the morphology and properly scaled is the crack length deviation record.[12] Thus, the scale denoted by X (in microns) serves for both the deviation record and the photographs. The crack length was measured on the edge next to the deviation. The large and rough features in the fracture surface have dimensions along the direction of propagation (increase in X) that are comparable with the periods of the deviation. As the crack front moves through the specimen the crack is propagating in different planes.

Figure 7 shows the end of the first experiment as the crack length reached 14200 μm. The thin band across the surface represents the crack front and a line through the middle of the craze where the crack breaks through as it propagates in a nonsteady fashion. The width of the band is about 20 to 30 μm; from this information and from the stress intensity factor the craze length is estimated to be 35 to 45 μm.

[12]The high frequency noise in the deviation record has been filtered out for display purposes.

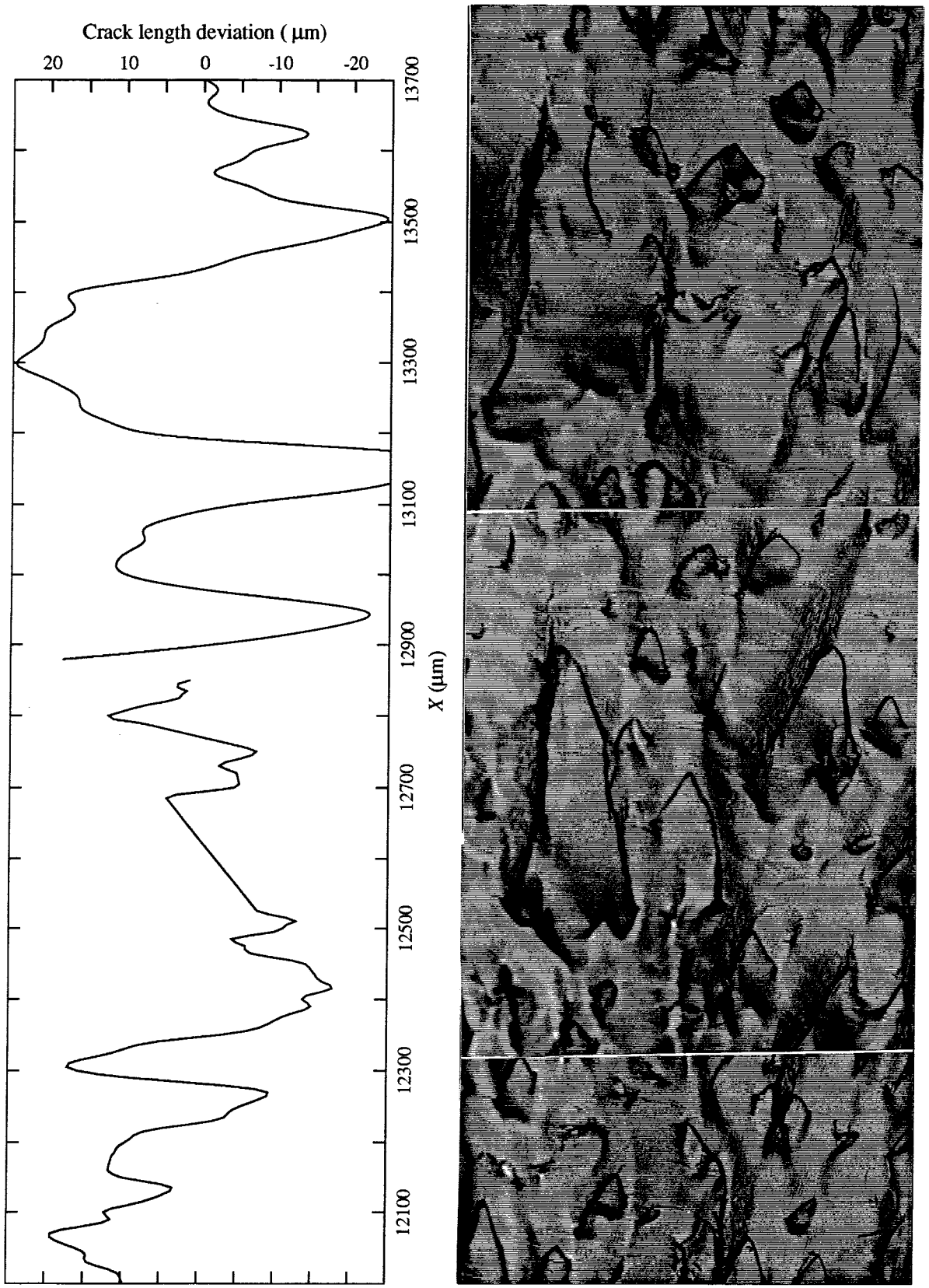

FIGURE 6 Crack length deviation and fracture surface morphology at high stress intensity factors (0.8-1.0 Mpa $m^{1/2}$).

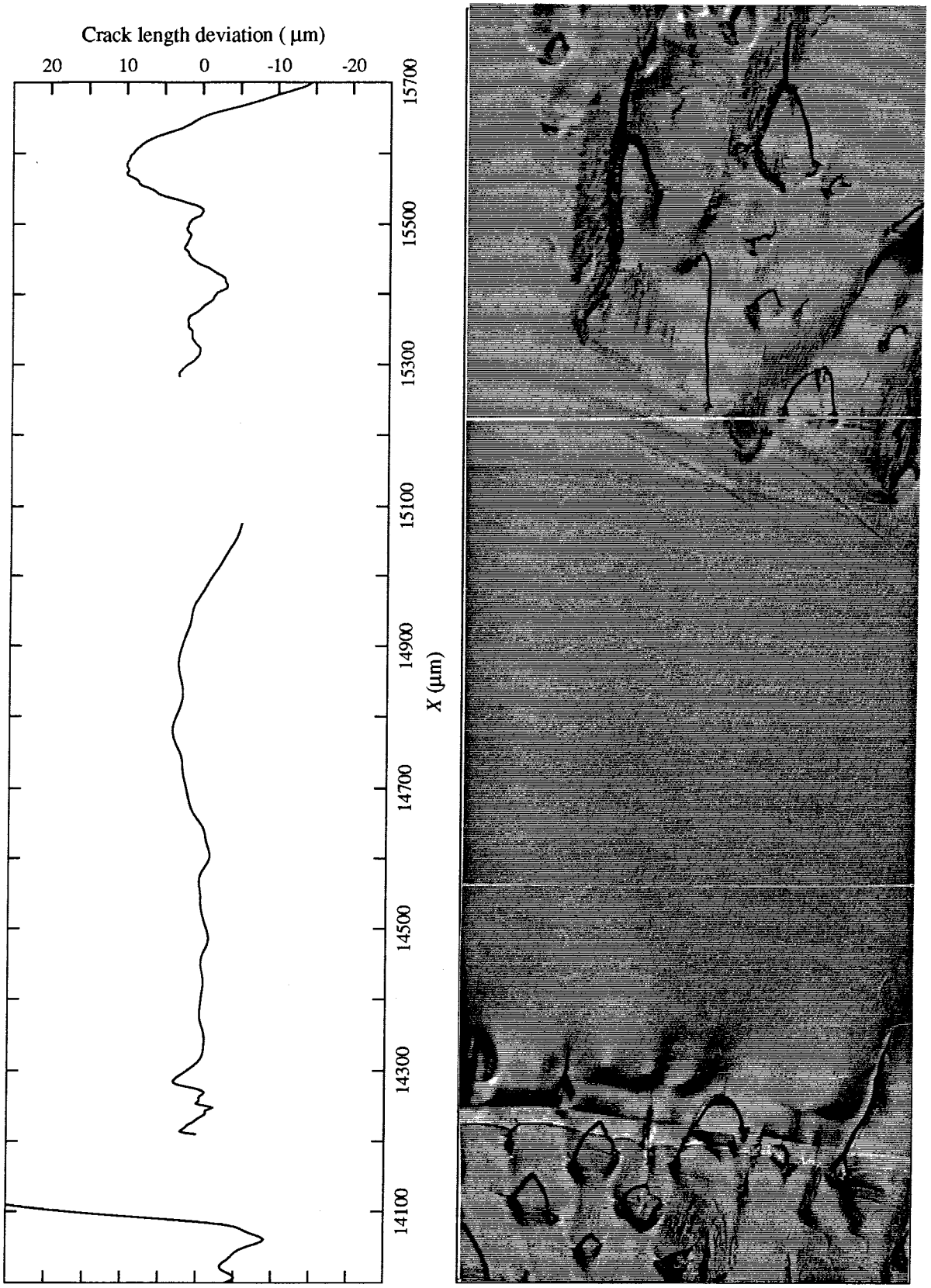

FIGURE 7 Crack length deviation and fracture surface morphology at high (0.8-1.0 Mpa $m^{1/2}$) and lower (0.7 Mpa $m^{1/2}$) stress intensity factors.

At this point a second test is started in which the stress intensity factor is reduced from 0.95 to 0.8 MPa $m^{1/2}$ (with a corresponding drop in the amplitude from 0.75 to 0.55 MPa $m^{1/2}$). As the crack begins to propagate at a slower rate and through the middle of a single craze, the fracture surface becomes smooth and the amplitude of the deviation decreases considerably. A third experiment where the stress intensity factor is raised to 1 MPa $m^{1/2}$ is started when the crack length reached 15200 μm. At that point, the crack begins to propagate through different planes and different crazes and its effect can be detected in the deviation record.

The most striking observation is that the periods of the oscillation in the deviation record, as well as the dimension of the features on the fracture surface are larger than the craze length. While there have been reports of crack propagation through multiple crazes [8], the length scales reported are on the order of the craze length; the case where the features have dimensions larger than in the 30 to 40 μm range is when "rib markings" appear in the fracture [4, 8]. However, these features are associated with fast crack propagation.

4.2 Constant Stress Intensity Factor Experiment

This section examines the fracture surface of a specimen where an experiment at constant stress intensity factor took place. The combined feedback technique was used to keep the stress intensity factor during the test at 0.60 MPa $m^{1/2}$ with its variation below 0.75%[13] as the crack propagated for about 15% of the length of the specimen. Five different tests at four different frequencies are used. The sequence is as follows: The first test is at a frequency of 1 Hz, the second at 3.2 Hz, the third at 1 Hz, the fourth at 0.32 Hz, and the last one at 0.1 Hz.

---

[13]A factor contributing to the variation is the slight change in Young's modulus that PMMA exhibits as it is tested at different frequencies.

In this particular experiment the features of interest occurred at the back edge of the specimen, whereas the high resolution crack length measurements were recorded on the front edge (free surface) of the specimen. For this reason both fracture surfaces are shown; at the end of the section some calculations of the frequency content (periods in the deviation) of the deviation record are made.

The optical micrographs of the fracture surface are shown in figures 8, 9 and 11. Figure 10 is an SEM photograph of details shown in figure 9. Starting with a crack length of 11000 μm in figure 8 an experiment at a frequency of 1 Hz is conducted until the crack length reaches 12400 μm. The fracture surface has a smooth appearance and the hue in the color photographs is very uniform and depends on the angle at which the fracture surface is viewed.[14] This type of observation was made by Berry [9] as he correctly pointed out that the colors were produced by an interference phenomena caused by a layer of oriented fibrils (i.e., the broken craze). Thus, because both surfaces show the same colors and because they are very uniform over areas much larger than the craze, one reaches the conclusion that the height of both layers is approximately the same and that the crack is breaking through the middle of the craze as it propagates.

The crack and craze front at the end of the 1 Hz test are shown at the bottom of figure 9. At that point a series of 3.2 Hz tests are conducted until the crack length reaches 13400 μm. The most prominent feature is the wedge-shaped region that develops almost as soon as the high-frequency test starts. In addition, both surfaces show complementary features inside the wedge: places where lines and features are sharply defined on one surface[15] correspond to places on the opposite surfaces that have a soft or out-of-focus appearance[16] (e.g., compare the places labeled AA' and BB').

---

[14]In this case, changing the magnification of the microscope objective changes the angle and (thus) the hue since each objective has a different numerical aperture.

[15]The color photographs show a set a well-defined color fringes next to the lines.

[16]No fringes are present in this area and the colors are different.

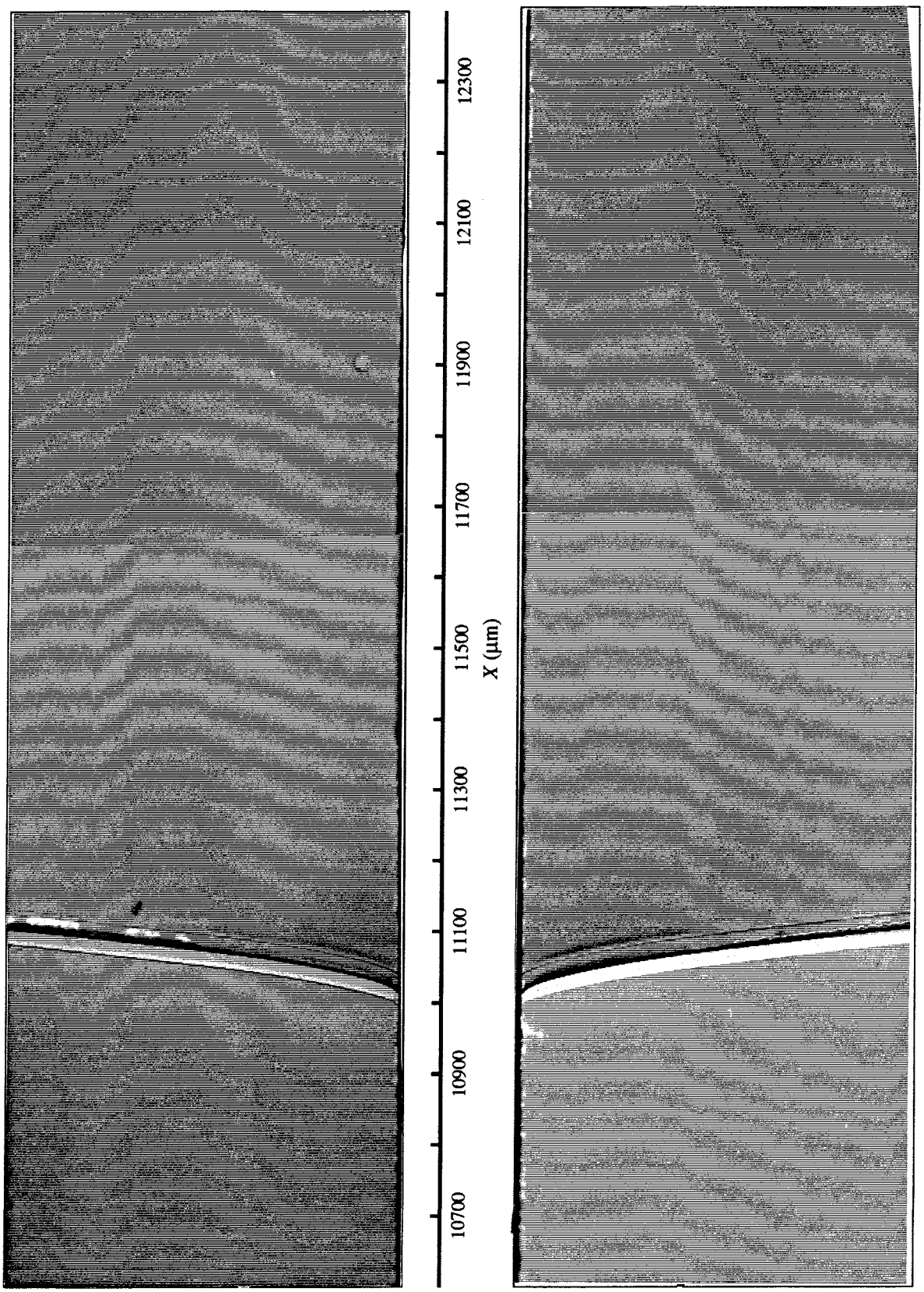

FIGURE 8 Fracture surface morphology at a constant stress intensity factor (0.60 Mpa $m^{1/2}$) and a test frequency of 1 Hz.

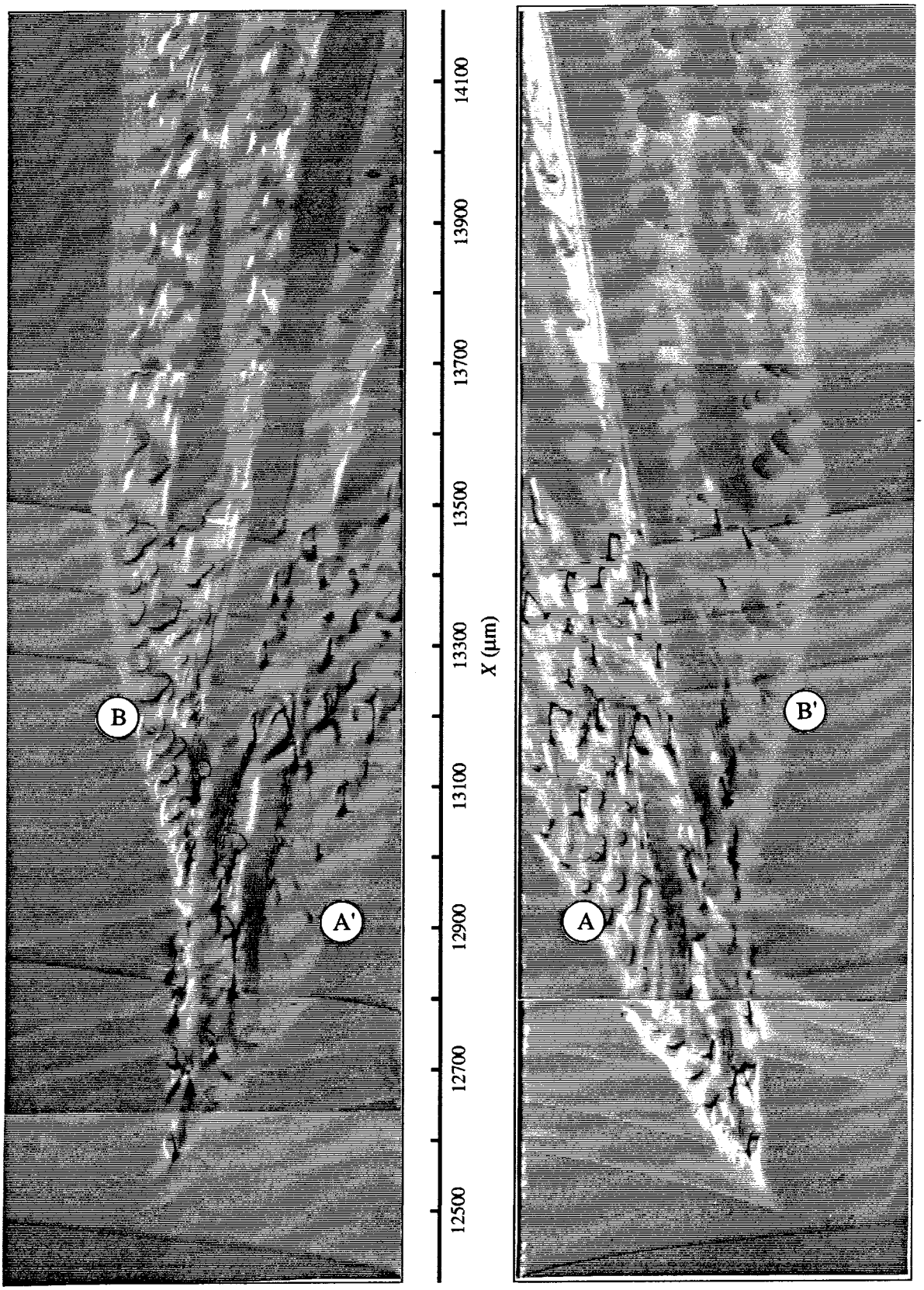

FIGURE 9 Fracture surface morphology at a constant stress intensity factor (0.60 Mpa $m^{1/2}$) and test frequencies of 3.2 Hz and 1 Hz.

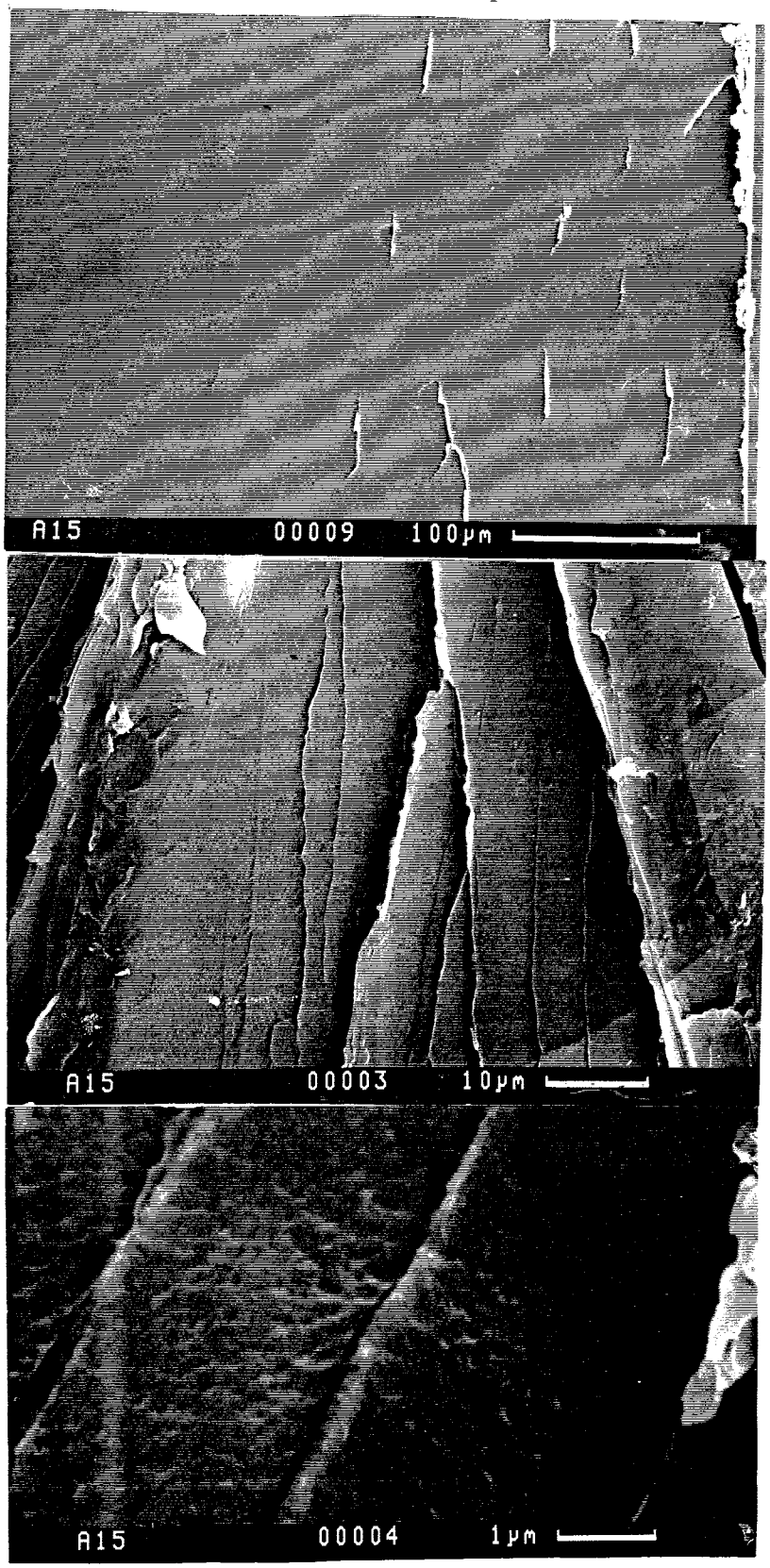

FIGURE 10 SEM photographs of wegde-shaped regions.

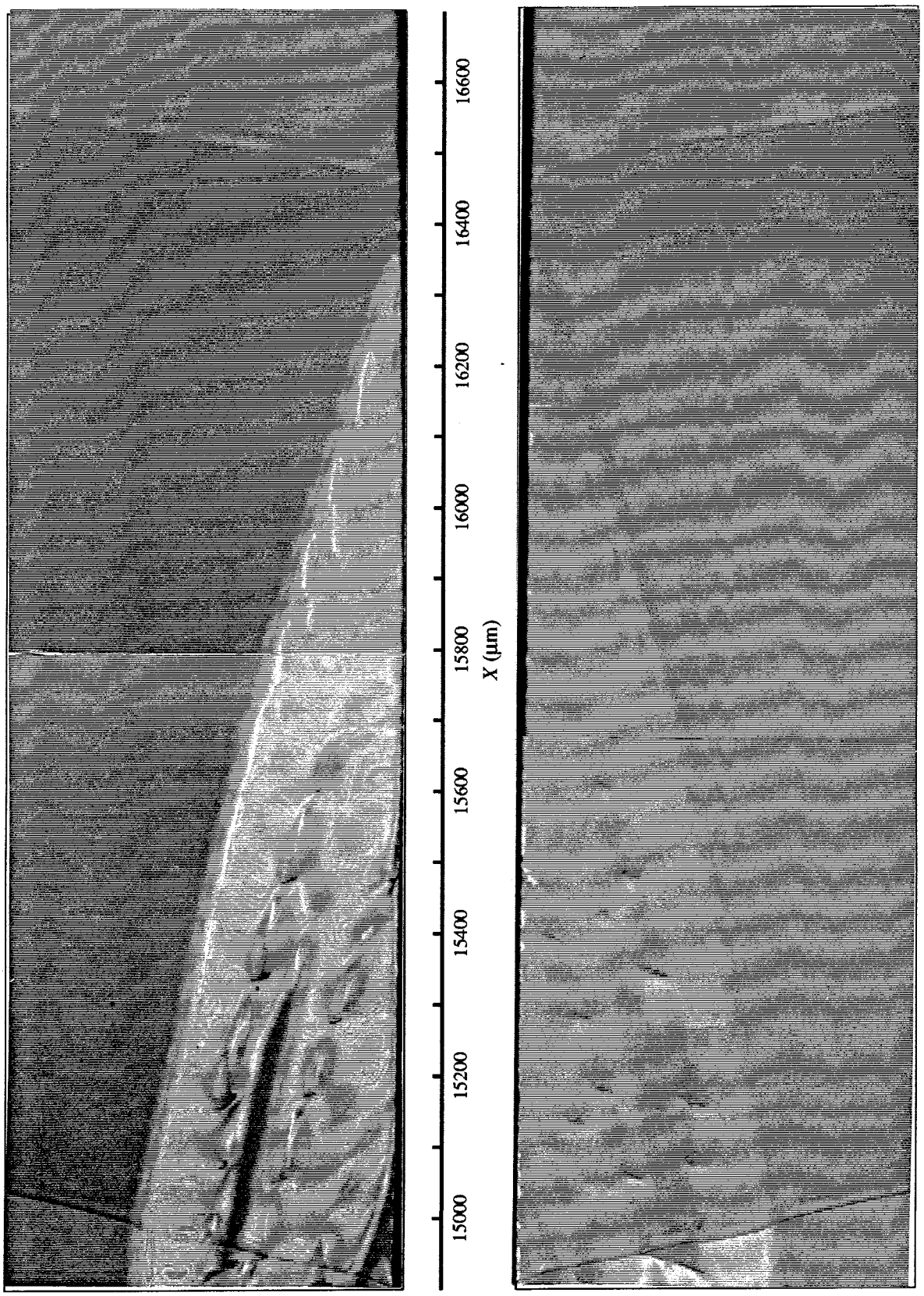

FIGURE 11 Fracture surface morphology at a constant stress intensity factor (0.60 Mpa $m^{1/2}$) and test frequencies of 0.32 Hz and 0.1 Hz.

The width of the wedge keeps increasing throughout the 3.2 Hz tests. The material outside the wedge has the same appearance (and hue) on both surfaces and it suggests that outside these regions the craze is breaking at the middle. The wedge-shaped regions were further investigated with the aid of a Scanning Electron Microscope (SEM).

The SEM photographs are shown in figure 10. The direction of crack propagation is from top to bottom. In the top photograph (lowest magnification) one can see that the wedge-shape region corresponds to a region where there are lines parallel to the direction of crack propagation. As the bottom two figures show, the (small) areas adjacent to the lines are composed of small "terraces" of different height; these terraces give rise to the color fringes in the color photographs and the "sharply-defined" areas in the black and white fractographs. From these observations one concludes that the crack does not break the craze in the middle but instead it breaks the craze at different heights. Thus, as the craze breaks, fibrils that are longer on one fracture surface correspond to places where the fibrils are short on the opposite one. Again, the length scale of these features is larger than the length of the craze. In this case the features (lines) range in dimension from 40 to 100 μm.

After the crack reached 13400 μm (figure 9) the frequency was reduced to 1 Hz and a new experiment was started. It should be noted that while the width of the wedge-shaped regions no longer increased, the regions themselves remained even though in the previous 1 Hz test the crack/craze system did not develop these regions. The experiment continued until the crack reached 14900 μm (shown at the bottom of figure 11).

As the frequency was reduced to 0.32 Hz the width of the regions gradually decrease until they disappear and the crack starts propagating in the so-called discontinuous mode in which the fracture surface is covered by bands which are smaller than the craze. The last 100 μm of crack propagation (at the top of the photograph) correspond to an experiment where the frequency is lowered to 0.1 Hz. The analysis of

the crack length record and its deviation of the features in the fracture surface that are smaller than the craze length is deferred to chapter 3 where the deviation is viewed in conjunction with the measurements of the craze and crack opening displacements. This section concludes with a Fourier analysis of an experiment where the wedge-shaped region have propagated long enough and have covered the whole thickness of the specimen.

The crack length deviation of an experiment where the wedge-shaped regions have covered the whole thickness of the specimen is shown in figure 12a. The amplitude of the deviations are on the order of 10 to 20 μm. The main frequency of the low frequency noise introduced by the choice of fitted function has been filtered by a low-pass filter in the frequency domain. The amplitude of the Fourier transform plotted against the period is shown in figure 12b. Before one could make use of the information presented the harmonics of the low frequency had to be identified. The procedure used in identifying them is as follows: An estimate of the period (or frequency) of the noise introduced by the fit was obtained from the unfiltered deviation (not shown); then the harmonics of the noise were plotted and adjusted until they covered most of the peaks. The harmonics are identified by the dashed lines. The information that remains has periods from about 60 to 100 μm which correspond very well with the features that are observed in the wedge-shaped regions.

It should be pointed out that a subjective judgment was used in deciding on the exact period of the low frequency noise (in this case 1150 μm). The decision was based on *a priori* knowledge of the length scale that were present on the fracture surface and second we wanted the harmonics to eliminate most of the peaks, including the ones at about 300 and 600 μm since they were clearly the first and second harmonics of the noise.

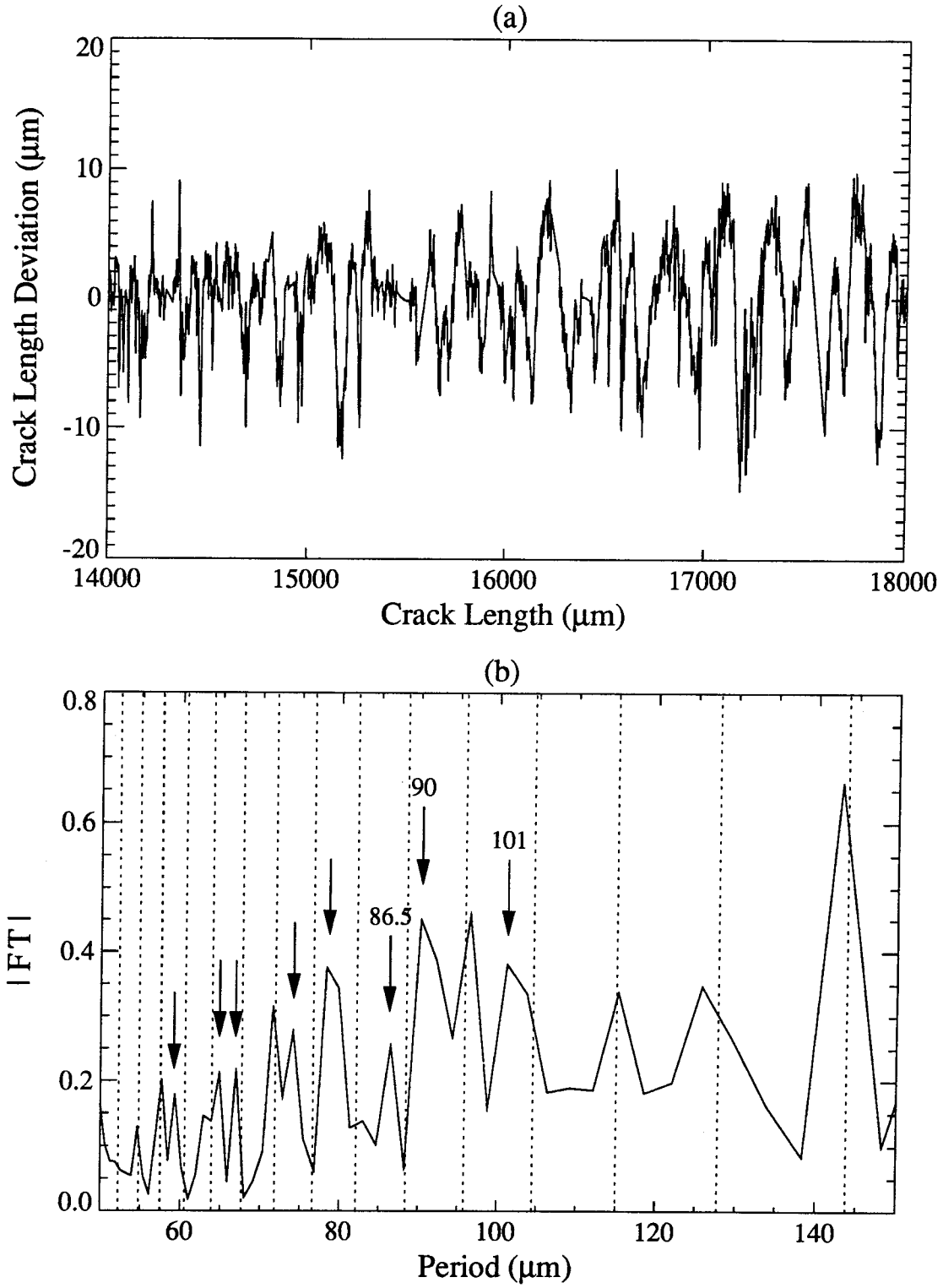

FIGURE 12 Crack length deviation record (a) and the magnitude of its Fourier transform (b).

While it has been found that the Fourier analysis can serve in obtaining a quantitative measure of the length scales that are present in the fracture surface and are captured by the crack length deviation, the Fourier analysis must be used with caution until a better way of dealing with the low frequency noise is found. This method would perhaps benefit from a Fourier analysis of different lengths (number of points) of the deviation record which would perhaps change the frequency content (and thus the harmonics) of the low frequency noise without a change of the information content.

5. Summary and Conclusions

The data suggests that under the prevailing loading conditions the crack propagates with a measurable acceleration, rather than exhibiting discrete and finite increments in length within the time frame of a cycle or less. Although there are instances when the crack appears to jump by a fraction of the craze length, most of the time the crack tends to accelerate rather than jump. This acceleration stage has typically the same character as a deceleration stage. The overall growth of a crack is thus not a matter of a distinct growth per cycle, but larger scale dimensions play a significant role here.

The deviations in the crack length record recorded on the surface of the specimen correlate well with the marking on the fracture surface and thus, the surface measurements reflect well what takes place inside the specimen.

High stress intensity failures are associated with multiple craze formations at the tip of a crack, which result in multiple sources of failure initiation to generate a rough surface with step-discontinuities. Sufficiently low stress intensity factors resulting in single crazes at the crack tip produce very smooth fractures surfaces, and produce accelerating and decelerating phases in he crack growth process. The length scales associated with these acceleration/deceleration phases are typically on the order of two to four times the length of the (single) craze. This indicates that the whole crack propagation process depends on the rate dependent interaction of the bulk material surrounding the craze and the rate dependent response of the craze material and the changes occurring within it.

The craze, the dimensions of which are on the order of 30 to 40 μm, is able to generate length scales on the fracture surface that are larger than its length, both when there is a single craze in front of the crack tip as well as when the crack tip is preceded by

multiple crazes. These length scales range anywhere from 50 to 250 μm. One possible explanation for generating these length scales derives from the coupling between the fibrillation at the tip of the craze and the disentanglement or rupture of the craze fibrils at the base of the craze (crack tip): Schirrer [10] discusses this coupling when he describes the "oscillating growth" observed in PVC; he argues that if the craze stress distribution is non-linear, rather than constant or corresponding to a simple proportionality along the craze axis, the feedback loop between these two processes could become unstable and the growth would exhibit oscillations. While he did not observe the details of the stress distribution in the craze, the studies reported here establish this nonlinear distribution clearly as outlined in the last chapter of this thesis.

Thus Schirrer's observation seems to fit the observations made here; however, the details of the "feed back loop" performance are not clear yet and are, most likely, not understood until extensive computational investigations are undertaken. Such investigations must be coupled, however, with a more thorough constitutive formulation of the bulk and craze materials, and in this way the present thesis contributes to the advance of knowledge for this further phase of crack/craze propagation understanding.

Returning to the reference of results delineated in the last chapter, namely, that the stress distribution within the craze is strongly non-linear, one can, nevertheless, offer some preliminary observations at this point. In this context the question must be raised whether or not this oscillating growth can have length scales that are larger than the length (of the craze) over which these processes take place. To answer this question let us assume, for the sake of argument, that the crack and craze propagate discontinuously in an idealized way such that on the average the crack jumps by one-half of the craze length every N[17] cycles. If the jump is longer than one-half of the craze length, one could argue that the next (second) increment would take a larger number of cycles because the fibrils

[17]Let N be a large number on the order of several hundred cycles.

left over in the craze have not accumulated enough damage[18] during the average number of cycles but require more time or more cycles to be brought to the state where the whole craze is ready for the next failure increment. By the same argument, the third jump would, therefore, occur before average N cycles have passed, which, in turn, would predispose the fourth one to take longer, and so on. This situation would repeat every $2N$ cycles and have periods of twice the one-half craze length.

Strictly speaking this model process would produce alternate accelerations and decelerations with a spatial scale on the order of the craze length, but hardly large multiples of that length scale. However, if the lag in this self-correcting mechanism is such that it take mN number of cycles where m is larger than 2 then the periods of this supra-scale length would be larger than the craze length, even though each individual jump has a length scale that is smaller than the craze length.

[18]We are aware that one can also argue that the shorter (than usual) craze length would generate higher stresses which would tend to damage the craze faster, thus generating a self-correcting growth condition. This implies that the craze possesses a "memory." However, the argument can still be made if one assumes that there is a lag in this self-correcting mechanism.

6. References

1. Hertzberg, R.W. and Manson, J.A., *Fatigue of Engineering Plastics,* 1st Edition, Academic Press, New York, 1980.
2. Döll, W. and Könczöl, L., "Micromechanics of Fracture under Static and Fatigue Loading: Optical Interferometry of Crack Tip Craze Zones," in *Advances in Polymer Science: Crazing in Polymers,* H.H. Kausch, Editor, Volume 91/92, pp. 137-214, Springer-Verlag, Berlin, 1990.
3. Elinck, J.P., Bauwens, J.C., and Homes, G., "Fatigue Crack Growth in Poly (Vinyl Chloride)," *International Journal of Fracture Mechanics*, Vol. 7, 277-287, 1971.
4. Washabaugh, P.D. and Knauss, W.G., "Nonsteady, Periodic Behavior in the Dynamic Fracture of PMMA," *International Journal of Fracture*, Vol. 59, No. 2, 189-197, 1993.
5. Hertzberg, R.W., Skibo, M.D., and Manson, J.A., *Journal of Materials Science*, Vol. 13, 1038-, 1978.
6. Gonzalez, R.C. and Wintz, P., *Digital Image Processing,* 2nd Edition, Addison-Wesley, Reading, 1987.
7. Press, W.H., et al., *Numerical Recipes: The Art of Scientific Computing,* Cambridge University Press, Cambridge, 1986.
8. Döll, W., "Fractography and Failure Mechanisms of Amorphous Thermoplastics," in *Fractography and Failure Mechanisms of Polymers and Composites,* A.C. Roulin-Moloney, Editor, pp. 387-436, Elsevier Science Publishers LTD, New York, 1989.
9. Berry, J.P., "Fracture Processes in Polymeric Material. 1. The Surface Energy of Poly(methylmethacrylate)," *Journal of Polymer Science*, Vol. 50, 107-115, 1961.

10. Schirrer, R., "Optical Interferometry: Running Crack-Tip Morphologies and Craze Material Properties," in *Advances in Polymer Science: Crazing in Polymers,* H.H. Kausch, Editor, Volume 91/92, pp. 215-261, Springer-Verlag, Berlin, 1990.

III. CRAZE BEHAVIOR IN PMMA: EFFECT OF LOAD HISTORY AND CRAZE DETERIORATION

Abstract

The craze and crack opening displacements are measured near the free surface of the specimen both under quasi-static step loading and cyclic loading. Eleven craze opening profiles for equal load increments are acquired during a single cycle under fatigue loading. A multi-linear craze stress model is used to match the opening displacements to the measurements. While the primordial thickness can be defined from the Lorentz-Lorenz equation and from the assumption of a constant index of refraction for the quasi-static loading, the effect of load history may prevent such determinations for cyclic loading. The damage accumulated through cyclic deformation reduces the strength of the fibrils in the middle of the craze and produces a drop in the middle of the stress distribution. The craze and crack opening displacement are monitored in connection with a jump-like crack/craze advance constituting 50% of the craze length. The newly-drawn craze fibrils after the jump show mechanical behavior that is different from their behavior before the jump and exhibit no deterioration in their stress-displacement relation.

1. Introduction

Crazes are the result of localized material instability in crack like geometries and represent a natural material response under suitable stress conditions in the transition to total material fracture. They usually involve material transformation from a basically random molecular structure to an oriented supramolecular configuration, with orientation in the direction of maximum principal tension stress. Because they are the prominent feature characterizing the transition of the bulk material to material failure at the tips of cracks they play one of the most important roles in the fracture process of these materials. While they are well recorded in and accepted for linear polymers, they have been mentioned without physical documentation to occur in cross linked ones; for the latter materials it is questionable whether the cross linking allows the molecule flow to proceed and generate the molecular/fibrillar orientation that is so characteristic of the classical crazing phenomenon. For this reason we think in the ensuing discussions mostly of uncrosslinked polymers .

The molecular orientation in the layer covering fracture surfaces had been noted by Berry [1] who deduced its (local) thickness from the variations in color shading. Hsiao and Sauer [2] identified the crack like geometry of crazes before fracture occurred. The first systematic study of the geometric craze zone and of the optical and (some) physical properties of craze material was supplied by Kambour [3-6]; amongst other results he found that the index of refraction of the craze in PMMA was 1.32, regardless of whether the craze was unbroken or resting stress free on traction free fracture surfaces. Many contributions to the mechanical behavior of crazes have been contributed by Kramer and his students [7-9]. A systematic study of craze behavior under cyclic loading was contributed by Döll [10-14] who concentrated on examining the effect of molecular

weight on fatigue response of PMMA in terms of craze behavior. His review articles [15, 16] still stand as excellent documents of the state of the art on this particular topic.

It appears that underlying all these studies is the assumption that the craze behavior is (rather) insensitive if not independent of the load history. While such an assumption may be justified for any initial investigation, it seems readily questionable in light of the fact that PMMA is not, even in its small strain state behavior, load history insensitive. Moreover, the reported phenomenon of "crack growth by jumps" [17] under cyclic loading intimates that history effects may be a strong component of craze break down and fracture.

Motivated by this background we set out to examine the deformation characteristics of crazes at crack tips under the load histories of slowly varying cyclical deformation as well as slow monotonic loading/unloading. Of particular interest is the determination of the force distribution offered by the (changing) craze fibrils along the crack/craze axis, in order to relate the craze deterioration to the possibly unsteady growth of the crack.

Considerations of this type require that one be able to observe the crack with surface measurements as are made conventionally, and through observations that illuminate the crack front profile through the thickness of the specimen. While the experimental arrangement to make the surface measurements have been discussed in chapter 2, this chapter delineates some of the observations made (as they relate to the craze behavior) as well as the experimental arrangement and analysis required for the evaluation of the optical data that is recorded through the thickness of the specimen. With the analysis of this data one can reconstruct the craze/crack profiles and deduce the cohesive forces at the crack tip. Prominent in these deliberations are the notion of the primordial thickness (primordial craze) and the concept or belief of a distinct difference in the index of refraction appropriate to the craze material and the bulk solid. These concepts are discussed in section 3. In order to deduce the cohesive forces supplied by the

craze across the crack front one draws on (linearly) elastic stress analysis delineated in section 4. With these tools available, the results for monotonic, slow loading and unloading are presented in section 5.1, while the fatigue counterpart is documented in section 5.2 including the observation of changes in the cohesive force distribution as the crack changes length incrementally under fatigue loading. The chapter concludes with an overall evaluation of the observations in section 6.

2. Experimental Set-up

This section discusses the experimental arrangement used to record the interferometric fringe pattern which is used later to reconstruct the craze/crack opening displacement profile. The details of the images that are seen by the CCD camera and are acquired and stored in the computer are also discussed. This optical set-up forms an integral part of the loading device that was described in chapter 1.

2.1 Optical Configuration

The schematic and photograph of the afocal optical system for recording the fringe pattern is shown in figure 1. The system consists of two lenses mounted back to back such that their focal points coincide; an arrangement that is termed afocal because the lens combination does not possess a focal length. An afocal system has the advantage that the size of the image is independent of its position. The size of the image (magnification) is determined by the ratio of the focal lengths of the individual lenses. In this system the front lens (closest to the specimen) is a microscope objective with a large working distance and a focal length of approximately 52 mm. The back lens is a telephoto lens with a focal length of 200 mm that is changed to 400 mm by a 2X tele-converter. Using these lenses the crack and craze are viewed by the CCD camera at a magnification of 8X.

The illumination is provided by a 5 mW diode laser collimated by a 10X Galilean beam expander; it is input to the optical system through a mirror and a polarizing beam-splitter. The polarization of the beam is such that the beam splitter reflects (turns) the light and directs it to the specimen through the afocal system and a 1/4-wave plate. A final mirror directs a 2.5 mm diameter beam through the specimen and illuminates a portion of the craze/crack front.

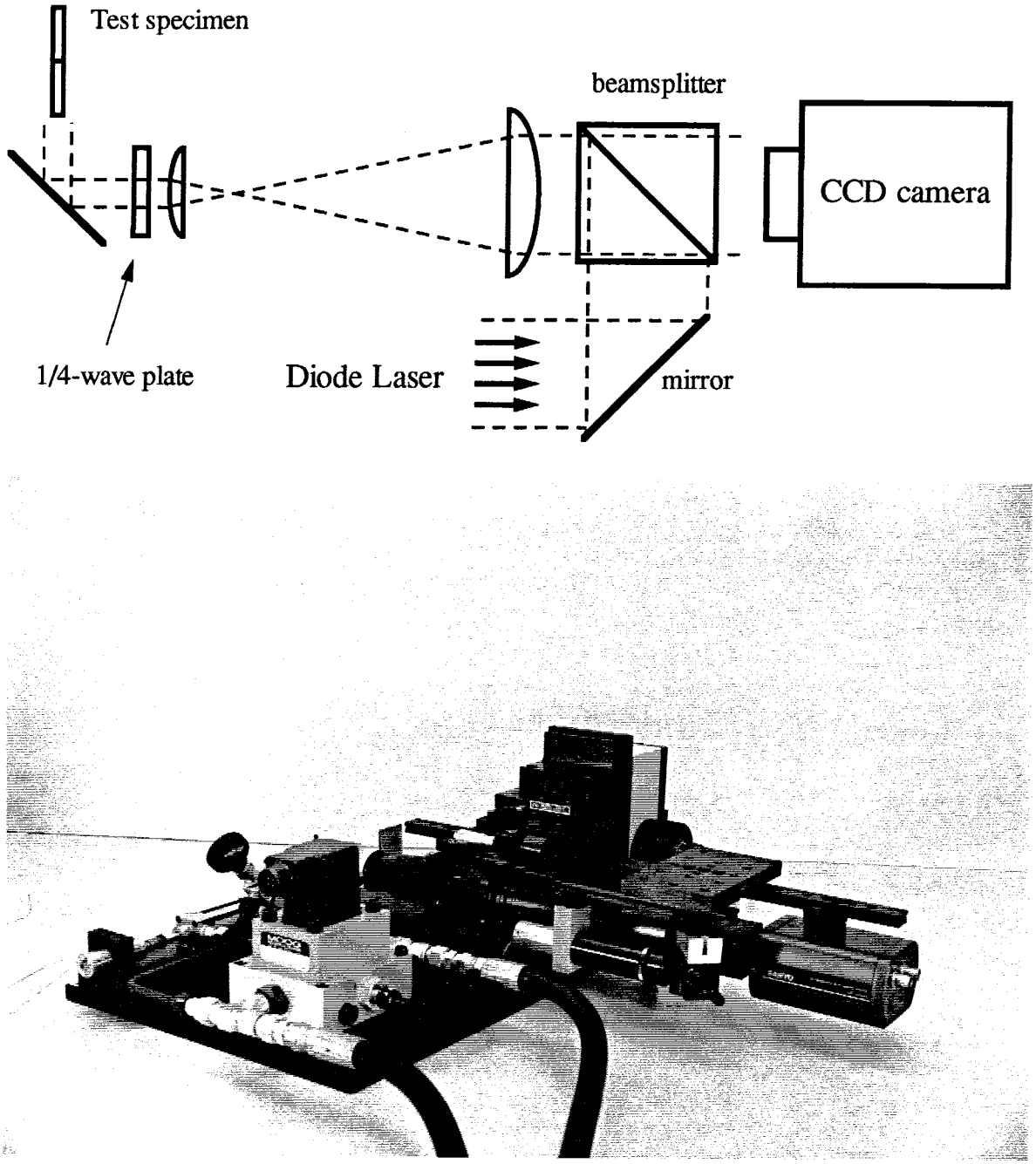

FIGURE 1 Schematic and photograph of the optical arrangement to record the fringe pattern of the craze and crack opening displacements.

Reflected light from the craze/crack (internal) interfaces is directed back into the optical system. As the light passes twice through the 1/4-wave plate its polarization has

changed (rotated by 90°) so that as it exits the afocal system the beam-splitter transmits the light to the CCD camera.

2.2 Data Acquisition

The CCD camera used for this study has a half-inch format with a CCD sensor that measures 6.4 mm by 4.8 mm; this sensor and the optical system make the field-of-view 0.87 mm by 0.68 mm. A frame-grabber inside the computer digitizes a TV frame into a 512x480 byte array. Thus, the size of the individual pixel turns out to be 1.70 μm in the x-direction and 1.41 μm in the y-direction.

A photograph of a digitized TV frame is shown in figure 2. The area at the top of the picture, which does not have any fringes, is the unbroken bulk material ahead of the craze. The broad and brighter set of (left-to-right) fringes that cover most of the photograph are from the crack opening displacement while the first three small fringes represent the craze opening displacement. The area where the fringes end (left side of the photograph) is the free surface (edge) of the specimen. It is on this surface where the optical system described in chapter 2 measures the crack length.[1] The region on the upper right of the photograph and denoted by the rectangle is a 64 x 128 pixel array that is monitored by the computer. The monitored area is always chosen to be close to the free surface[2] of the specimen so that the craze/crack opening displacements (COD) measurements can be correlated to the surface crack length measurements described in chapter 2.

---

[1]The vertical region that divides the fringe pattern in two is a region in which the craze breaks in layer of different height (as described in chapter 2) and diffracts the light enough that it does not reach the CCD camera.

[2]In most other studies the monitored area is chosen near the center of the specimen. The dimensions of the specimens are such that the recorded opening displacement can be considered to be under plane strain conditions. In this study the measurements are within the three-dimensional zone associated with the intersection of the crack front with the free surface.

Due to the large number of tasks that the computer must perform while an experiment is running and because of the large processing requirements in analyzing and storing visual data the computer does not acquire frames of the opening displacements continuously. Once every four cycles and during the minimum load of the cycle the computer grabs a frame and stores the 64 x 128 pixel byte array of the area that is being monitored. To study the load effects on the craze 11 frames are acquired during a particular cycle and the area under the monitored rectangle is stored for later analysis. The particular cycle when these operations take effect can be chosen by the operator or be programmed to occur at fixed intervals (typically every 100 cycles to avoid running out of disk storage).

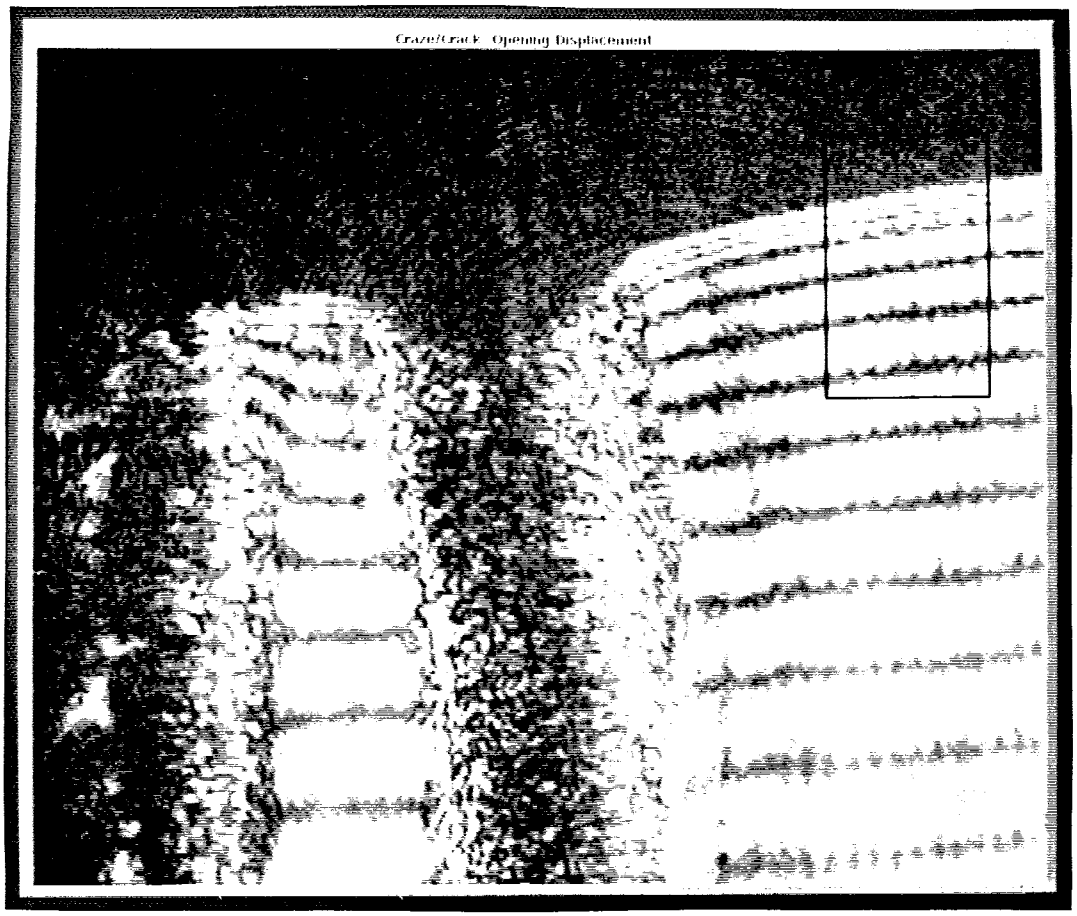

FIGURE 2 Digitized TV frame of the craze and crack opening displacements.

The computer analysis that turns the fringes into the opening displacements is carried out after the experiment finishes. It consists of filtering the fringes in the Fourier domain to remove high frequency noise using standard digital image processing techniques [18] and taking a cross-section of the fringe pattern to be unfolded into an opening profile; it is discussed in the next section.

3. Calculation of The Opening Displacement Profiles

In this section we sketch the steps that are necessary to reconstruct the craze and crack opening displacements from the recorded fringe pattern. We start with a simple two-beam interference phenomena, we then consider four-beam interference and later discuss the concept of the primordial thickness and how to obtain the index of refraction.

3.1 Preliminary Considerations

Light will be reflected at the boundary of two dielectric media if there is a change in the index of refraction across the interface. If a wedge of material is embedded in a medium of a different index of refraction, there will be some light reflected off each boundary due to the difference in refractive indexes.

Because of relevance to the craze geometry consider now the case when a plane wave polarized in the x-direction and propagating in the negative y-direction strikes a wedge having an index of refraction n and a thickness $2w(x)$ (see figure 3).

The electric field of the incident light of wavelength λ is given by

$$\mathbf{E}_i = \mathbf{e}_x E_0 \exp(-i(\omega t + ky)) \qquad (1)$$

where E_0 is its amplitude, ω its frequency and $k = 2\pi/\lambda$ its wave number; the electric fields of the reflected beams are

$$\begin{aligned} \mathbf{E}_1 &= \mathbf{e}_x \sqrt{r} E_0 \exp(-i(\omega t - ky)) \exp(i\varphi_1) \\ \mathbf{E}_2 &= \mathbf{e}_x \sqrt{r} E_0 \exp(-i(\omega t - ky)) \exp(i(\varphi_1 + 4knw + \pi)) \end{aligned} \qquad (2)$$

where $\mathbf{E}_1$ is the electric field of the light reflected at the upper boundary $\mathbf{E}_2$ is the electric field of the light reflected at the lower boundary, r is the reflection coefficient (assumed to be small) and φ_1 is an arbitrary phase angle.

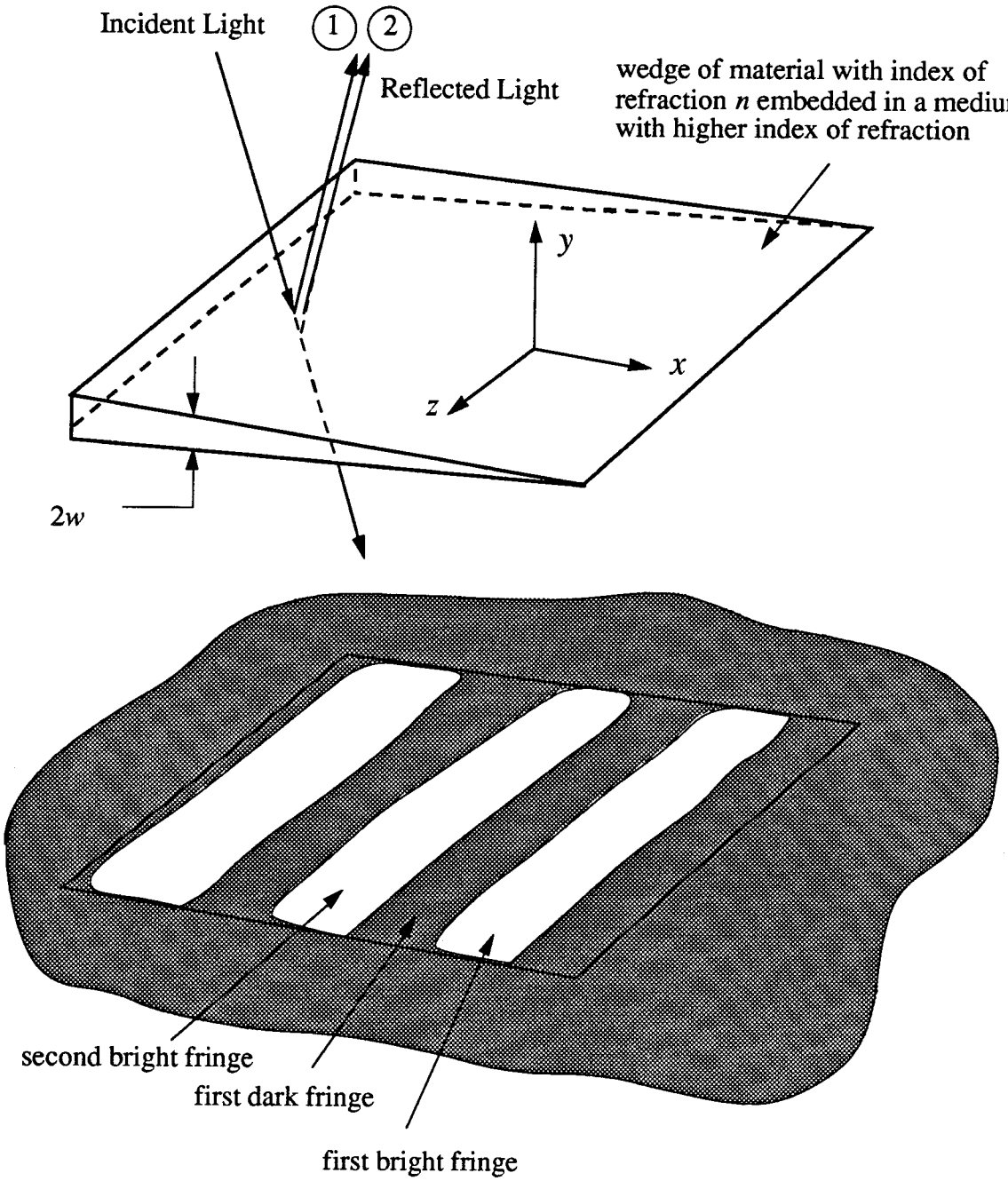

FIGURE 3 Reflected optical interference.

When the reflection off both boundaries is combined the light interferes forming dark and bright fringes. The intensity I of the reflected light will be proportional to

$$I \propto 4rE_0^2 \sin^2(2knw). \qquad (3)$$

The fringe at the tip of the wedge is dark because as light propagates into a medium with higher index of refraction there is a phase change of π (λ/2) [19] upon reflection. In this case the phase change occurs at the bottom boundary. Because the dark fringe at the tip of the wedge merges into the dark background the location of the tip cannot be determined from the fringe pattern *per se*.

The minima and maxima of equation 3 determine the location of the dark and bright fringes. Conversely, the (opening) profile of the wedge is given by

$$2w = \frac{\lambda}{4}\frac{1}{n}m \qquad m = 1,2,3,... \tag{4}$$

where m is the fringe order and odd integers correspond to bright fringes while even ones correspond to dark fringes. Thus, the (opening) profile of the wedge can be constructed from the location of the fringes if λ and n are known; however, the location of the tip of the wedge must be calculated by extrapolation or by some other means.

3.2 Craze Geometry

While the presence of a craze inside a material is somewhat similar to the situation described above, the presence of a crack embedded in the craze introduces two additional interfaces which deserve further consideration. The additional boundaries produce two additional reflected beams and their electric fields must be considered in determining the interference phenomena.

A cross-section of a crack and craze inside a material is schematically shown in figure 4. This section considers the situation in which the crack propagates through the middle of a craze of thickness $2w(x)$. As the crack propagates into the craze it leaves a layer of broken crazed material, having a thickness w_0, attached to each side of the elastic-plastic boundary.

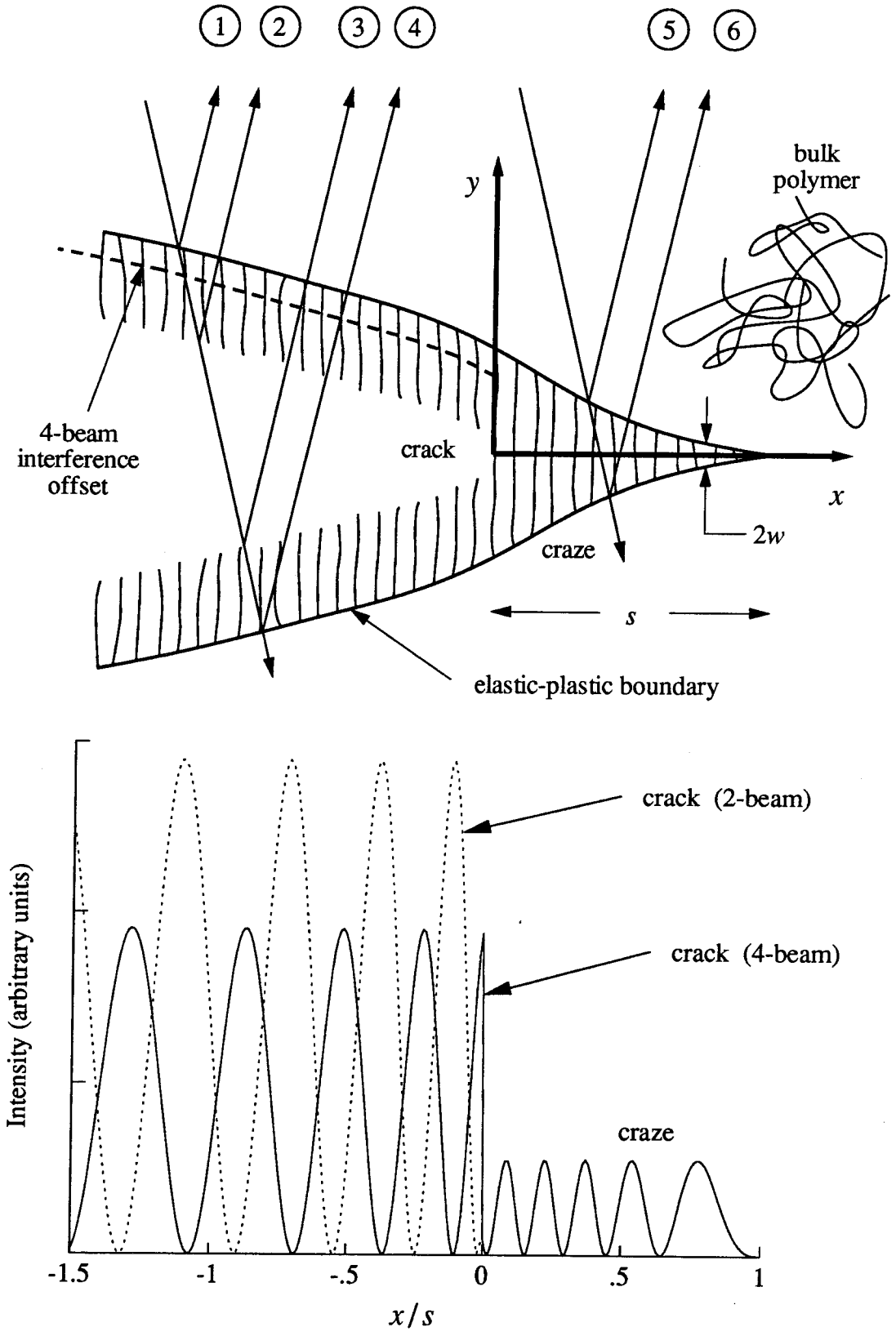

FIGURE 4 Craze/Crack schematic.

The interference from the reflected light along the crack is due to the combination of four beams (beams 1 through 4 in figure 4). If the incident light is the same as before then the electric fields of the four beams are given by

$$\begin{aligned}
\mathbf{E}_1 &= \mathbf{e}_x\sqrt{r_{BC0}}\,\mathrm{E}_0\exp(-i(\omega t-ky))\exp(i\varphi_1)\\
\mathbf{E}_2 &= \mathbf{e}_x\sqrt{r_{C0}}\,\mathrm{E}_0\exp(-i(\omega t-ky))\exp(i[k(\Delta-2(w-w_0))+\varphi_1])\\
\mathbf{E}_3 &= \mathbf{e}_x\sqrt{r_{C0}}\,\mathrm{E}_0\exp(-i(\omega t-ky))\exp(i[k(\Delta+2(w-w_0))+\varphi_1+\pi]).\\
\mathbf{E}_4 &= \mathbf{e}_x\sqrt{r_{BC0}}\,\mathrm{E}_0\exp(-i(\omega t-ky))\exp(i[2k\Delta+\varphi_1+\pi])
\end{aligned} \quad (5)$$

In equation (5) r_{BC0} is the reflection coefficient for the boundary between the bulk and the broken crazed material, r_{C0} is the reflection coefficient at the craze-air boundary, φ_1 is an arbitrary phase angle and

$$\Delta = 2(w-w_0)+2n_{C0}w_0 \quad (6)$$

is the optical path length through the crack together with the broken crazed material. The index of refraction in the broken craze is n_{C0}.

After some algebraic manipulations the intensity I of the reflected beam along the crack can be written as

$$I \propto 4r_{C0}\mathrm{E}_0^2\left(1+2\sqrt{r_{BC0}/r_{C0}}\cos(2kn_{C0}w_0)\right)\sin^2\left(2k(w-w_0)+\varphi\right), \quad (7)$$

where φ is given by

$$\tan\varphi = \frac{\sqrt{r_{BC0}/r_{C0}}\sin(2kn_{C0}w_0)}{1+\sqrt{r_{BC0}/r_{C0}}\cos(2kn_{C0}w_0)}. \quad (8)$$

If the width of the broken craze layer w_0 is constant, then φ is also constant and in this case the fringe pattern is shifted along the crack/craze axis by a constant amount. Thus, the introduction of two additional boundaries by the broken craze changes the

intensity of the fringe pattern and more importantly, it shifts the fringe pattern by a constant amount.[3]

The shift in the fringe pattern is equivalent to a crack-normal offset of the elastic-plastic boundary (see figure 4). The interference from the four reflected beams tracks a surface parallel to the elastic-plastic boundary. Reconstructing the position of the elastic-plastic boundary along the crack requires the knowledge of the horizontal phase shift or the crack-normal offset.

The fringe pattern along the craze results from the interference of the two beams reflected off the elastic-plastic boundary. The intensity I of the fringe pattern is given by

$$I \propto 4 r_{BC} E_0^2 \sin^2(2 k n_C w) \tag{9}$$

where r_{BC} is the reflection coefficient for the boundary between the bulk and the craze and n_C is the index of refraction inside the craze.

The elastic-plastic boundary can be determined from the extrema of equations 7 and 9 as follows:

$$\begin{aligned} 2w &= \frac{\lambda}{4}\frac{1}{n_C} m \quad m = 1,2,\ldots,m_C \\ 2w &= \frac{\lambda}{4} m - \frac{\lambda}{4}\frac{m_C}{n_C} + \text{offset} \quad m = m_C + 1, m_C + 2,\ldots \end{aligned} \tag{10}$$

The first equation determines the elastic-plastic boundary along the craze where there are m_C number of extrema. The second equation determines the elastic-plastic boundary along the crack.

The reconstruction of the elastic-plastic boundary requires the knowledge of four quantities: λ, n_C, m_C, and the offset. The wavelength λ is a chosen parameter and thus, is

---

[3] A four-beam interference analysis was performed by M. J. Doyle [20] for a craze that contained an internal region of constant thickness and different index of refraction. He found that the introduction of the two additional interfaces caused the bright fringes to have an alternating intensity.

known *a priori*. The calculation of n_C is discussed in the next section and the remainder of this section focuses on the calculation of m_C and the offset.

The number of extrema in the craze can be determined from the fringe pattern once a distinction is made between the crack and craze fringes. The fringes along the craze have a different amplitude than those along the crack since the amplitude of the fringes depends on the reflection coefficients (see equations 7 and 9) which themselves depend on the change in the indices of refraction across a boundary. The indices of refraction are such that for a craze in front of a crack in an unloaded specimen the amplitude of the fringes along the craze is about 20% of the amplitude of those along the crack. As the specimen is loaded the difference in amplitude decreases and it becomes more difficult to determine the location of the crack tip. However, by examining a sequence of fringe patterns of the opening displacement as the specimen is loaded, it is possible to track the location of the crack tip and thus distinguish between the two sets of fringes. Once the distinction between the two set of fringes is made the number of extrema in the craze m_C can be determined.

While the offset can be calculated from the thickness and the index of refraction of the broken craze layer, it can also be calculated from the requirement that the elastic-plastic boundary be continuous at the crack tip. It is the continuity condition that is used to calculate the offset in the following manner: First, the offset is assumed to be zero and the elastic-plastic boundary is constructed according to equation 10. Second, a smooth function (typically a 2nd order polynomial in x or y) is least-square-fitted separately to the craze and crack portions of the elastic-plastic boundary. Third, the fitted functions are extrapolated to the crack tip and the offset becomes the difference in the calculated values. Finally, the offset is added to the crack portion of the elastic-plastic boundary.

3.3 Constant Index of Refraction and the Primordial Thickness

In order to reconstruct the elastic-plastic boundary the index of refraction of the craze must be known. The calculation of the index of refraction is based on the Lorentz-Lorenz equation [19] which relates the index of refraction of a transparent dielectric medium to its density. If one assumes that the craze extends without changing its in-plane dimensions then the density is inversely proportional to the thickness of the craze $2w(x)$ and the Lorentz-Lorenz equation can be written as

$$\frac{n^2-1}{n^2+2}2w = \text{const.} \qquad (11)$$

For the equation to be useful it must be referred to a known state (index of refraction and thickness). Kambour determined the index of refraction of unloaded crazes in several glassy polymers by measuring the angle of total internal reflection [5]. For an unloaded craze in PMMA Kambour determined the index of refraction to be 1.32.

If one assumes that the index of refraction is constant through the craze then equation 11 can be written in terms of the number of extrema in the craze portion of the fringe pattern. Let m_0 be the number of extrema in the unloaded craze, and let the index of refraction of the unloaded craze be n_{C0}[4]. The Lorentz-Lorenz equation then becomes

$$\frac{n_C^2-1}{n_C^2+2}\frac{m_C}{m_0} = \frac{n_C}{n_{C0}}\frac{n_{C0}^2-1}{n_{C0}^2+2}. \qquad (12)$$

This cubic equation is plotted in figure 5. For the experimental profiles the ratio of extrema varies between 1 and 2.6, so that the index of refraction varies between 1.32 and 1.10. Thus, once the number of extrema in the craze is known, the (constant) index of refraction in the craze can be obtained from equation 12.

---

[4]In the previous section n_{C0} referred to the index of refraction of the broken craze layer. As it turns out Kambour later measured the index of refraction of this layer [4] and found it to be equal to 1.32, the same as the unloaded craze.

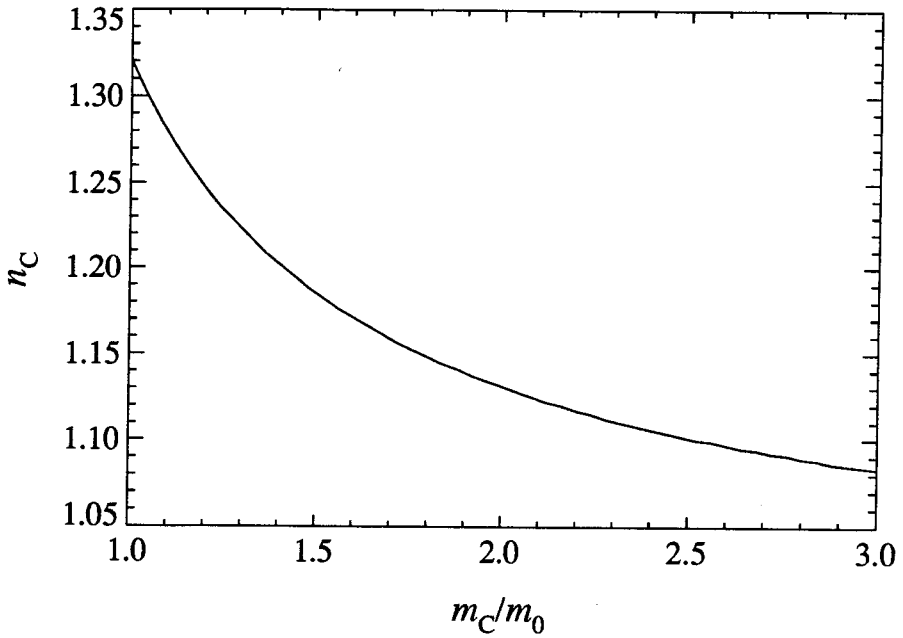

FIGURE 5 Index of refraction in the craze as a function of the ratio of extrema in the craze to that of the "unloaded" craze.

A second reference state for the Lorentz-Lorenz equation is the bulk polymer. Crazes are formed by a phase transformation of the bulk polymer into aligned fibrils [7]. The layer of bulk polymer is transformed into crazed material called the primordial thickness. A schematic representation is shown in figure 6. Denote the primordial thickness by τ; then from the Lorentz-Lorenz equation we obtain

$$\tau(x) = 2w(x)/\Lambda, \tag{13}$$

where Λ is the extension ratio representing the stretching of the primordial thickness to the current elastic-plastic boundary. The extension ratio is given by

$$\Lambda = \frac{n_B^2 - 1}{n_B^2 + 2}\frac{n_C^2 + 2}{n_C^2 - 1}. \tag{14}$$

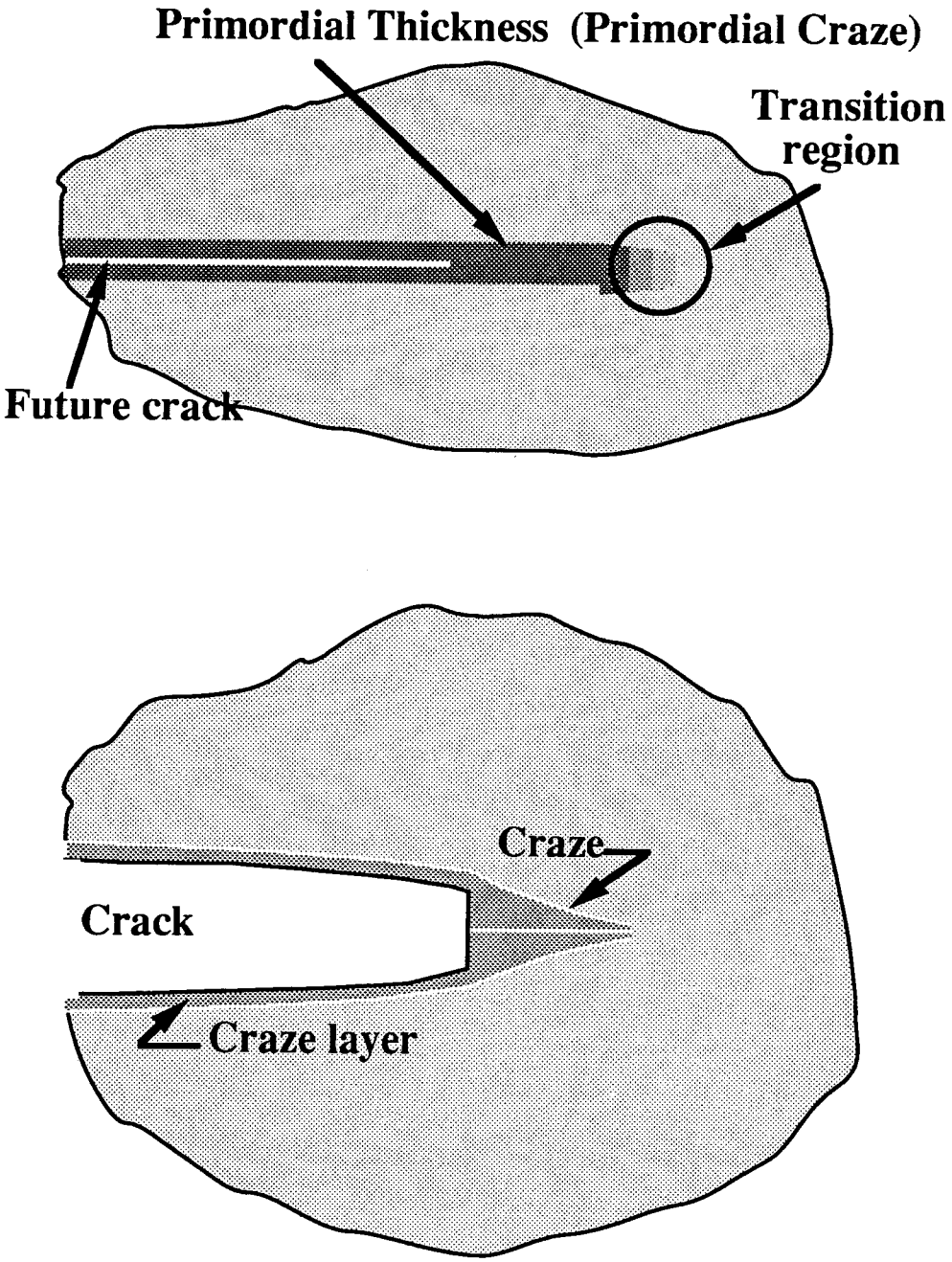

FIGURE 6 Schematic of the primordial craze.

For an index of refraction of the bulk polymer of 1.49 [4] and of 1.32 for the unloaded craze the extension ratio of the unloaded craze is 1.46, or a craze composition that is 69% polymer and 31% voids.

3.4 Variable Index of Refraction

Under the assumption of a constant index of refraction throughout the craze, one can reconstruct the elastic-plastic boundary for each fringe pattern. In addition, using equations 14 and 13 the extension ratio and the primordial thickness can be calculated. If the profiles correspond to different loading conditions of the same craze all of the primordial thicknesses should be the same. If the primordial thicknesses computed from data obtained under different loads differ from one another, the index of refraction is allowed to vary throughout the craze to make all of the primordial thicknesses coincide.

The procedure to perform these calculations is as follows: Assuming that one knows the primordial thickness, let the index of refraction be piece-wise constant throughout the craze so that

$$2w(x_i) = 2w(x_{i-1}) + \frac{\lambda}{4}\frac{1}{n_C(x_i)}. \qquad (15)$$

Then, combining equations 13 and 14 one writes a cubic equation for $n_C(x_i)$

$$n_C^3\left(\frac{2w(x_{i-1})}{\tau(x_i)} - \frac{n_B^2-1}{n_B^2+2}\right) + (n_C^2-1)\frac{\lambda}{4}\frac{1}{\tau(x_i)} - n_C\left(\frac{2w(x_{i-1})}{\tau(x_i)} + 2\frac{n_B^2-1}{n_B^2+2}\right) = 0. \quad (16)$$

Using equations 15 and 16 one can reconstruct the opening profile starting at the craze tip ($2w(x_0)=0$) and continuing toward the crack tip where the x_i's are the location of the fringe extrema.

The above procedure requires the knowledge of the primordial thickness. One way to obtain it is to assume that at least one profile in the set corresponds to a constant index of refraction throughout the craze; in that case equation 12 is used to obtain the index of refraction and the primordial thickness is calculated from equation 13. For later reference it should be noted that in fatigue experiments it is common to choose the lower load limit in the cycle low enough to assume that the index of refraction in the craze is that of the "unloaded" craze [21].

4. Stress Calculation

Once the elastic-plastic boundary has been constructed and the primordial thickness is known an analysis that relates the stresses to the net displacements can be formulated.

Here we seek a relation between the net displacement of the elastic-plastic boundary and the distribution of stress acting on the craze, that is

$$2v(x) \equiv 2w(x) - \tau(x) = \text{fnc}(\sigma_{CZ}(x)). \tag{17}$$

Dugdale considered the problem of a constant stress distribution [22]. The displacement associated with the Dugdale model was obtained by Goodier and Field [23] and a simpler expression was later obtained by Rice [24].

This study develops an expression for the net displacement of the elastic-plastic boundary as a function of a general stress distribution along the craze following the analysis of Ungsuwarungsri and Knauss [25] with some minor modifications: the coordinate system is located at the crack tip, the stress distribution is piecewise continuous and the craze length is considered to be small with respect to the crack length (small scale yielding).

Using the Westergaard stress function method [26] the solution to the problem of a crack of length $2c$ embedded in an infinite plate and loaded by 2 pairs of point loads as shown in figure 7 is given by

$$\begin{aligned} 2v(x') &= \frac{2P}{\pi \tilde{E}} \ln \left| \frac{\sqrt{c^2 - x'^2} + \sqrt{c^2 - T^2}}{\sqrt{c^2 - x'^2} - \sqrt{c^2 - T^2}} \right| \\ K_I &= \frac{2P}{\sqrt{\pi c}} \frac{c}{\sqrt{c^2 - T^2}} \end{aligned} \tag{18}$$

where $\tilde{E}$ is the reduced modulus ($\tilde{E} = E$ the Young's Modulus for plane stress and $\tilde{E} = E/(1-\upsilon^2)$ for plane strain, with υ being Poisson's Ratio).

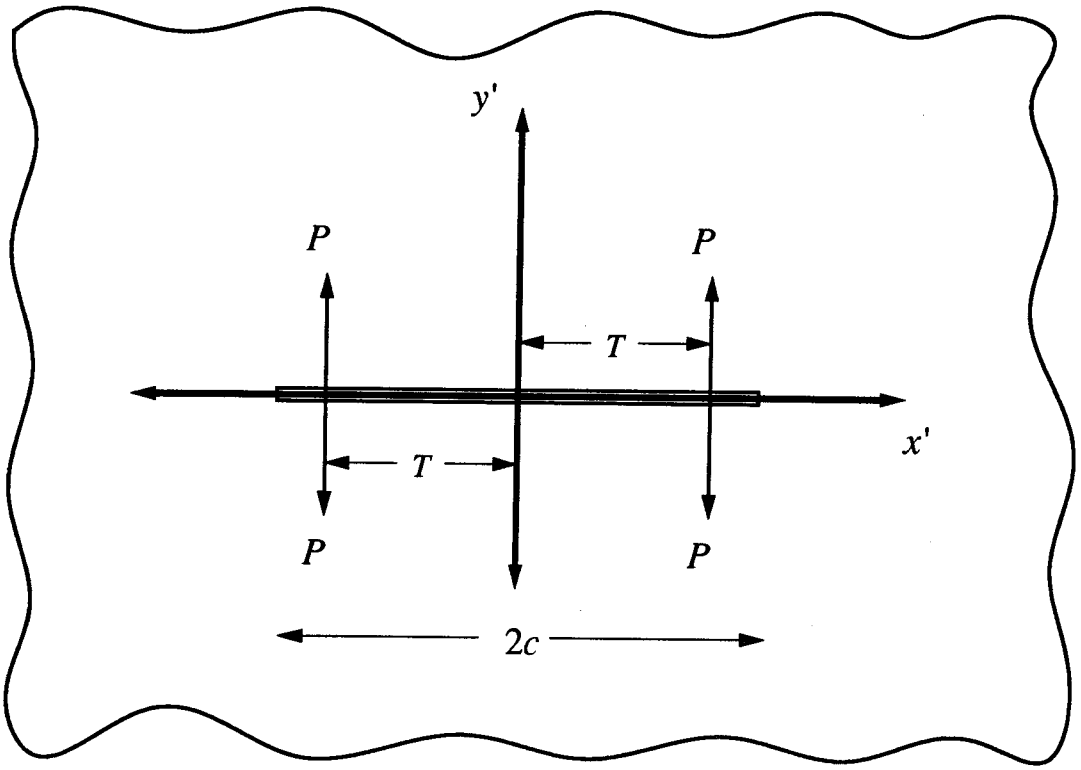

FIGURE 7 Crack of length $2c$ embedded in an infinite plate and loaded by 2 pairs of points loads.

The solution to the problem of an elastic plate loaded by far-field tension and by an arbitrary stress distribution acting over a portion of the crack (i.e., along the craze) as shown in figure 8 can be obtained by superposition [27] of three elastic problems, one of which is the problem described above. The (net) displacement is given by

$$2v(x') = \frac{2}{\tilde{E}}\left[\sigma_\infty\sqrt{c^2 - x'^2} - \frac{1}{\pi}\int_a^c P(T')\ln\left|\frac{\sqrt{c^2 - x'^2} + \sqrt{c^2 - T'^2}}{\sqrt{c^2 - x'^2} - \sqrt{c^2 - T'^2}}\right| dT'\right] \qquad (19)$$

while the stress intensity factor is given by

$$K_I = \sigma_\infty\sqrt{c\pi} - 2\sqrt{c/\pi}\int_a^c \frac{P(T')}{\sqrt{c^2 - T'^2}}\,dT'. \qquad (20)$$

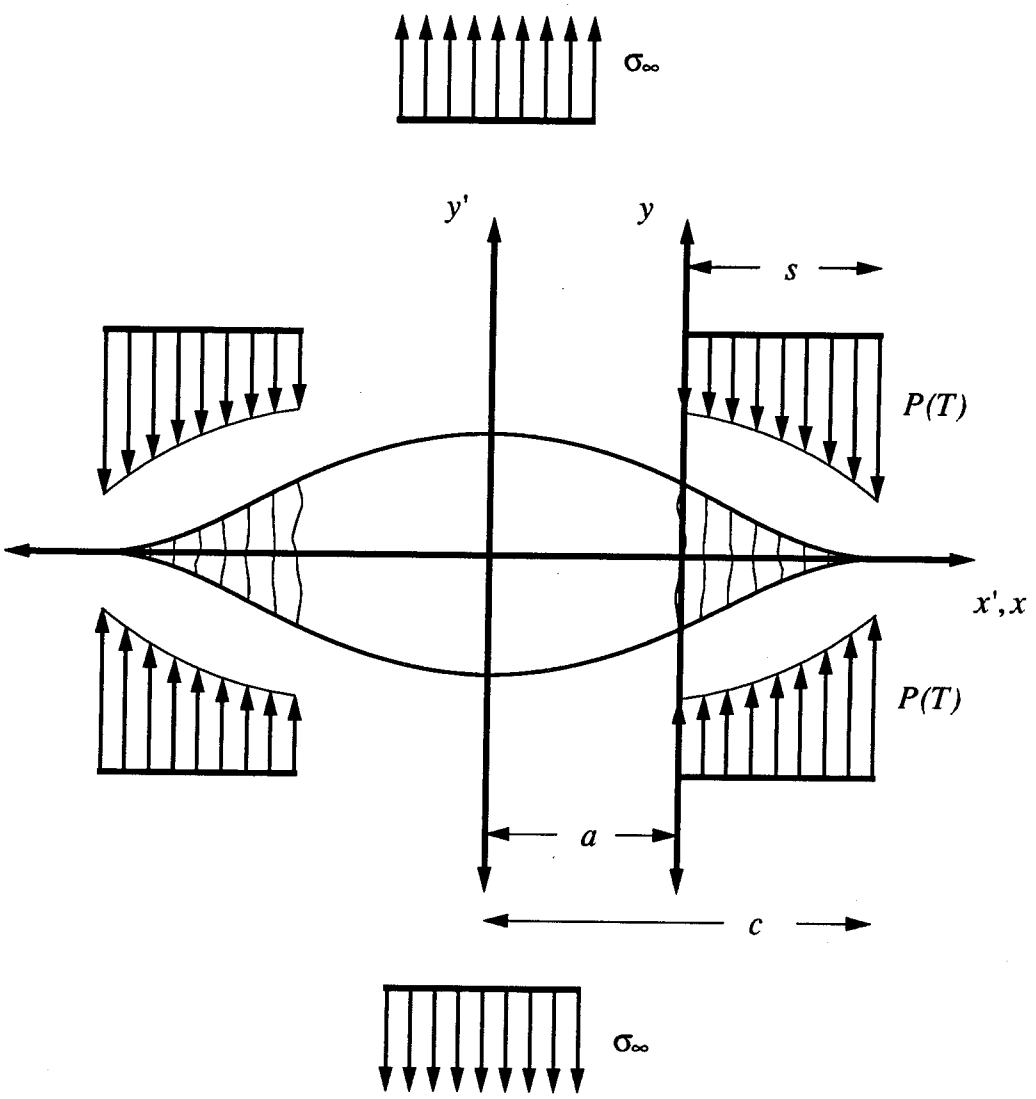

FIGURE 8 Elastic plate under far-field tension containing a crack of length $2c$ with a craze of length s at each crack tip.

Changing to the coordinate system located at the crack tip[5] and still assuming that the craze length $s=c-a$ is small compared to the crack length a then, after some algebraic manipulation, the displacement can be written as

$$2v(x)=\frac{2}{\tilde{E}}\left[\sigma_\infty\sqrt{2sc}\sqrt{1-x/s}-\frac{1}{\pi}\int_0^s P(T)\ln\left|\frac{1+\sqrt{\frac{1-x/s}{1-T/s}}}{1-\sqrt{\frac{1-x/s}{1-T/s}}}\right|dT\right] \quad (21)$$

[5]We now define the crack length to be a (as opposed to c) so that the crack tip will be located at the base of the craze and the crack faces will be stress-free.

while the stress intensity factor becomes

$$K_I = \sigma_\infty \sqrt{c\pi} - \sqrt{2/\pi s}\int_0^s \frac{P(T)}{\sqrt{1-T/s}}dT. \qquad (22)$$

If, following Dugdale, one sets the (local) stress intensity factor equal to zero equation 22 becomes a constraint condition and can be written as

$$\int_0^s \frac{Q(T)}{\sqrt{1-T/s}}dT = 2s \qquad (23)$$

where $Q(T)$ is the non-dimensional stress across the craze and is given by

$$Q(T) = P(T)/\sigma_D. \qquad (24)$$

The Dugdale stress σ_D is related to the far-field tension or to the (prescribed) far-field stress intensity factor by

$$\sigma_D = \pi\sqrt{c/8s}\sigma_\infty = \sqrt{\pi/8s}K_I. \qquad (25)$$

If one defines the Dugdale opening displacement as

$$2v_D = \frac{K_I^2}{\tilde{E}\sigma_D} = \frac{8s}{\pi\tilde{E}}\sigma_D \qquad (26)$$

then equation 21 becomes

$$2v(x) = 2v_D\left[2\sqrt{1-x/s} - \frac{1}{2s}\int_0^s Q(T)\ln\left|\frac{1+\sqrt{\frac{1-x/s}{1-T/s}}}{1-\sqrt{\frac{1-x/s}{1-T/s}}}\right|dT\right]. \qquad (27)$$

Equation 27 together with equation 23 are the basis for obtaining the (net) displacements of the elastic-plastic boundary for an arbitrary stress distribution along the craze such that the stresses are bounded at the craze tip.

The procedure to deduce a stress distribution along the craze from the measured displacements is to write equation 27 for a particular stress distribution in terms of some parameters and then to perform a least-squares fit to find the value of the parameters. In

this study we divide the craze into N segments and allow the stresses within each segment to vary linearly.[6]

A trapezoidal stress distribution is shown in figure 9. The integrals in equations 23 and 27 can be evaluated explicitly when $Q(T)$ is constant or proportional to T. The details for obtaining a final expression of the displacement in terms of the parameters that characterize the stress distribution are carried out in the appendix. Here only the final result is presented

$$\frac{2v(x)}{2v_D} = 2\xi + \frac{3}{2\xi_{N-1}} \frac{fv2 - x_{N-1} fv1}{\Delta_N}\Bigg|_{x_{N-1}}^{s} +$$

$$Q_0 \left\{ -\frac{fv2 - x_1 fv1}{\Delta_1}\Bigg|_0^{x_1} - \frac{3}{2\xi_{N-1}} \left(1 - \frac{2s}{3x_1}(1 - \xi_1^3) \left(\frac{fv2 - x_{N-1} fv1}{\Delta_N} \right)_{x_{N-1}}^{s} \right) \right\} +$$

$$\sum_{i=1}^{N-1} Q_i \left\{ \begin{array}{l} \dfrac{fv2 - x_{i-1} fv1}{\Delta_i}\Bigg|_{x_{i-1}}^{x_i} - \dfrac{fv2 - x_{i+1} fv1}{\Delta_{i+1}}\Bigg|_{x_i}^{x_{i+1}} \\ + \dfrac{3}{2\xi_{N-1}} \dfrac{fv2 - x_{N-1} fv1}{\Delta_N}\Bigg|_{x_{N-1}}^{s} \left(\dfrac{fq2_i - x_{i-1}\xi_i}{\Delta_i} + \dfrac{fq2_i - x_{i+1}\xi_i}{\Delta_{i+1}} - \dfrac{2s}{3} \left(\dfrac{\xi_{i-1}^3}{\Delta_i} + \dfrac{\xi_{i+1}^3}{\Delta_{i+1}} \right) \right) \end{array} \right\} \qquad (28)$$

The functions $fv1, fv2$, ξ, and $fq2$ are defined in the appendix. The expression above does not include the variable Q_N since the constraint condition was used to eliminate it. Upon multiplying through by $2v_D$ the displacement can be expressed in terms of N+1 functions that have N+1 linear coefficients. A least squares fit (LSF) procedure using Singular Value Decomposition [29] is used to find the value of $2v_D$ and the Q's that give the best fit for the experimental and calculated displacements.

[6] In 1985 Imai and Ward used a bi-linear stress distribution across the craze in their fatigue study in PMMA [28].

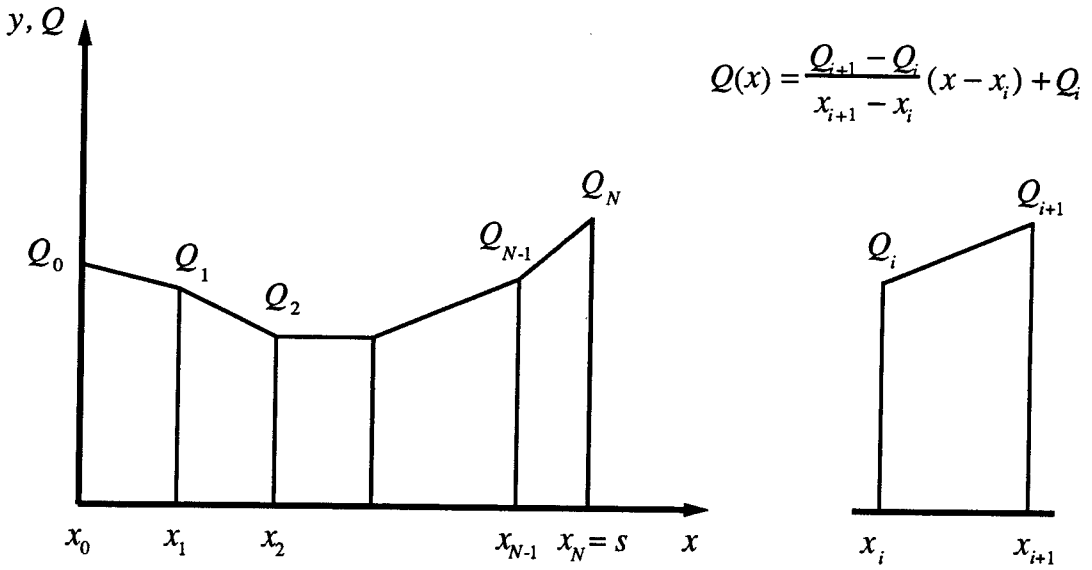

FIGURE 9 Discretization of the stress along the craze.

The number of segments N, as well as their location, used to characterize the stress distribution along the craze is chosen independently of the number and position of the extrema along the craze portion of the fringe pattern. Data from both the craze opening displacement as well as the crack opening displacement is used in the LSF procedure since both opening displacements depend on the craze stress distribution.[7]

The procedure to determine the best fit between the calculated and the experimental displacements is to systematically divide the craze into N segments of the same width and to perform the LSF. We start with the Dugdale model (1 segment with both end stresses equal to each other) and proceed with N= 1 up to N= 10. An example of this procedure is illustrated in figure 10 where the top figure shows the experimental and calculated

[7]One would expect from Saint-Venant's principle that the crack opening displacement will be independent of the details in the craze stress distributions as the point of observation is moved far away from the craze. However, the crack opening displacement is sensitive to the craze stresses near the crack tip. Thus, it is advantageous to use also the crack opening displacement in determining the distribution of stress along the craze. In this study crack opening displacements within 3 craze lengths of the crack tip are used in the LSF procedure.

crack/craze opening displacements (COD[8]) normalized by the primordial thickness (under a constant index of refraction) at the base of the craze.[9] The experimental data are the asterisks while the calculated data are the different lines. The horizontal axis represents the distance (x) normalized by the craze length s; the craze lies between $x/s= 0$ and $x/s= 1$. The crack tip is located at zero and the crack extends over $x/s\leq 0$. Except for the line corresponding to the Dugdale model it is difficult to distinguish among the displacements represented by the stress distribution with different numbers of segments.

In the bottom diagram of figure 10 the deviation between the experimental and calculated displacements is plotted against distance. In this case the deviation is normalized by $0.25\ \lambda$ which is the difference in height of the displacement between consecutive extrema. As the number of segments increases the deviation decreases with no discernible or obvious criterion for choosing an optimum number of segments.

The stress distribution along the craze for the same data used above is plotted in figure 11. The abscissa shows the distance normalized by the craze length with x/s= 0 corresponding to the base of the craze (crack tip) and x/s= 1 corresponding to the craze tip. The ordinate represents the craze stress in MPa. As one passes from the Dugdale model (horizontal dashed line) to a distribution with 2 segments (bi-linear), the stress distributions are very different; however, as the number of segments increases further the stress distribution does not change much. In particular, the distribution for 4 and 6 segments is about the same to within the error bars.[10] As the number of segments is further increased the noise in the experimental data introduces numerical instabilities which cause oscillations in the stress distribution as the plot for 8 segments shows.

---

[8]We use the term COD to denote the craze and crack opening displacement to avoid confusion between $2v(x)$ which is the opening displacement and $2w(x)$ which denotes the position of the elastic-plastic boundary. Thus, we have $\text{COD}=2v(x)=2w(x)-\tau(x)$.

[9]The primordial thickness at the base of the craze $\tau_{CI}(0)=0.435$ μm is a convenient number for non-dimensionalizing the COD. The non-dimensional COD at the crack tip gives the average extension ratio of the craze.

[10]The error bars are determined together with the stresses by the singular value decomposition LSF.

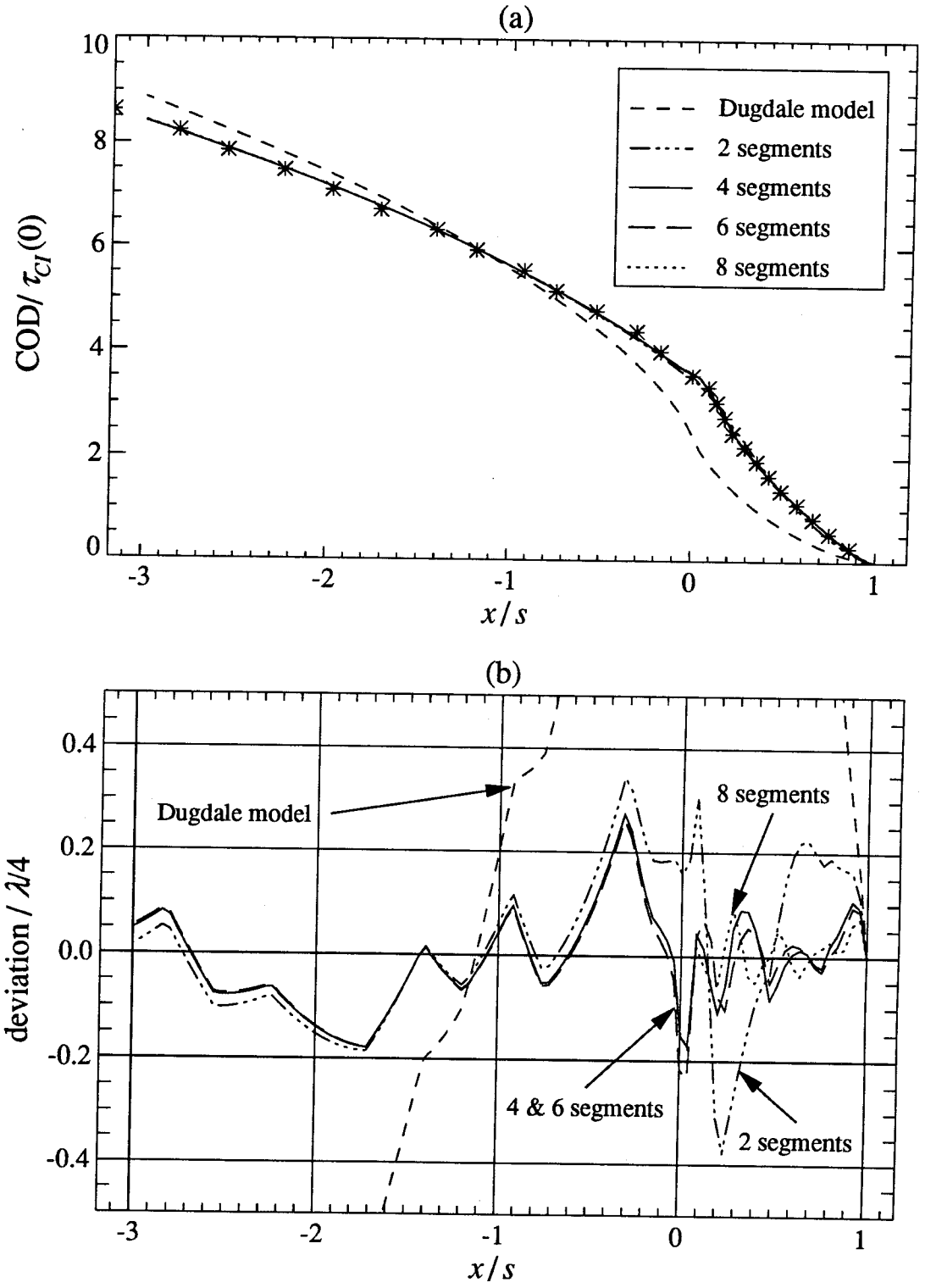

FIGURE 10 Profiles and deviations for different number of segments in the craze stress distribution as the craze is unloaded to $K_I = 0.339$ Mpa $m^{1/2}$.

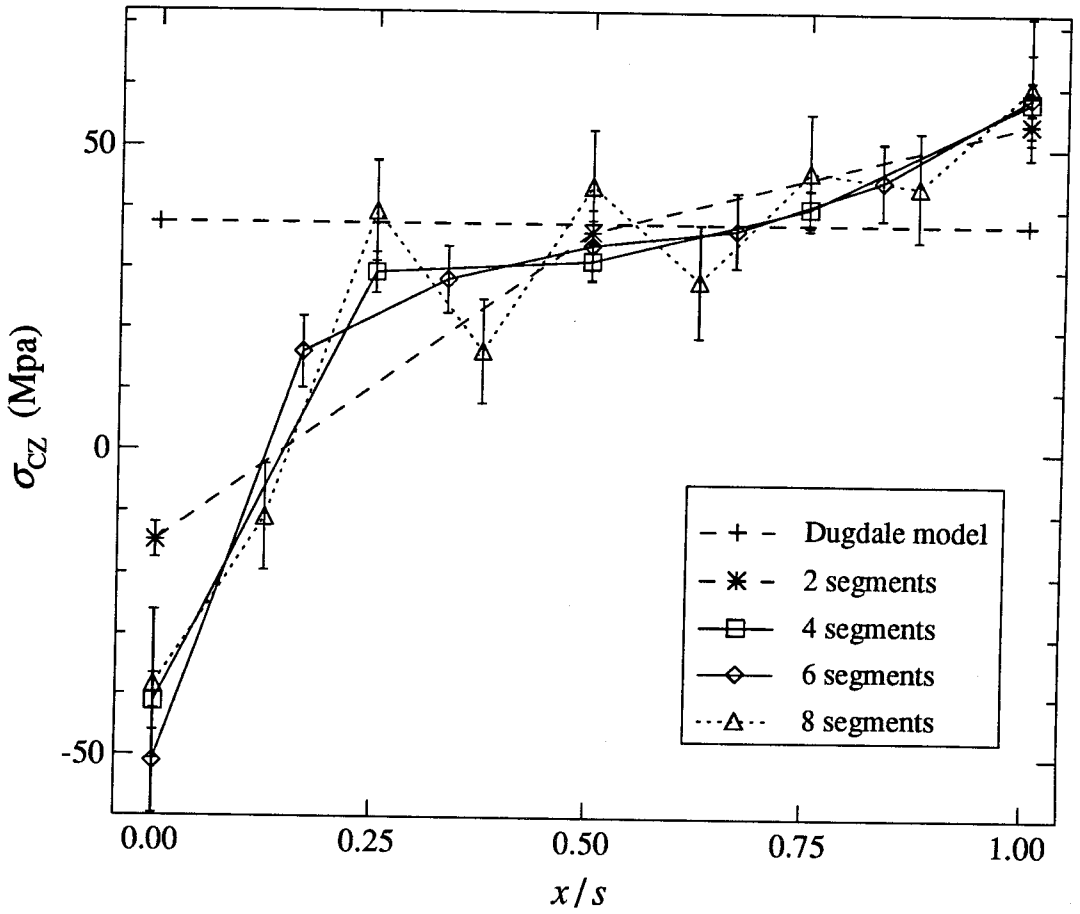

FIGURE 11 Stress distributions along the craze for different number of linear segments as the craze is unloaded to $K_I = 0.339$ Mpa $m^{1/2}$.

For this particular example the distribution finally chosen corresponds to 6 segments. Finding the optimum number of segments involves subjective criteria as there are always some distributions which seem to give equally good results. For most of the cases that were analyzed we found that either 3 or 4 segments yields a reasonable stress distribution commiserate with the precision of the measurements.

This section finishes the discussion on constructing the craze/crack opening displacement and the associated stress distribution so that the calculated displacements match the experimental profiles. We now turn our attention to discussing some of the results.

5. Results and Discussion

This section examines some of the profiles and craze stress distributions obtained in compact tension specimens of PMMA (commercial grade Rohm & Hass). The thickness of the specimens used was 2.85 mm. The in-plane dimensions are described in chapter 1 Before evaluating craze behavior under fatigue loading, craze response derived from step wise loading and unloading will be considered.

5.1 Quasi-Static Results

For this set of experiments opening profiles were obtained after a fatigue experiment was run. During the experiments the crack propagated by more than 1 mm at a test frequency of 2 Hz. After the experiment was completed the specimen remained loaded at the minimum stress intensity factor used during the fatigue test for approximately 10 minutes before it was manually (quasi-statically) loaded to various stress intensity factors at which the profiles were recorded.

Two loading sequences are described here: In the first, two fringe patterns of the opening displacements were recorded during loading and two during unloading. The loading cycle lasted approximately 2-4 minutes. The maximum stress intensity factor during the manual loading cycle was below the maximum stress intensity factor achieved during the fatigue test sequence.

The second loading sequence was recorded after a new and additional fatigue experiment had been run. The specimen was loaded to a stress intensity factor larger than that used in fatigue test. The loading cycle lasted approximately 1-2 minutes. Four fringe patterns of the opening displacements were recorded during the unloading part of the cycle.

5.1.1 Primordial Thickness

As discussed in the previous section, before one can proceed to determine the net opening displacement (and the stresses) one must define the primordial thickness; this is accomplished by assuming that the index of refraction is constant throughout the craze and using equation 12.

Equation 12 is a cubic equation for the index of refraction in terms of the ratio of extrema in the craze m_C to the number of extrema in the unloaded craze m_0. The number of extrema in the unloaded craze was determined from six different unloaded profiles in four different specimens. In all but one case m_0 turned out to be 5 (in the one particular exception the third bright craze fringe appeared to be merging with the first bright fringe of the crack).

Once the index of refraction is known, one can determine the extension ratio Λ, the primordial thickness τ and the craze/crack opening displacements COD. It is convenient to present the results of the primordial thicknesses (as well as the COD's) in non-dimensional form. Using $m_0 = 5$ (and $\Lambda = 1.46$ for the unloaded craze) the primordial thickness at the base of the craze (crack tip) is found to be

$$\tau_{CI}(0) = 0.44\ \mu m. \qquad (*)$$

Both the primordial thickness and the opening displacements are normalized by this quantity.

The primordial thickness for each load level in the loading-unloading sequence is shown in figure 12. Three of the four primordial thicknesses are very close together: namely, the first loading one and the two unloading ones. These primordial thicknesses (determined under the assumption of a constant index of refraction) serve to define the (unique) primordial thickness for the sequence which is shown as the dashed line.

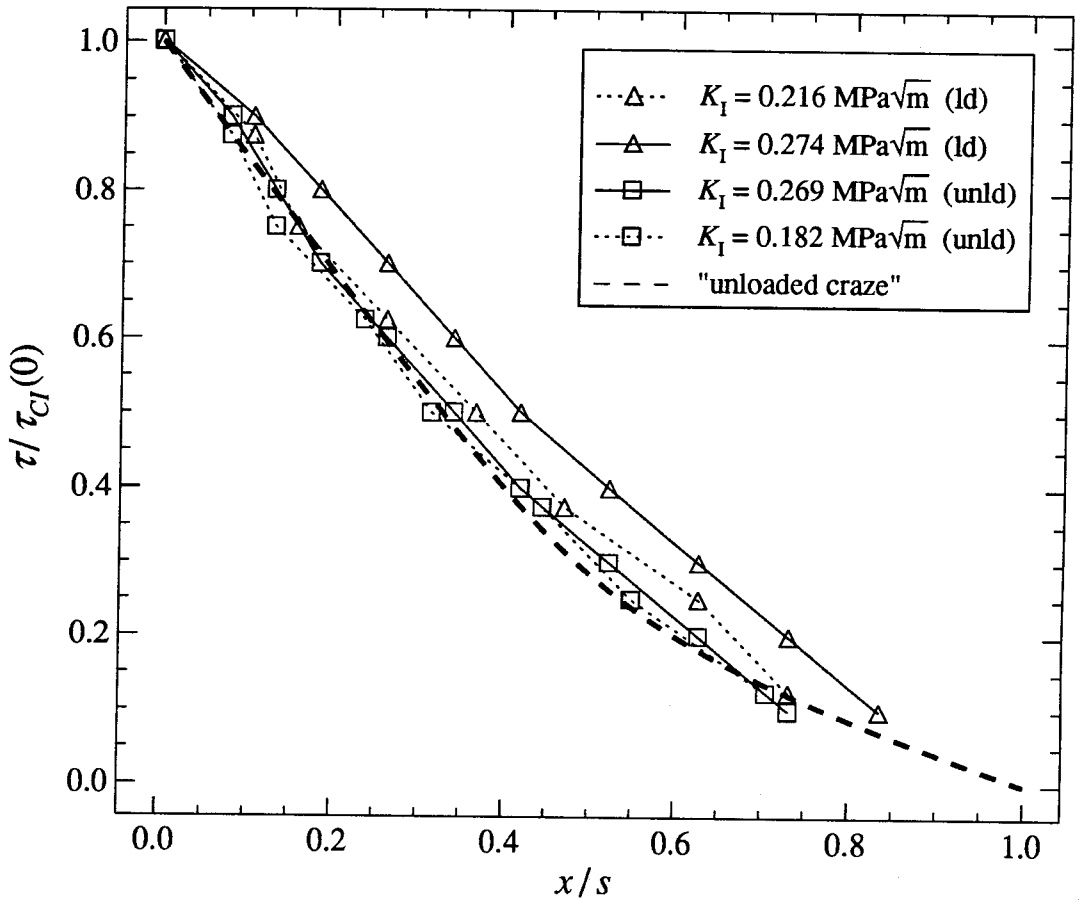

FIGURE 12 Primordial thicknesses using a constant index of refraction for a static loading and unloading case.

For computational purposes the primordial thickness was defined in terms of a hyperbola. It passes through the points (1,0) and (0,1) and the other parameters are varied until a good fit is found to the primordial thicknesses for a constant index of refraction. The emphasis is placed on matching the ones at lower stress intensity factors since it is expected that at lower stress intensity factors the index of refraction will be constant.

The primordial thickness for the unloading sequence are shown in figure 13. In this case the four primordial thicknesses for a constant index of refraction are very close to each other and the primordial thickness for the whole sequence is readily defined; it is shown as the dashed line. Once the primordial thickness for a sequence has been defined

one can proceed to construct the opening displacement profiles and calculate the extension ratios.

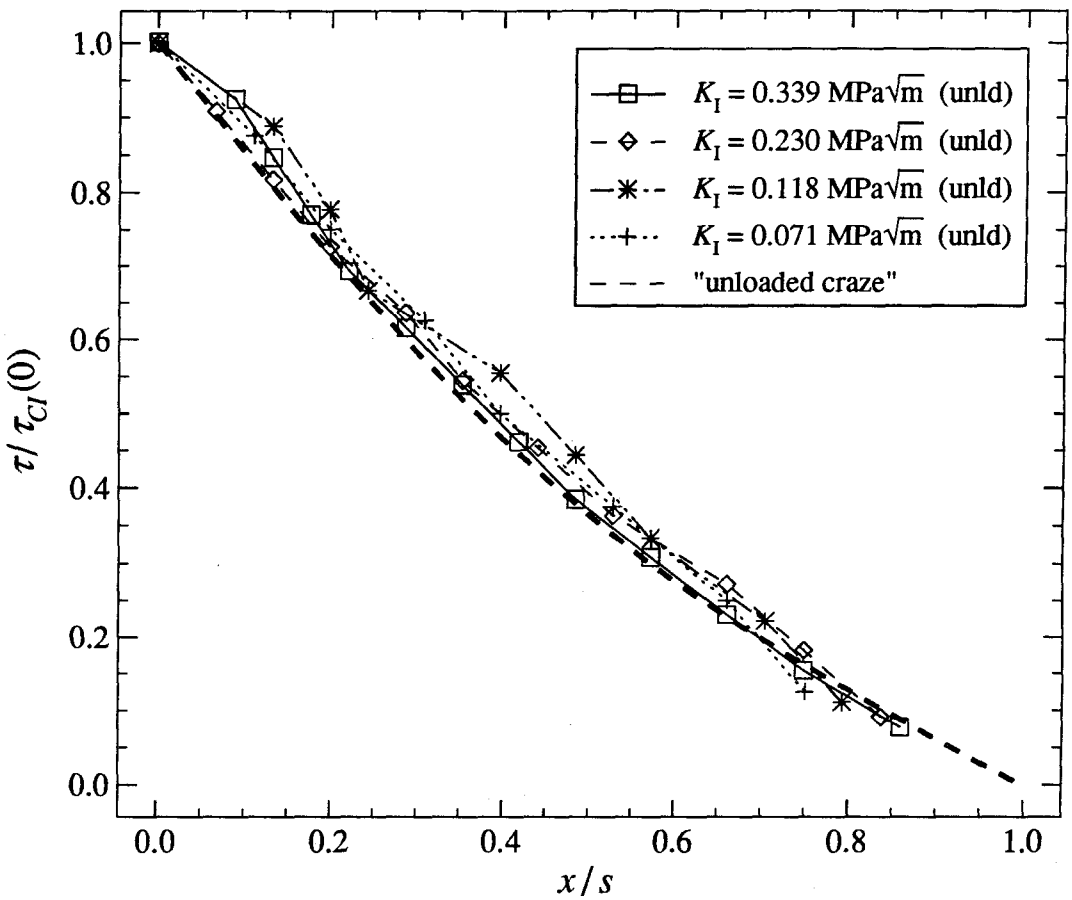

FIGURE 13 Primordial thicknesses using a constant index of refraction for a static unloading case.

5.1.2 Opening Profiles and Extension Ratios

The opening profiles for the loading-unloading sequence are shown in fig 14a. The COD is plotted on the vertical axis and normalized by the maximum primordial thickness at constant index of refraction; the abscissa shows the position normalized by the craze length s. The craze corresponds to $0< x/s \leq 1$ while the crack corresponds to $x/s \leq 0$. The calculated opening displacements are shown by dotted and solid lines while the experimental values which are displayed by the triangles (loading) and squares

(unloading). There is a good fit between the experimental and calculated displacements. The opening displacement in the craze tends to be concave for the unloading profiles (squares; specially for K_I= 0.269 MPa $m^{1/2}$) and they tend to be "straight" for the loading profiles.

Figure 14b shows the extension ratios along the craze. The extension ratios for the unloading profiles (squares) tend to be constant since the primordial thickness was chosen to match those of the unloading profiles. All extension ratios show a drop as the craze tip is approached; however, the data closest to the craze tip may be unreliable since the location of the craze tip could not be determined experimentally but had to be inferred by extrapolation. The location of the craze tip was extrapolated from the fringe patterns and a plot of the primordial thicknesses against the crack-parallel coordinate.

Figure 15 shows the corresponding opening displacements and extension ratios for the unloading sequence. In this case the fit between the calculated opening displacements (lines in figure 15a) and the experimental ones (symbol) is even better than for the loading case. The opening displacement in the craze tends to be concave for all of the profiles.

The corresponding extension ratios are shown in figure 15b. They are almost constant since all of the primordial thicknesses at constant index of refraction were very close to each other and to the chosen primordial thickness. The drop in extension ratio as the craze tip is approached is also present, as it was in the loading-unloading sequence.

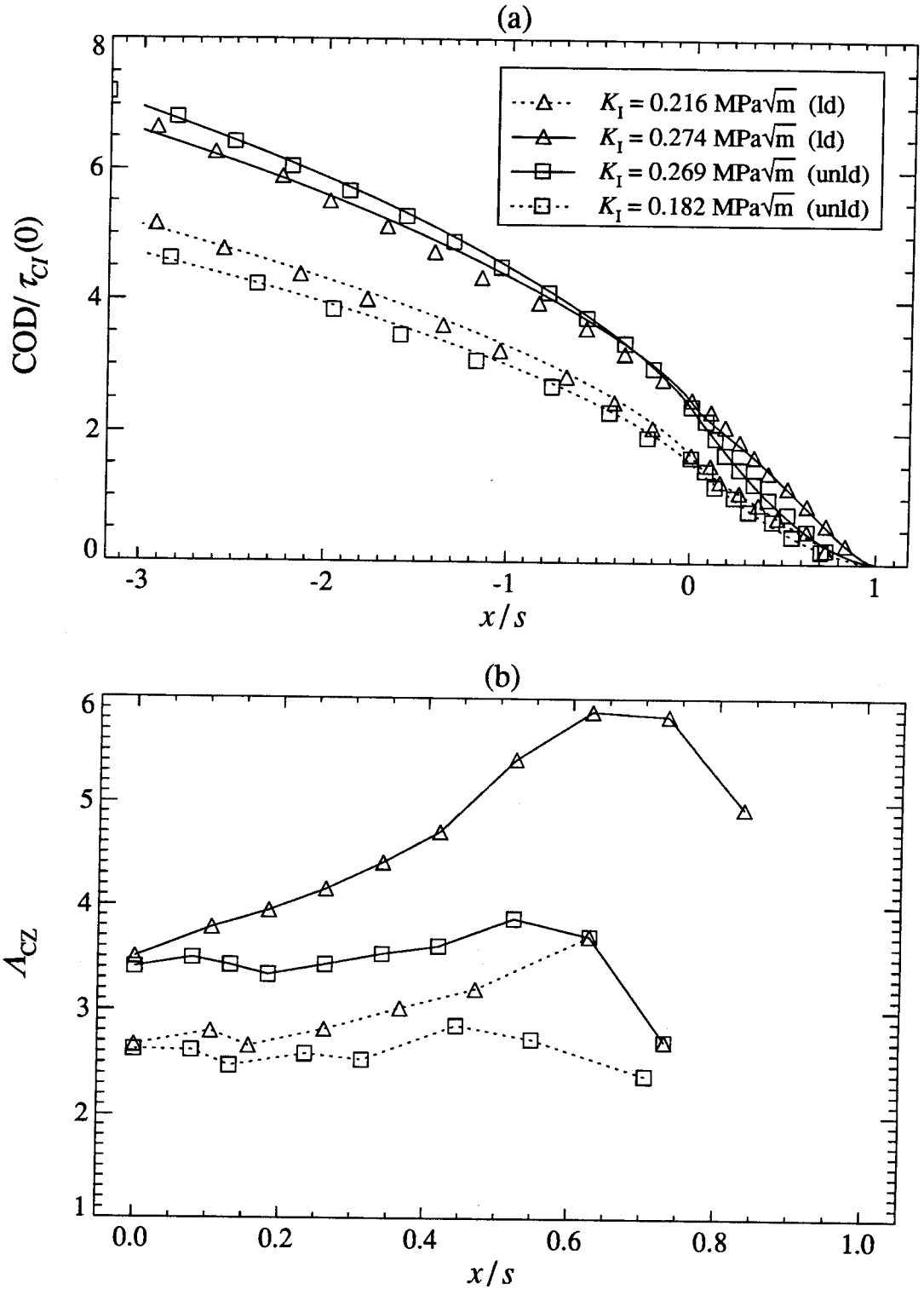

FIGURE 14 Profiles and extension ratios for a static loading and unloading case.

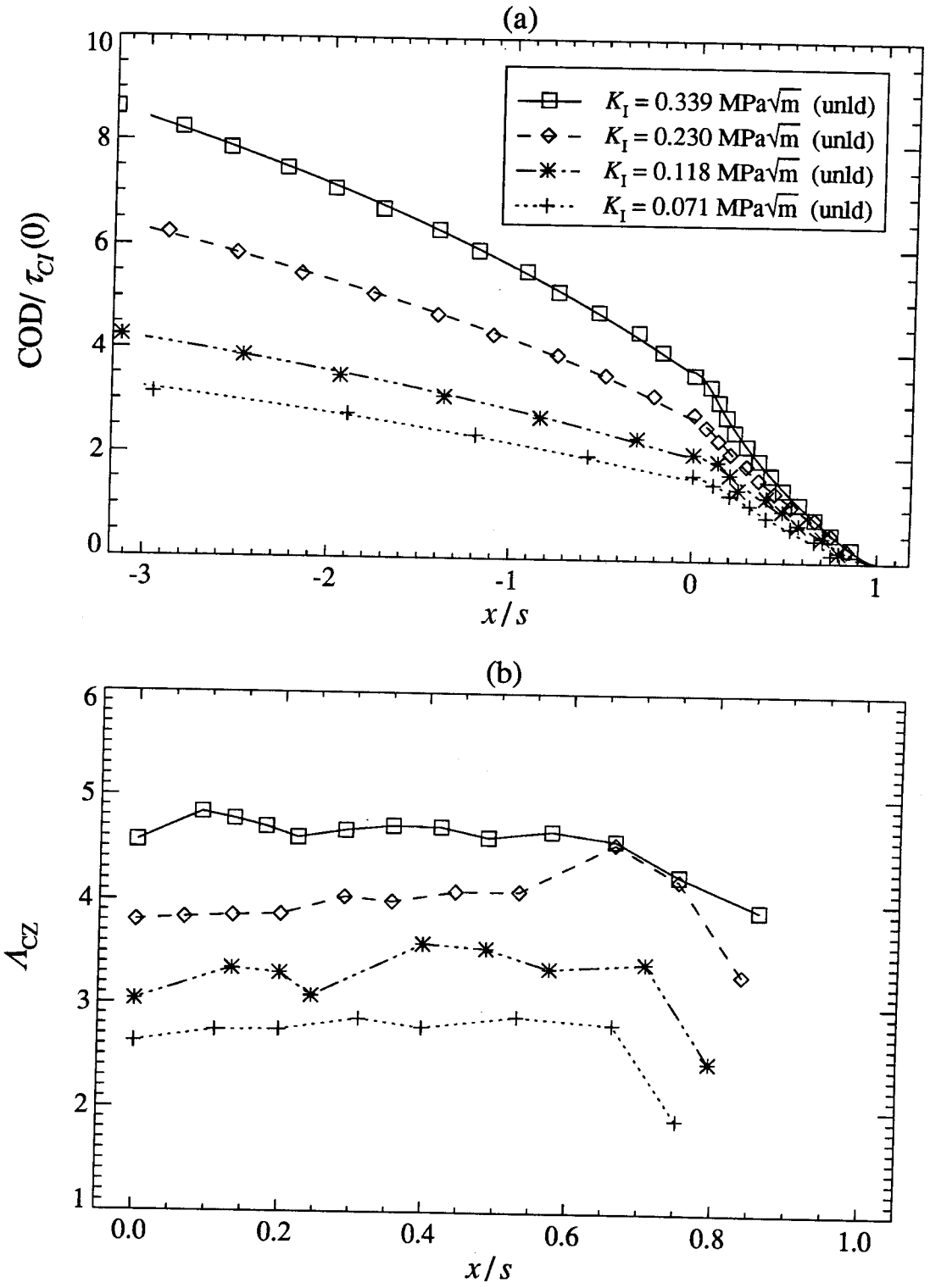

FIGURE 15 Profiles and extension ratios for a static unloading case.

5.1.3 Stresses

The stresses along the craze were found by finding the best fit to the experimentally-determined opening displacements. The stress distributions for the loading-unloading sequence are shown in figure 16 while the distributions for the unloading sequence are shown in figure 17. In each figure the craze stresses are plotted along the ordinate against distance along the craze with $x/s = 0$ corresponding to the base of the craze (crack tip) and $x/s = 1$ corresponding to the craze tip. The round dot on the open triangle indicates the load level in terms of the stress intensity factor during the sequence when the fringe pattern was acquired.

The stress distributions in figure 16a and 16b correspond to the opening profiles during loading. The shape of the distribution tends to be concave. A stress distribution similar to these-i.e., smaller stresses in the lower half of the craze that rise linearly from the middle of the craze toward the craze tip- were also found by Brown and Wang [30] in Polyethylene crazes. This type of stress distribution (concave) gives rise to openings which are somewhat "straight" due to the lower stresses in the middle of the craze.

The stress distribution during unloading (figures 16c and 16d) tend to be convex and the smaller stresses near the base of the craze give rise to the more typical (in terms of the Dugdale model) concave craze opening displacements. The smaller error bars of the stresses in figure 15c reflect the better fit between the experimental and calculated displacements of the unloading profile at $K_I = 0.269$ MPa $m^{1/2}$ in figure 14a.

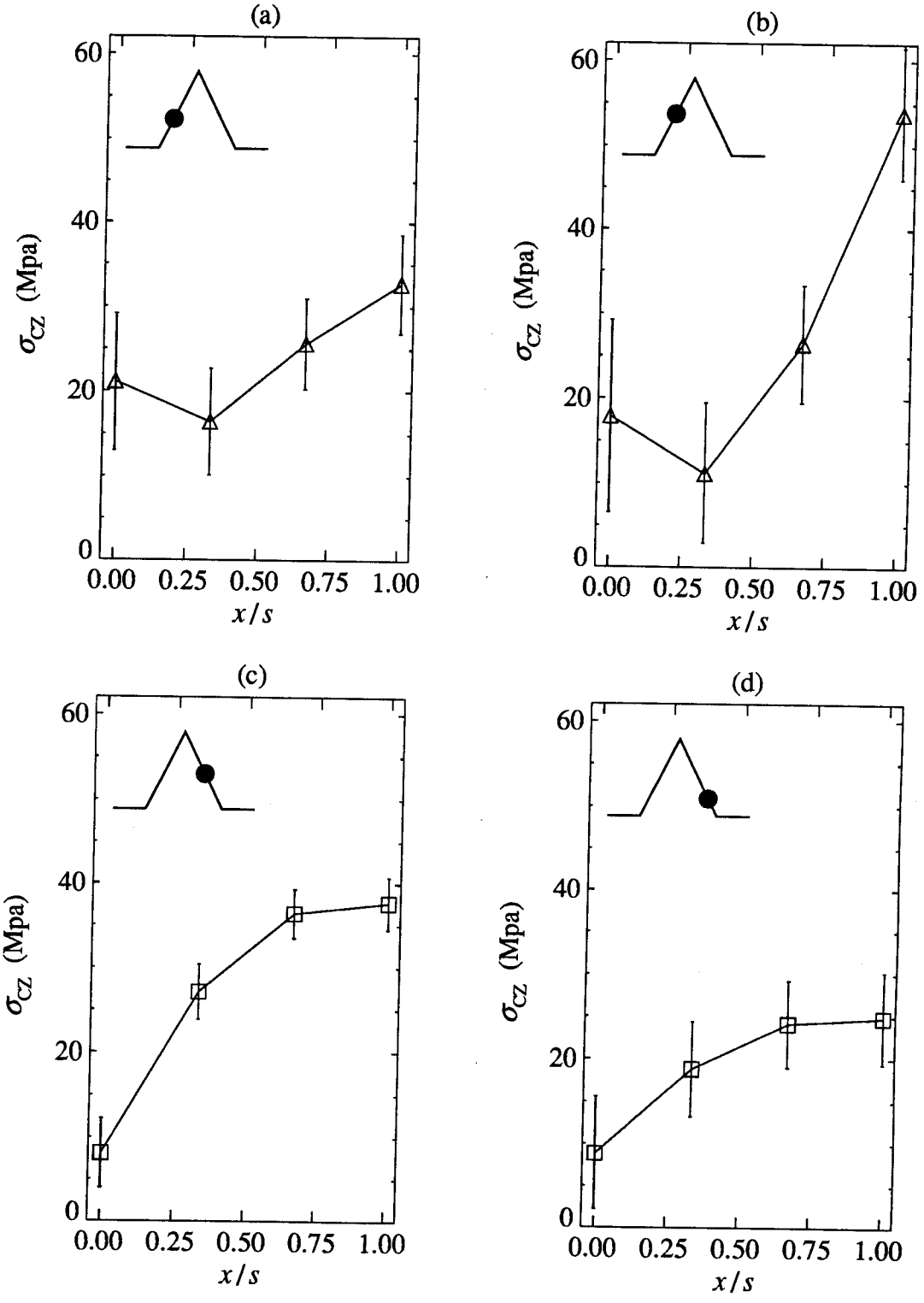

FIGURE 16 Stress distribution along the craze for a static loading and unloading case.

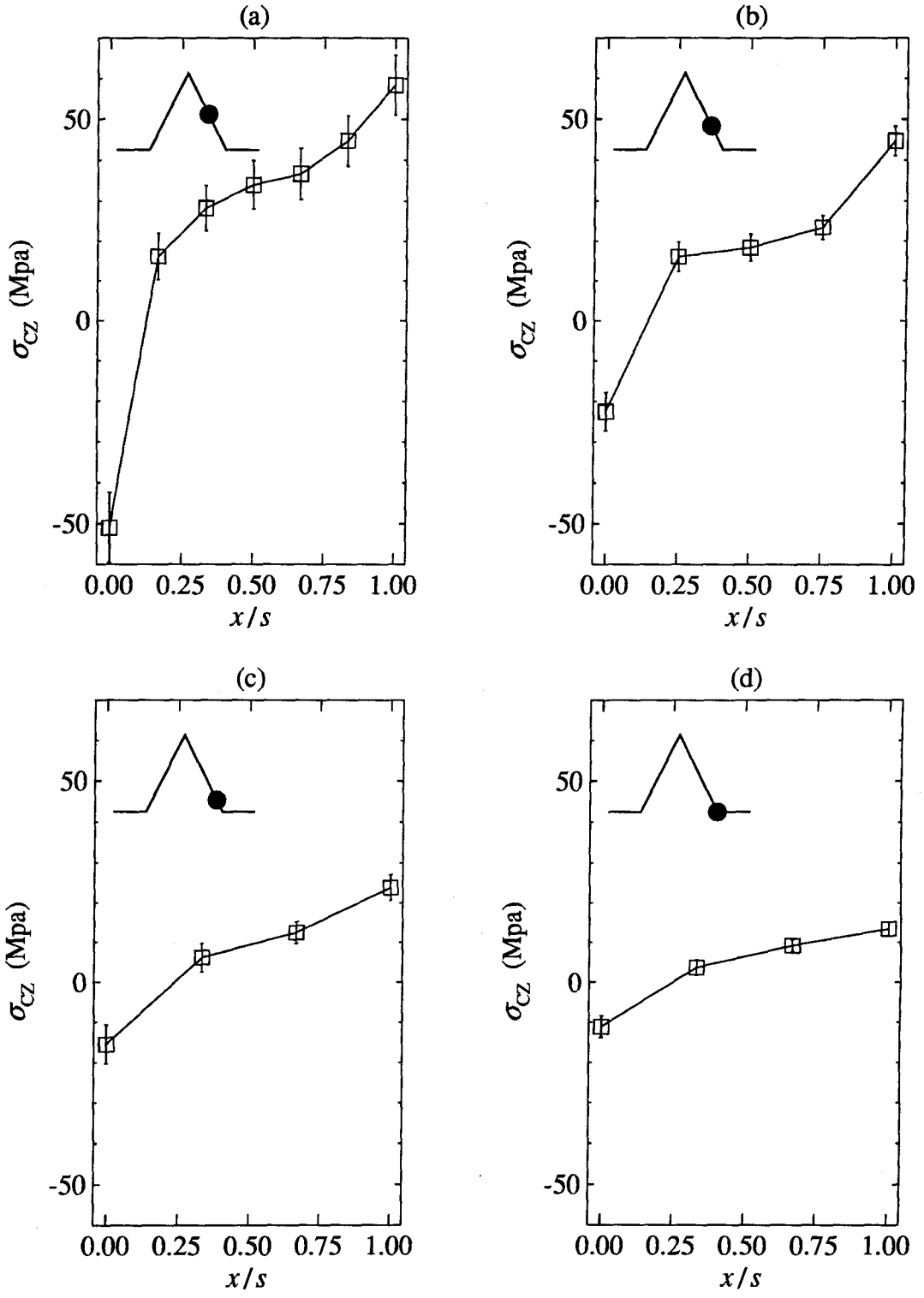

FIGURE 17 Stress distribution along the craze for a static unloading case.

The stress distributions for the unloading sequence (figure 17) share some similarities to the previous unloading distributions (figures 16c and 16d); in particular, the stress distribution in figure 17d looks like the other distributions. The main difference in this (unloading) sequence is that they were obtained after the specimen was loaded to a much higher stress intensity factor (0.64 MPa $m^{1/2}$ vs. 0.40 MPa $m^{1/2}$). In particular, the stress intensity factor was larger than that used during the fatigue test which formed the craze.

The main consequence of the overload is that upon unloading, part of the craze may come under compressive stresses (crack closure). These compressive stresses are generated as one starts unloading and become less negative as the unloading continues.

This situation can be compared to the plasticity-induced crack closure that occurs after an overload [31]. The excursion into the overload (50% higher stresesses than those that genarated the craze) enlarges the (thickness) of the material inside the craze so that upon unloading the craze no longer "fits" and acts as an embedded wedge, thereby generating the compressive stresses. It should be noted that the closeness in the fit between the calculated and measured displacements provide a good indication that the (stress) model is able to deal with the stresses generated during crack closure.[11]

The error bars on the unloading sequence of stress distribution are smaller than those in the loading-unloading sequence. The smaller error bars in these stress distributions reflect a better fit between the calculated and measured opening displacements.

---

[11]No assumptions were made on the sign of the stresses during the derivation of the stress-displacement equation in section 4.

5.1.4 Stress-Displacement Relations and Stress-Extension-ratio Plots

One way to characterize the behavior of the craze is to plot the stress distribution along the craze as a function of the craze opening displacement. This type of load-displacement diagram can serve as a starting point in modeling the craze lifetime or as a boundary condition for numerical studies on the mechanics of crack and craze growth [27].

The stress-displacement relation for the loading-unloading sequence is shown in figure 18. The tip of the craze (COD= 0) experiences the higher stresses; the stresses drop toward the middle of the craze and at the base of the craze (largest CODs) some reloading may occur. As the craze is loaded the stress-displacement relation moves outward from the origin and returns toward the origin as the craze is unloaded. The hatched area is meant to indicate broadly a representative stress-displacement relation for the particular craze state.[12]

[12]In terms of a supra-molecular modeling the craze is the process zone where at the tip of it bulk material is converted into fibrils and where damage accumulates during the fatigue loading before final fracture occurs at the base of the craze. Calculating the stresses and opening displacements of a craze after a fatigue experiment can be thought of as "probing" the state (of damage) of the craze. The stress-displacement relation is a measure of that state.

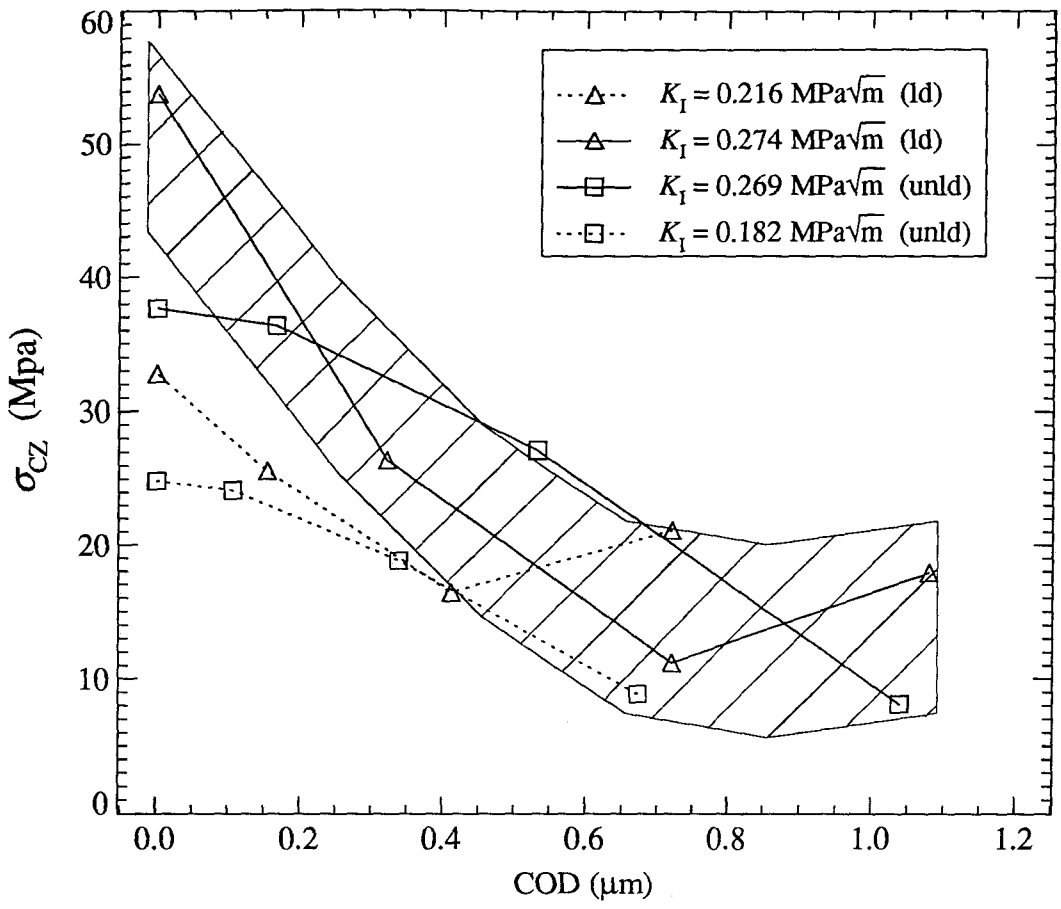

FIGURE 18 Stress-displacement relation for a static loading and unloading case.

The stress-displacement relation for the unloading sequence is shown in figure 19. The compressive part of the stress-displacement relation reduces the opening displacement such that the slope of the stress-displacement relation at the highest displacements becomes less negative as the craze is unloaded (in the loading-unloading sequence, figure 18, the slope does not change as the craze is unloaded).

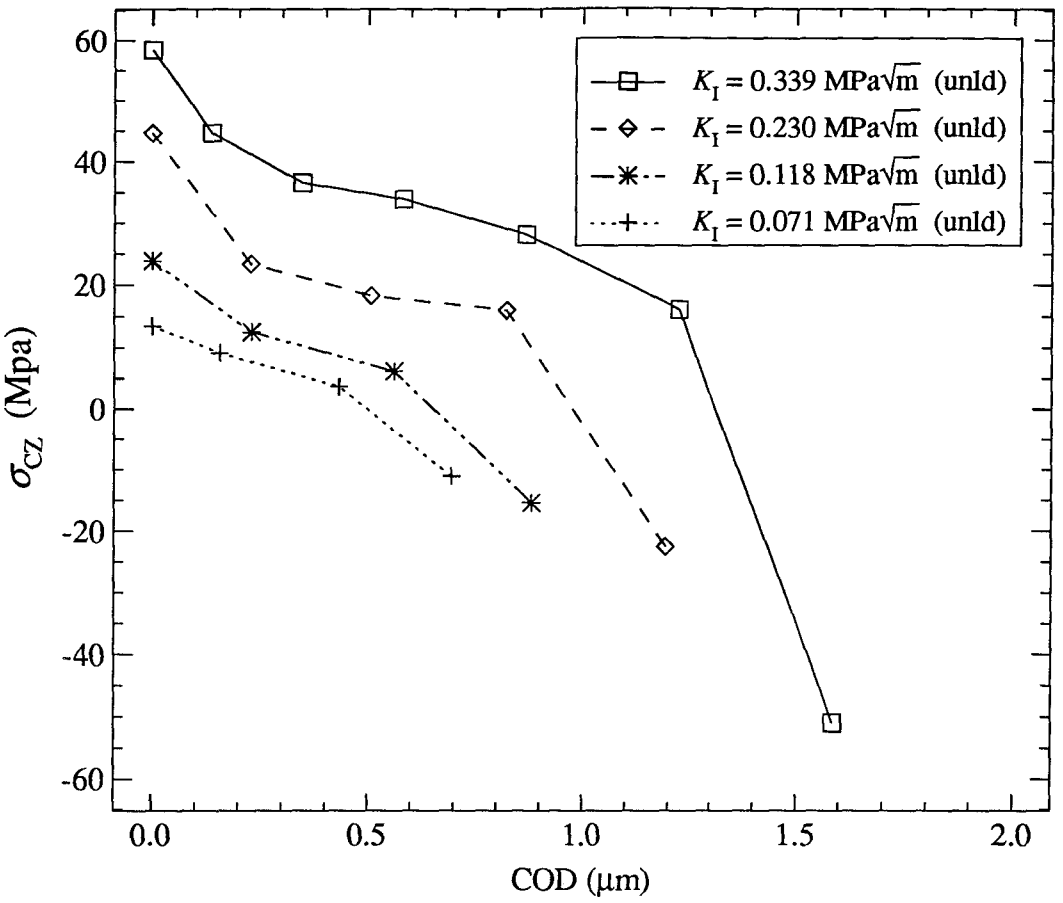

FIGURE 19 Stress-displacement relation for a static unloading case.

The stress vs. extension ratio is plotted in figure 20 for the loading-unloading sequence. The triangles represent the loading points while the squares represent the unloading ones. The different lines correspond to different locations along the craze. Starting from the base of the craze the first two loading-unloading paths (x/s= 0 and x/s= 1/8) are traversed clockwise while the next four are traversed counter-clockwise. The reason behind the reversal is that the stresses in the middle of the craze are higher upon unloading than they were during loading. Although there is no extension ratio data to plot the paths close to the tip of the craze, it can be argued that the loading-unloading paths would be traversed in a clockwise fashion.

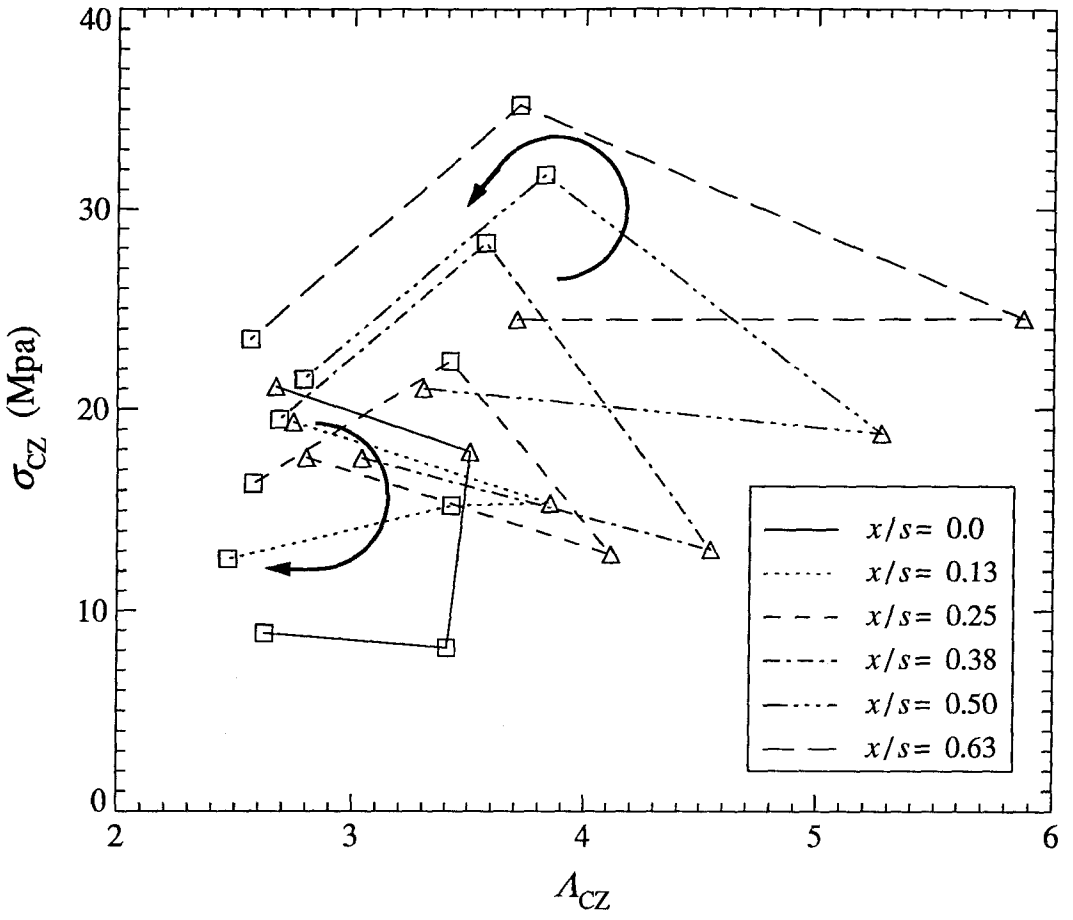

FIGURE 20 Stress vs. extension ratio for a static loading and unloading case.

The implication of the direction in which a path is traversed is that while the elastic body does work on the base and the tip of the craze the middle part of it does work on the surrounding elastic body.

The stress vs. extension ratio is plotted in figure 21 for the unloading sequence. The unloading path is shown at seven different locations along the craze, starting at $x/s= 0$ and ending at $x/s= 3/4$. The paths with compressive stresses are confined to a region next to the crack tip that is a quarter of the length of the craze.

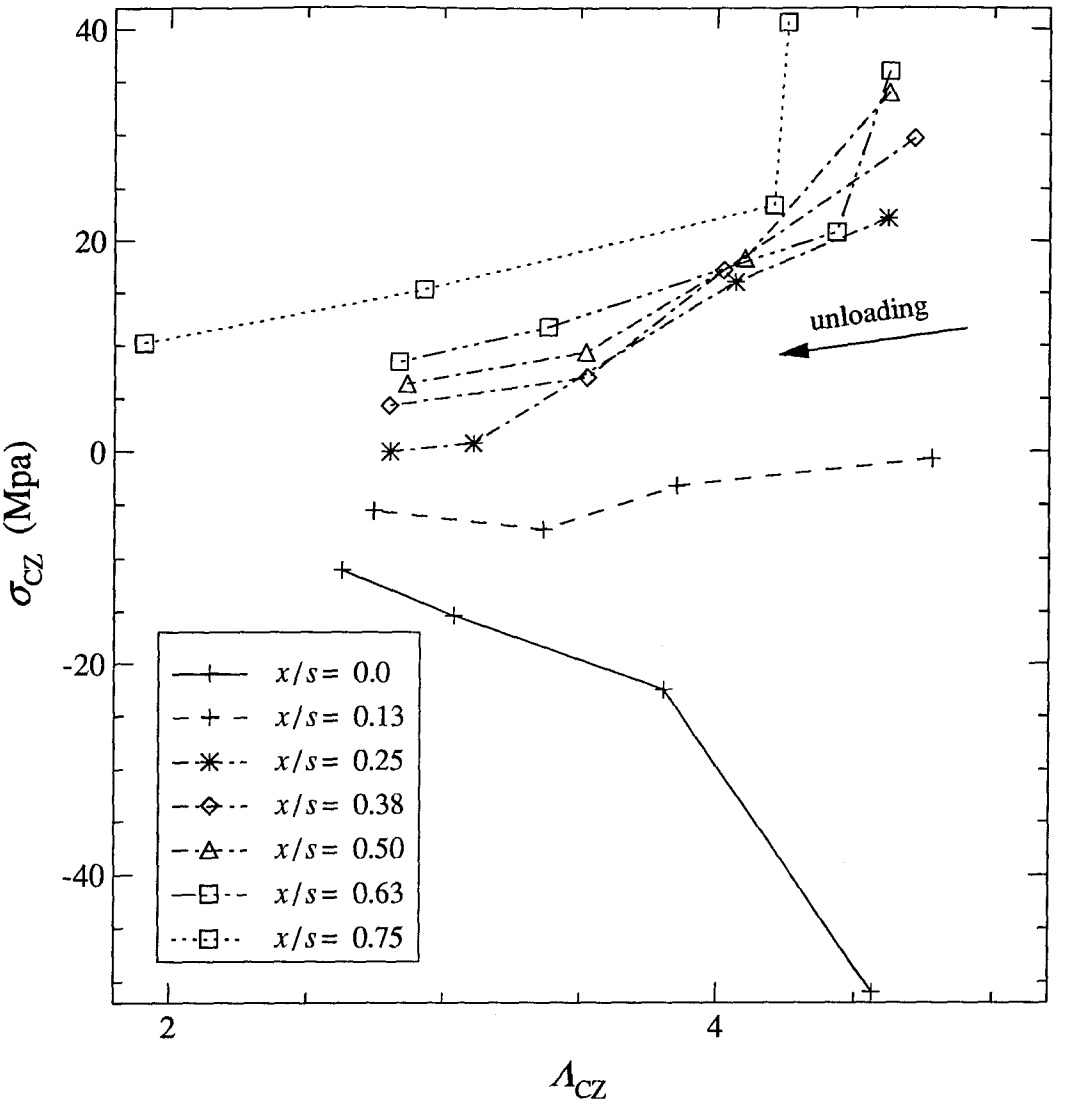

FIGURE 21 Stress vs. extension ratio for a static unloading case.

5.2 Results from Fatigue Loading

This section concerns the results obtained during fatigue experiments. The frequency employed was 0.1 Hz. Prior to running the experiment where the data was recorded, another experiment was run at a frequency of 1 Hz where the loading was adjusted so as to produce a constant stress intensity factor and the crack was allowed to propagate by more than a millimeter. The 0.1 Hz data to be discussed was taken after the

experiment ran for several hundred cycles and the crack and craze had propagated by more than the length of the craze.

Eleven fringe patterns were collected during a cycle. They are collected at equally spaced intervals (36° apart) during the cycle; the first one is collected when the load is a minimum, the sixth one when the load is a maximum and the eleventh one at the minimum load one cycle later. Where appropriate, the data is labeled 0.0, 0.1, etc., up to 1.0, with 0.0 and 1.0 corresponding to the minimum load while 0.5 corresponds to the maximum one. The loading curves are labeled with triangles; the curve corresponding to the maximum (0.5) is labeled with asterisks and the unloading ones with squares. The area where the data is collected is approximately 0.25 mm away from the free surface (the thickness of the specimen was 2.85 mm). We examine first the primordial thickness obtained during a fatigue cycle.

5.2.1 Primordial Thickness

The primordial thicknesses determined under the assumption of a constant index of refraction during a fatigue cycle are shown in figure 22a. The primordial thicknesses tend to be straight lines of various (constant) slopes. The most striking difference between these primordial thicknesses and those obtained under step loading after a fatigue experiment is the spread among them. None of the primordial thicknesses are grouped together except for those at 0.0 and 1.0. This spread brings up a fundamental issue: How does one define a (single) primordial thickness for this (or any other) cycle?

Figure 22b shows four of the eleven profiles together with some of the possible models that define the primordial thickness. Könczöl et al. [21] chose the minimum load sufficiently small as to allow the assumption that the index of refraction was constant and equal that of the unloaded craze. In the present case the profile at the minimum load has

the same number of extrema (e.g., 5) as the "unloaded[13]" craze so that it would be reasonable to use that particular primordial thickness as the (single) primordial thickness for the cycle. Such a model is shown in figure 22b and labeled 'B_hyperbola.'[14] The use of that primordial thickness presented a difficult problem: It was not possible to find a craze stress distribution that could produce displacements which matched the measurements.

In addition, an attempt was made to define the primordial thickness based on some of those associated with unloading. The model labeled 'U_hyperbola' tries to match the primordial thicknesses at 0.8 and 0.9; however, the use of that model lead to the same difficulties. A third model, based on the Dugdale stress distribution and labeled 'Dugdale', produced a marginally better match between the displacements.

Because all of the primordial thicknesses look like straight lines, it was decided to try a primordial thickness that varied linearly with x/s. The primordial thickness labeled 'linear' in figure 22b leads these to displacements that can be modeled reasonably well by the N-segment craze stress distribution. The use of this model brings out a different problem: The primordial thickness in the middle of the craze turns out to be larger than the calculated craze thickness ($2w(x)$) for the profiles at the lower loads. This situation produces physically unallowable indices of refraction and extension ratios.

---

[13]By "unloaded" craze we have meant a craze at the front of the crack in a specimen under no external load. From the discusion concerning the stresses in section 5.1.3 one can argue that it is possible to have a loaded craze (with a self-equilibrating stress field) in an unloaded specimen.

[14]The original model had the primordial thickness equal to zero at the craze tip; however, that model produced extension ratios near the craze tip that were unusually high (> 40).

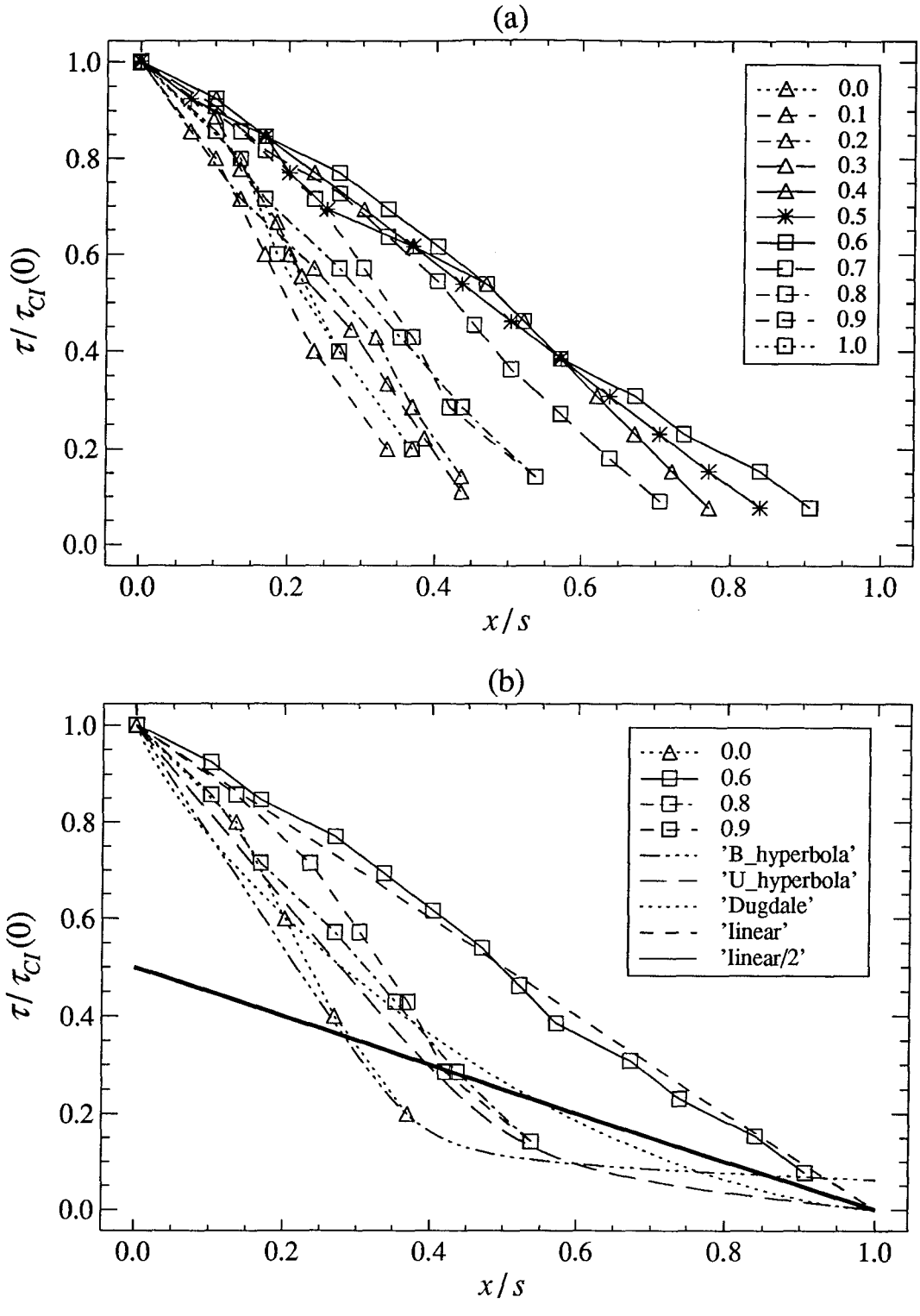

FIGURE 22 Primordial thicknesses using a constant index of refraction for a fatigue case.

Based on the linear primordial thickness estimate, we solve the problem mentioned above by reducing its size. The primordial thickness that was used to construct the profiles and calculate the stresses is shown as the solid line and it is labeled 'linear/2'.

One of the consequences of considering different primordial thicknesses is that we must forgo the discussion about the extension ratios since they depend critically on the primordial thickness. Any slight change in the primordial thickness produces a large change in the extension ratios since the primordial thickness is the reference length used in calculating them (i.e., the extension ratios are inversely proportional to the primordial thickness). However, the stresses and displacements are not as drastically affected as the extension ratios were.

5.2.2 Opening Profiles

A sample of the opening displacements for the fatigue cycle are shown in figure 23. While the fit between the measured and calculated displacements is not as good as it was for the profiles obtained under slow step loading, it is within $\lambda/8$. Some of the calculated displacements (e.g. that at the minimum load) are slightly negative near the craze tip; however, their magnitude is within the noise (or error) in the measured displacements.[15]

5.2.3 Stresses

The stresses derived from the LSF between the measured and calculated opening displacements are shown in figures 24 and 25. The vertical axis denotes the craze stresses in MPa while the horizontal axis denotes the position along the craze. The base of the craze (crack tip) is at $x/s = 0$ and the craze tip is at $x/s = 1$. The small black circle on the sinusoid represents the position on the loading cycle when the data was acquired.

---

[15]If we consider the noise or error in x-direction to be 1 pixel then the error in the COD is about $\lambda/10$, or about 0.15 units of the vertical axis in figure 23.

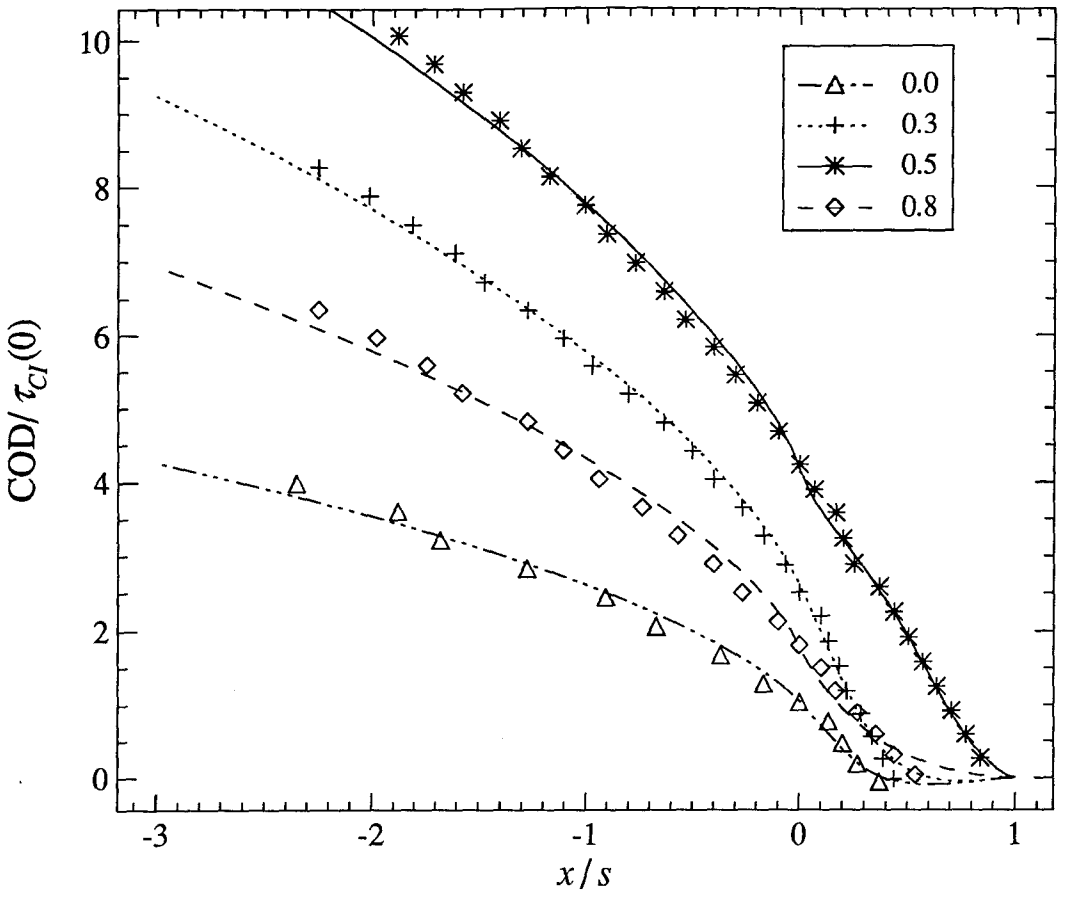

FIGURE 23 Opening profiles for a fatigue case.

Figure 24 shows the stress distributions during the loading part of the cycle with figure 24a showing the craze stresses at the minimum load while 24f shows the craze stresses at the maximum load. The first four load distributions are similar. A transition in the distribution of the stresses occurs in figure 24e and the stress distribution at the top of the cycle (figure 24f) shows a drop in the stresses at the middle of the craze. The change in the stress distribution as well as the distribution at the maximum load provides information on the damage in the craze as discussed further in section 5.2.6.

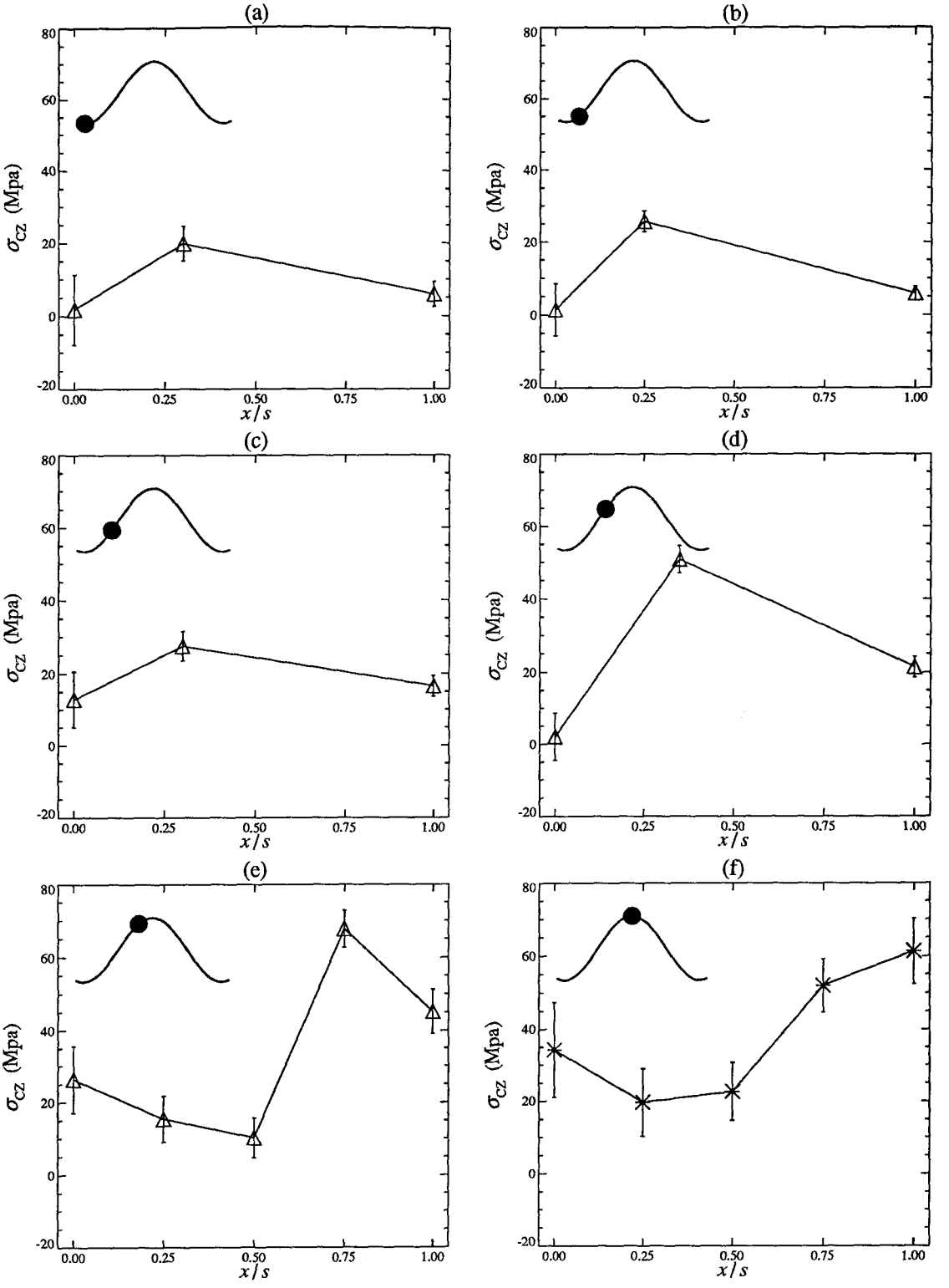

FIGURE 24 Stress distribution along the craze during the loading section of a fatigue cycle.

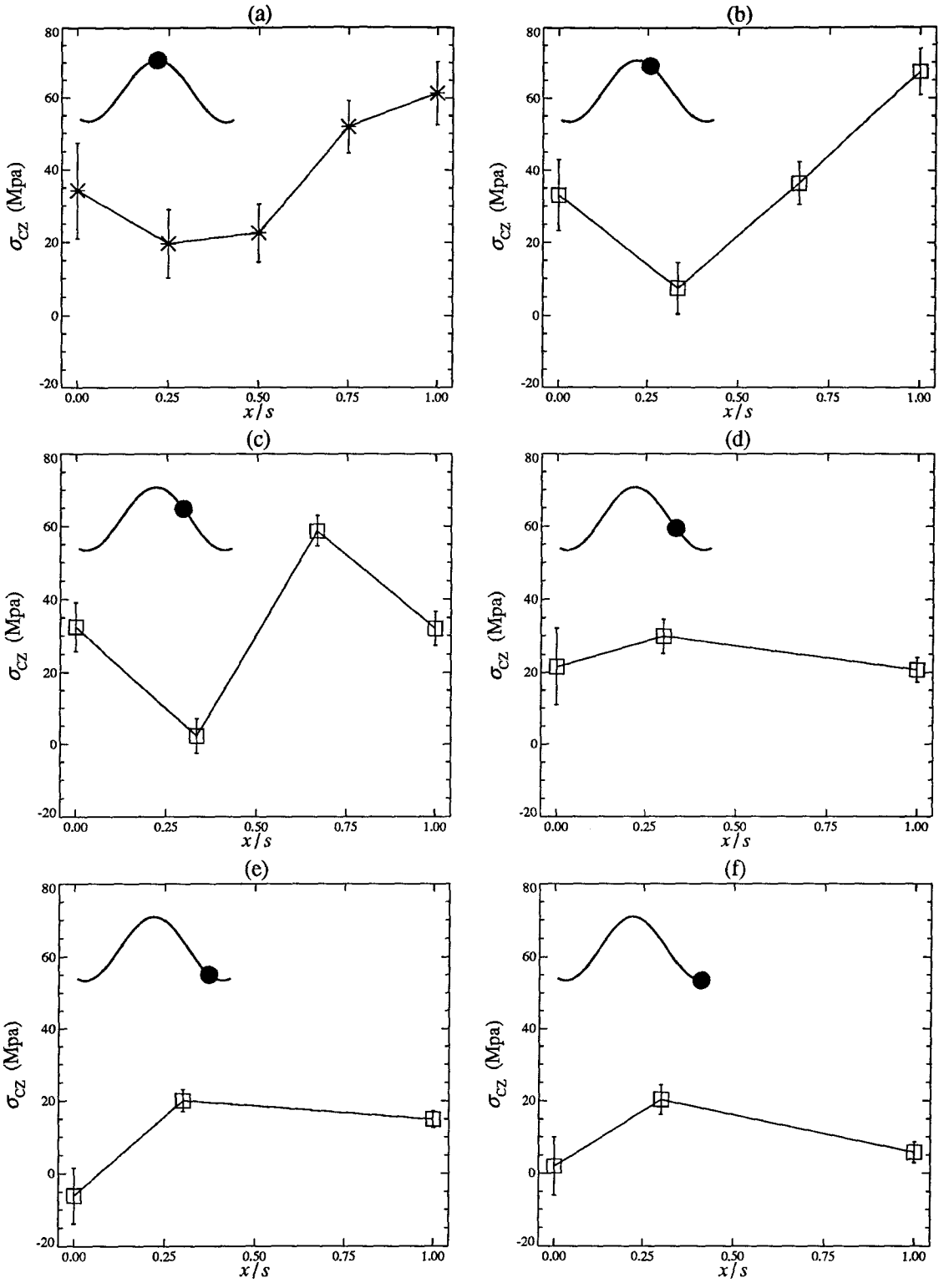

FIGURE 25 Stress distribution along the craze during the unloading section of a fatigue cycle.

Figure 25 shows the stress distributions during the unloading part of the cycle. The distribution at the maximum load (figure 24f) is repeated in figure 25a. Figures 25b and 25c illustrate the change in the stress distribution during unloading. Finally, figures 25d through 25f show the same type of distribution as their loading counterparts. Note that Figure 25e exhibits some compressive stresses near the crack tip; however they are within the error bar (uncertainty) of the stress at the base of the craze.

5.2.4 Stress-Displacement Relation

The stress-displacement relation for the cycle is shown in figure 26. The loading curves are denoted with triangles and the unloading ones by squares. The curve at maximum load during the cycle is the solid line with asterisks. As the craze is loaded the stress-displacement relation moves outward from the origin until it reaches the hatched area where it remains for the top one-third of the loading cycle; as the craze is unloaded the stress-displacement relation returns toward the origin during the last third of the cycle. The hatched area can be considered to represent the terminal state of the stress-displacement relation as it reflects the stress-displacement relation of the fully loaded craze fibrils.

The interpretation of the stress-displacement relation in terms of a supramolecular model of the fibrils in the craze will be more complete if one makes use of the crack length surface measurement that was recorded by the other CCD camera.

5.2.5 Crack Length Record

The cyclic data corresponds to cycle 693 of the crack length record shown in figure 27a. The record shows several places where the crack decelerates for some number of cycles before accelerating or jumping. The jumps are better illustrated in the crack length

deviation[16] record which is shown in figure 27b. As the crack decelerates the deviation decreases and as it accelerates or jumps the deviation increases. All of the jumps are about 5 μm in length except for that which occurs just before cycle 1200 where the crack increases its length by about 18 μm.

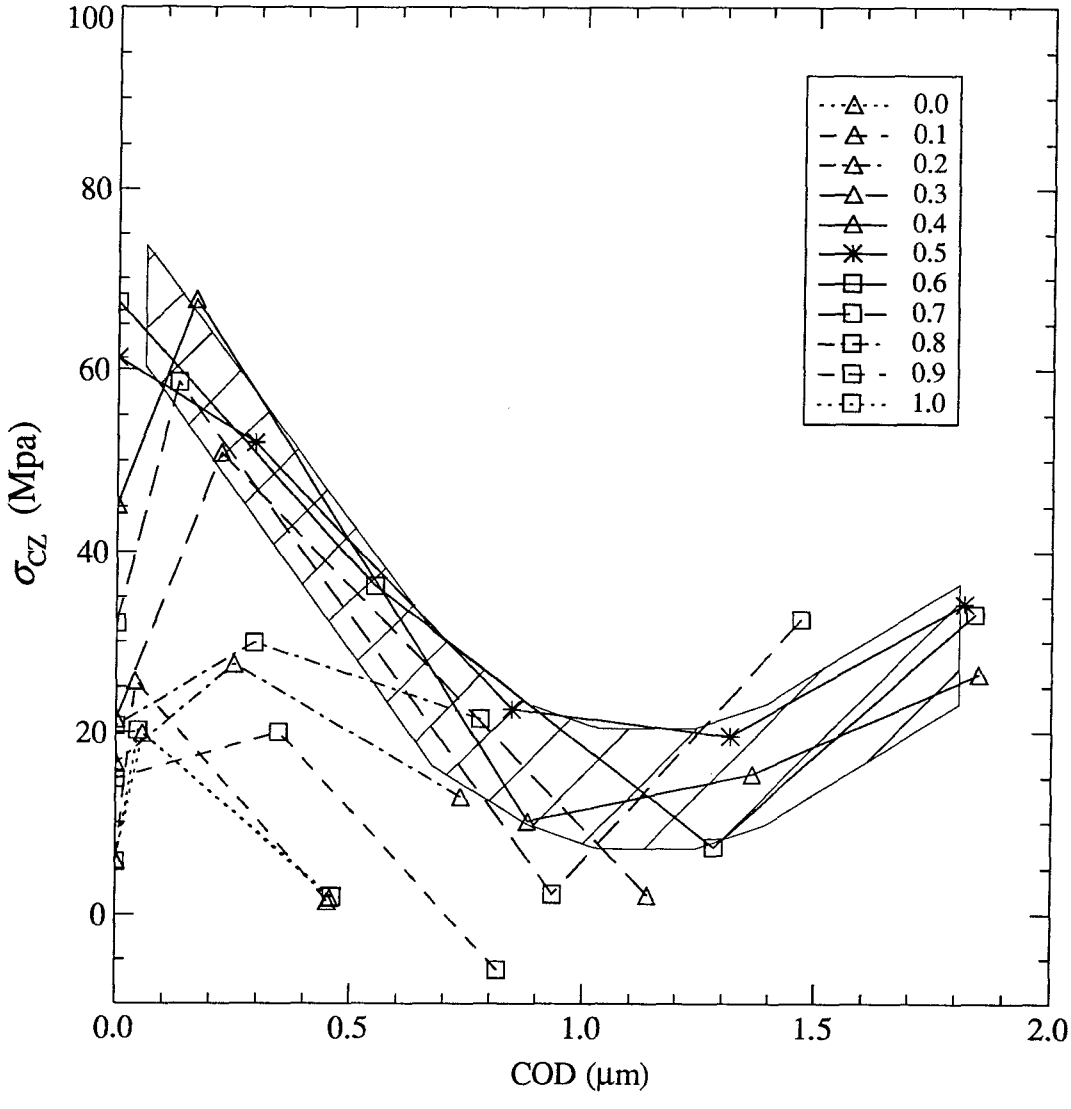

FIGURE 26 Stress-displacement relation during a fatigue cycle.

[16]Crack length deviation is defined as the excursion of the actual crack length from the average length-time trace.

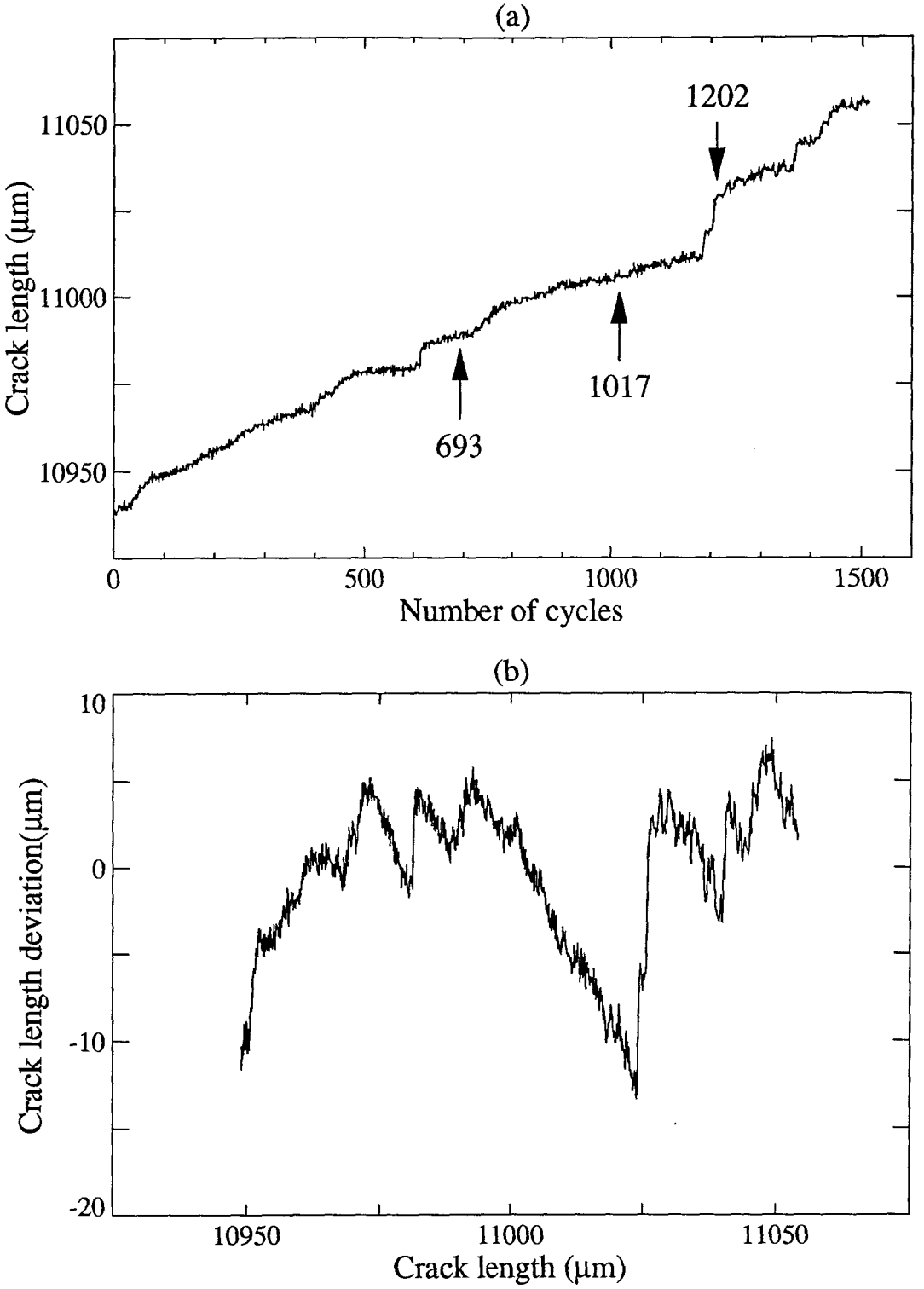

FIGURE 27 Crack length (a) and crack length deviation (b) records of an experiment where the crack jumped by 20 μm.

The craze length was 42 μm at cycle 693 and it decreases to 34 μm at cycle 1017; at the same time the crack length increases by 16 μm so that the craze tip advanced only by 8 μm. Between cycles 1017 and 1202 the crack length propagates by 23 μm while the craze remains the same length; prior to cycle 1200 the crack "jumps[17]" by about 18 μm. The far-field loading can be considered to be constant[18] over the duration of the test. In the next section we will investigate the craze state at cycles 1017 and 1202.

5.2.6 Damage Accumulation

In this section we examine the primordial thicknesses at cycles 1017 and 1202, as well as the stresses during cycle 1202 and the stress-displacement relations for both cycles.

The primordial thicknesses for cycles 1017 and 1202 are shown in figures 28a and 28b respectively. The primordial thicknesses for cycle 1017 are very similar to those of cycle 693 (shown in figure 22a and discussed in section 5.2.1); the spread in the primordial thicknesses at cycle 1017 is slightly larger than that of cycle 693. The analysis of cycle 1017 presents the same problem encountered before: It is not clear how to define the primordial thickness. However, after the crack jumps the primordial thicknesses are closer together and, except for the primordial thicknesses at the bottom part of the cycle (denoted by 0.0 and 1.0), they are amenable to defining a unique primordial thickness for the cycle.

---

[17]The "jump" actually occurs over a period of 50 cycles; however, the growth rate is very large compared to that prior to this period.

[18]Cycling between two constant levels.

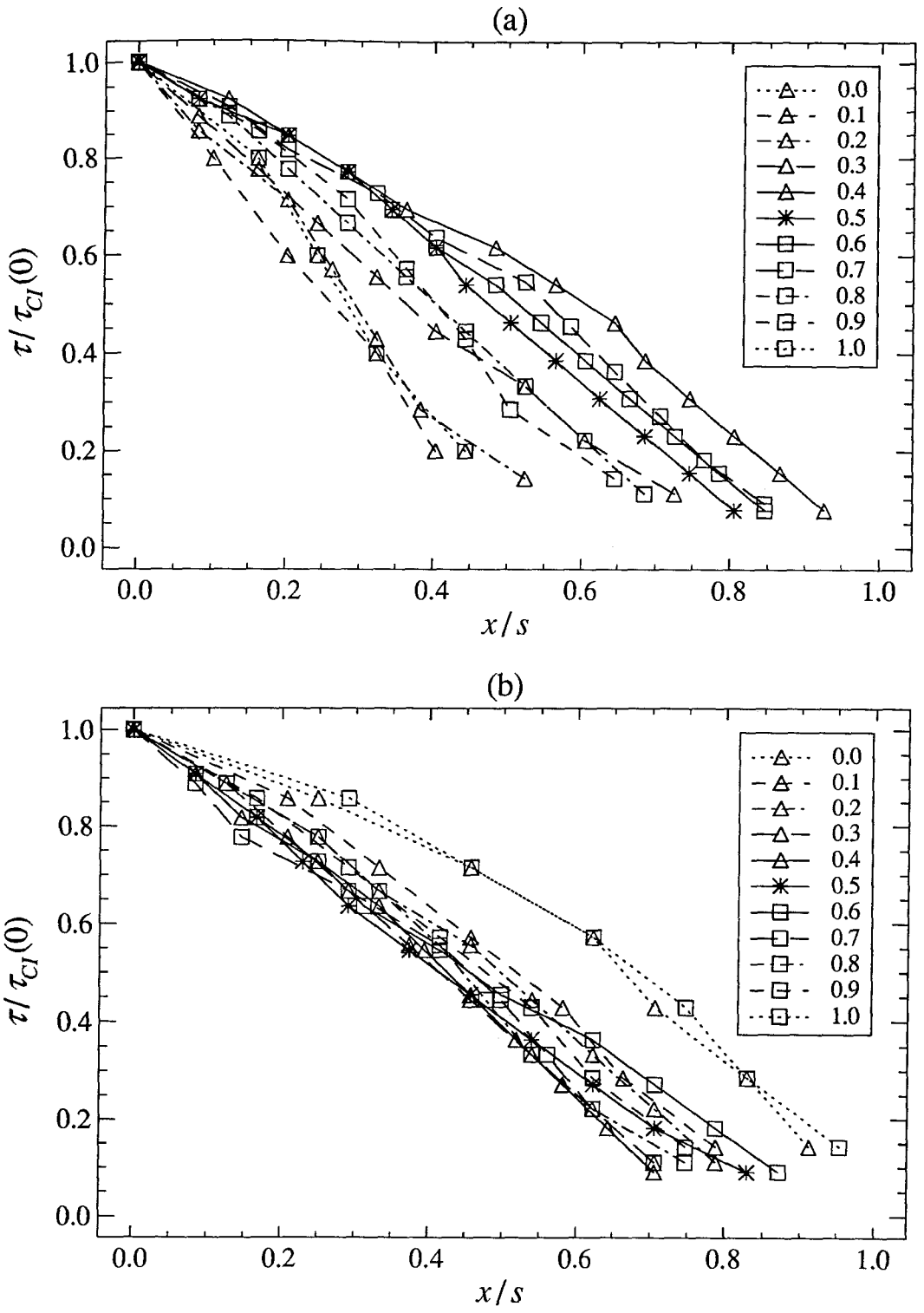

FIGURE 28 Primordial thicknesses using a constant index of refraction during cycles 1017 (a) and 1202 (b).

It should be noted that the variation during the cycle of the average extension ratio[19] is reduced in cycle 1202 as compared to that in cycle 1017. The average extension ratio during cycle 1017 varied between 1.5 and 4.6; during cycle 1202 it varied between 2.2 and 3.8. We will defer an explanation for this reduction until we discuss the stress-displacement relation for both cycles. It may be pointed out, however, that this reduction in the variation of the average extension ratio may be a contributing factor to the better definition of the primordial thickness. In order to avoid confusion in the later results the definition of the primordial thickness used in the analysis of cycle 1202 will be the same as been used so far ('linear/2').

The stresses (along the craze) during cycle 1017 are similar to those of cycle 693 (figures 24 and 25) and will not be shown. The craze stresses during the loading portion of cycle 1202 are shown in figure 29 and those during unloading in figure 30. The two main differences between these stress distributions for the "new" craze and the previous ones are that in this case there is no change in the distribution as the craze is loaded (or unloaded) and that the distribution of stress is different at the bottom of the loading cycle: most of the craze is unloaded except for the tip (figure 29a) whereas before the craze remained loaded (figure 24a) at the bottom of the cycle.

The most striking difference between cycles 1017 and 1202 can be appreciated by looking at the stress-displacement relation during those cycles; it is shown in figure 31. The stress-displacement relation for cycle 1017 is similar to that during cycle 693 except that the drop in stress at medium opening displacements (in the middle of the craze) is more pronounced (about 10 Mpa) and so it is the rise in stress at the base of the craze (about 20 Mpa or 50%).

---

[19]Though it was argued that the extension ratios were ill-defined in the fatigue results due to the ill-definition of the primordial thickness, the average extension ratio is based on the assumption of a constant index of refraction which is itself well-defined since it only depends on the number of extrema in the craze.

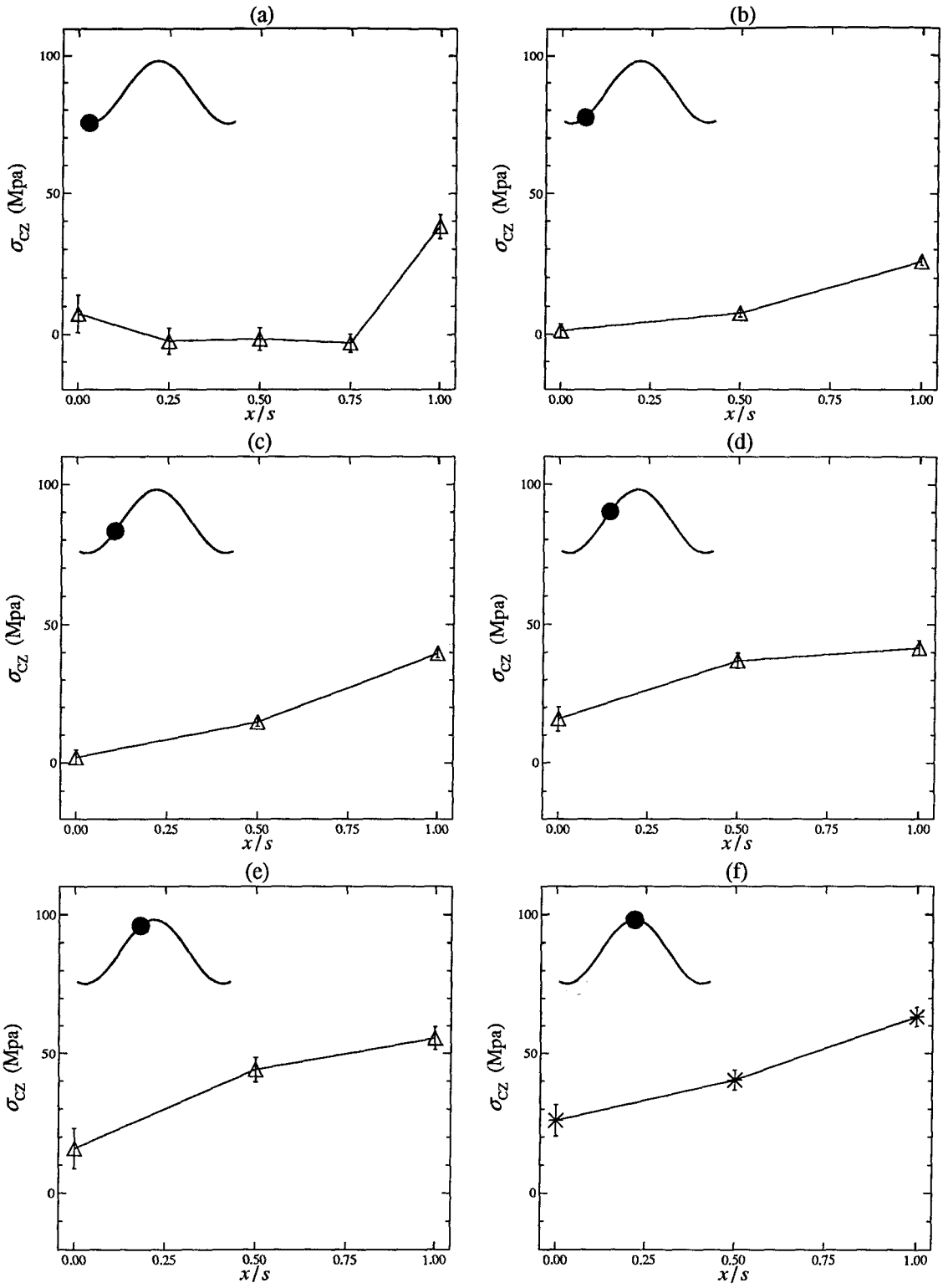

FIGURE 29 Stress distribution along the craze during the loading section of cycle 1202.

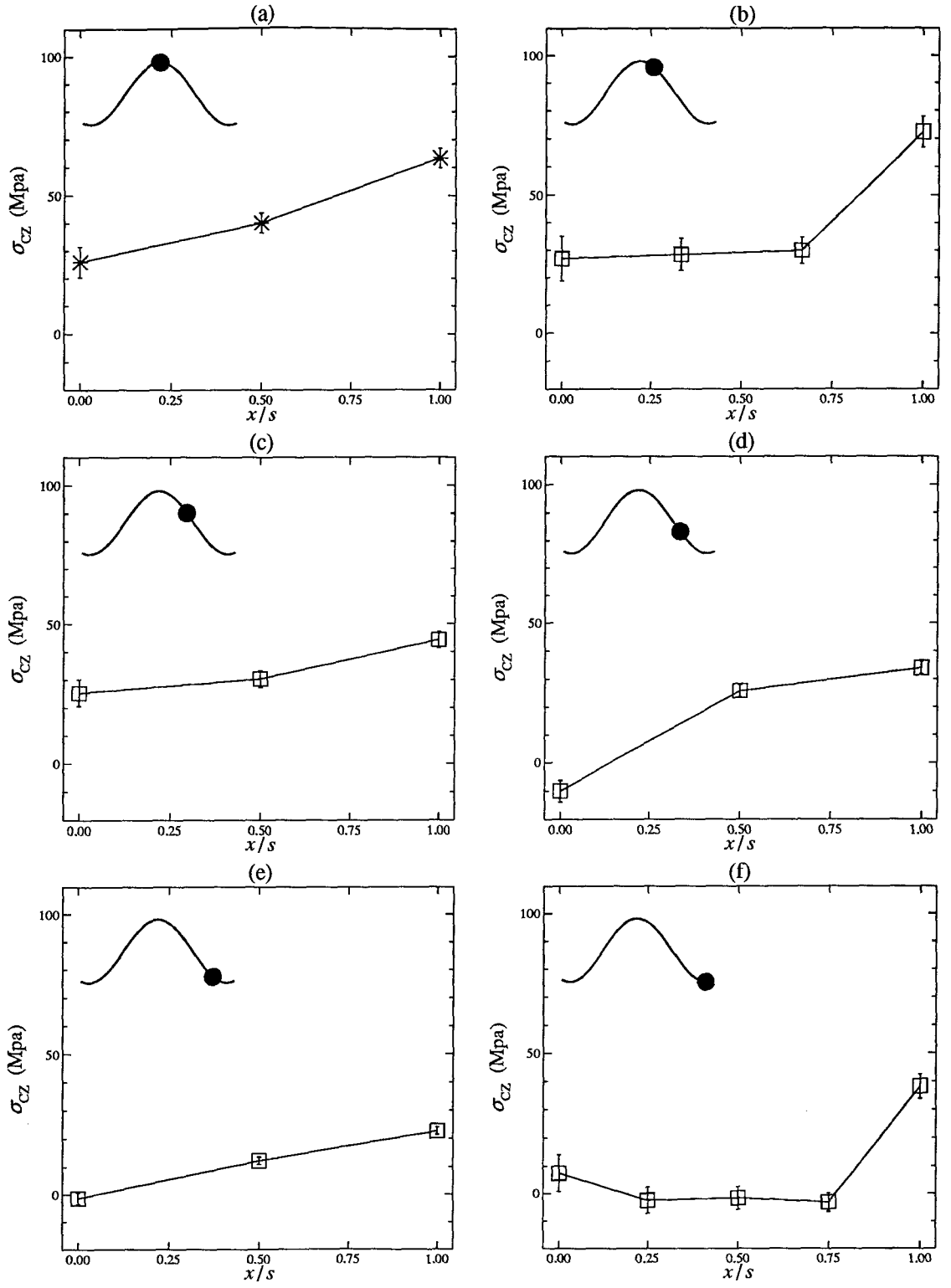

FIGURE 30 Stress distribution along the craze during the unloading section of cycle 1202.

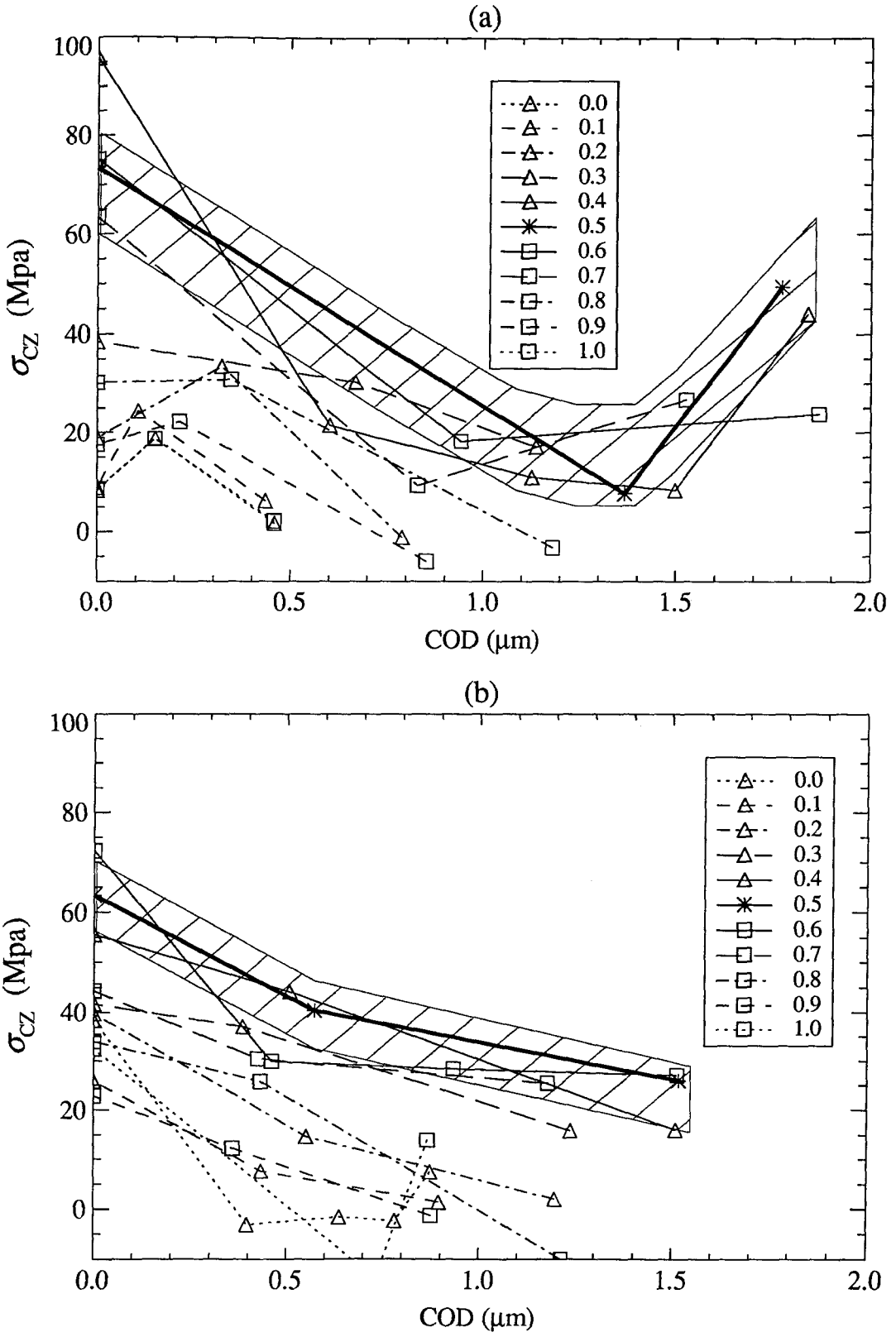

FIGURE 31 Stress-displacement relation during cycles 1017 (a) and 1202 (b).

However, the stress-displacement relation during cycle 1202 is markedly different. It is almost linear with no drop in stress in the middle of the craze. It suggests a model for the fibrils that has not sustained damage because both crack and craze have propagated by a substantial amount (18 μm or about 55% of the craze length) in a short number of cycles. Thus, the "newly" formed craze material has not had the time to accumulate damage.

This issue of damage and having a strong, newly-formed craze during cycle 1202 allows an explanation for the reduction in the variation of the average extension ratio during the cycle: As was mentioned earlier the (externally) prescribed stress intensity factor amplitude is, for all practical purposes, constant. Since the craze length remains the same as the crack jumps (i.e., the craze tip also jumps) the Dugdale stress (equation 25), which is the normalizing stress for the distribution, does not change either. Thus, the craze experiences the equivalent of a prescribed-constant-stress condition and as the material in the craze becomes stronger, the craze responds to the (constant) cyclic stress with a reduced cyclic strain (or extension ratio). We complete the discussion by examining the surface morphology and its relation to the crack length record.

5.2.7 Surface Morphology

The crack length record shown in figure 27a has had its axis inverted and has been scaled to match a photograph of the fracture surface in the area where the experiment that we have described took place; it is shown in figure 32.

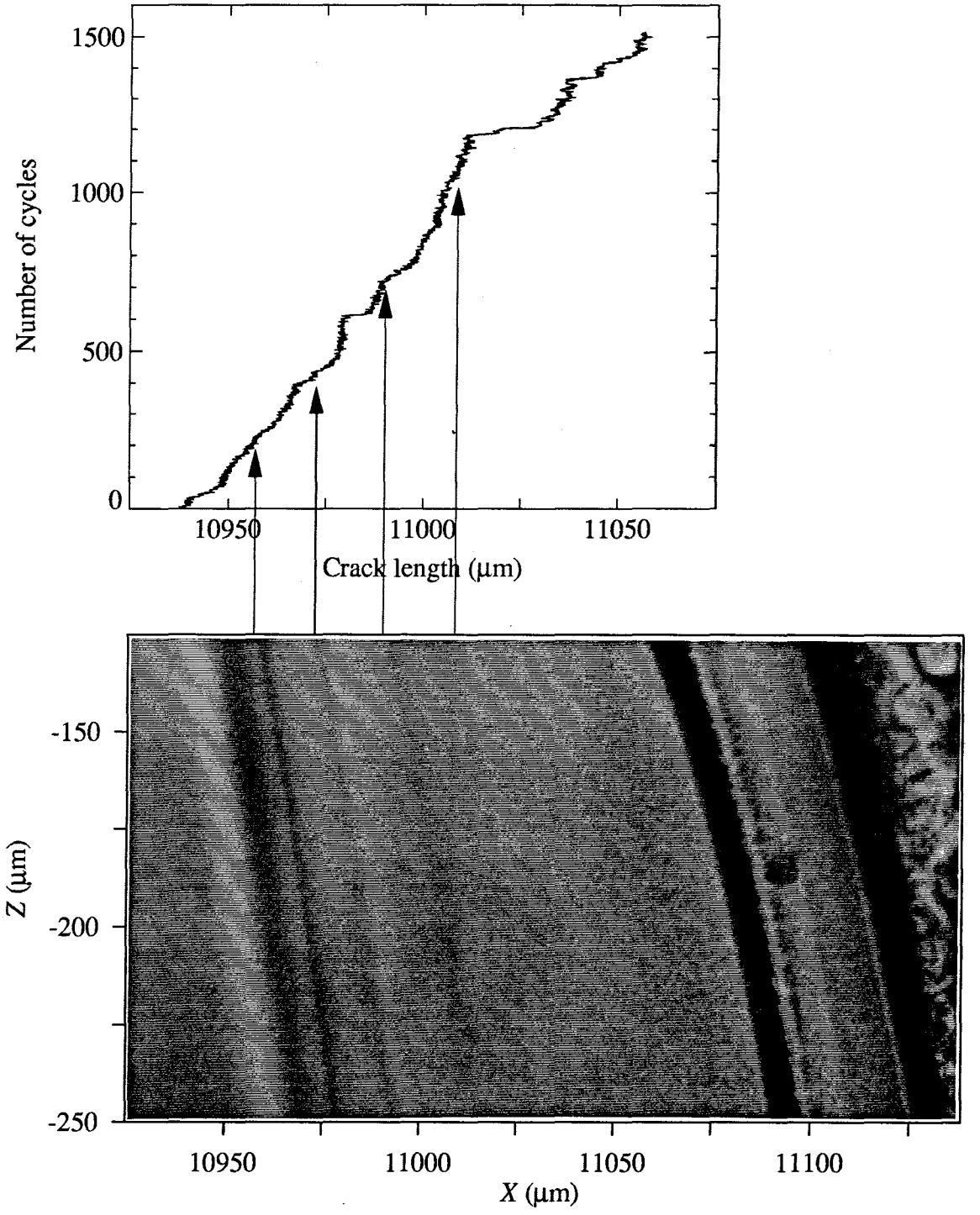

FIGURE 32 Crack length record (a) and fracture surface morphology (b) of an experiment where the crack jumped by 20 μm.

There are four (faint) markings in the fracture surface that are similar to those at the end of the series of experiments that were conducted at a constant stress intensity factor and described in chapter 2. The first marking has the higher contrast because of the original craze position since the original position of the craze tip lies between the second and third markings. The third marking occurred somewhere near cycle 700 while the fourth one occurred in the neighborhood of cycle 1100.

All of the markings (specially the second, third and fourth) seem to be associated with the beginning of the acceleration period and by looking at the record vertically one is reminded of the measurements of Lu Qian and Brown [32]on the discontinuous crack growth in Polyethylene pipes.[20] The crack length record implies that the crack/craze system tended to propagate with decelerating and "jumping" stages with periods of a few microns, and when the crack/craze system failed to decelerate between cycles 800 to 900 (crack length of 11000 μm) and continued to propagate, the failure led to the large jump prior to cycle 1200.

[20]In that case the period of the oscillations is on the order of 1 mm.

6. Conclusions

While it is possible to define a primordial thickness during quasi-static loading, it is not clear how to define it during cyclic loading. This issue points out the dependence of the craze behavior on load history.

In contrast to reports on other investigations of fatigue crack propagation in PMMA it is found that time and rate effects are important. Although analyses based on linear elasticity concepts appear to serve well, it is absolutely necessary to account for relaxation or creep behavior in the bulk material at room temperature.

Rate dependent phenomena are also clearly evident and significant in the response of the crazed material. Noticeable differences in the fracture surface morphology arise when the frequency changes while the stress intensity factor remains constant.[21] Moreover, different time histories of loading, as exemplified by the single load cycle and the continuously applied cyclical loading generate markedly different response characteristics of the craze material.

It appears that the propagation of the crack is associated with a gradual breakdown of the craze, this breakdown being distributed along the length of the craze and not necessarily continuous along its length. The craze breaks along portions of its length to produce crack growth and the mechanical response before and after the advance is different: An "old" or "cycled" craze develops a high cohesion force at its trailing end such as results from strong molecular orientation in the drawing process of the fibrils; this orientation aspect is missing in the "new" craze just after the incremental crack growth has taken place.

---

[21] as noted in section 4.2 of chapter 2.

Kambour's measurements of the index of refraction in an unloaded craze, where there was no variation of the index with distance, may require more detailed considerations before they are applied to a craze under cyclic loading. The minimum stress intensity factor during cyclic loading may play a role on whether compressive stresses develop during the deformation history of the craze. Compressive stresses make the craze opening displacement to be underestimated.

When the fibrils in the craze are newly formed and have not sustained damage they are stiffer and their stress-displacement relation is a straight line. As the damage accumulates there develops a minimum in the stress-displacement relation, accompanied by a hardening of the (presumably) most damaged fibrils. The hardening can be accounted for through the point of view of a molecular force-extension law which may indeed show hardening at very high stretches (high strains that are provided by the approaching crack tip): Because the fibrils at the trailing end of the craze and closest to the crack tip are subject to the largest extension one would expect that the deformation is also associated with increased molecular orientation. The latter phenomenon would clearly invoke the observed increase in cohesive forces in that part of the cycle.

It is now clear (from the minimum in the stress-displacement relation) that the step-wise loading-unloading sequence belonged to a craze that had sustained damage. Nevertheless, it is also apparent that since the craze had rested from its previous cyclic load history and yielded a (fairly) well defined primordial thickness, that comparison with the steadily and cyclically loaded craze forces the conclusion that the mechanical response of the craze exhibits significant rate or history dependent deformation properties.

7. References

1. Berry, J.P., "Fracture Processes in Polymeric Material. 1. The Surface Energy of Poly(methylmethacrylate)," *Journal of Polymer Science*, Vol. 50, 107-115, 1961.
2. Hsiao, C.C. and Sauer, J.A., "On Crazing of Linear High Polymers," *Journal of Applied Physics*, Vol. 21, No. 11, 1071-1083, 1950.
3. Kambour, R.P., "Optical Properties and Structure of Crazes in Transparent Glassy Polymers," *Nature*, Vol. 195, 1299-1300, 1962.
4. Kambour, R.P., "Refractive Index and Composition of Poly(methylmethacrylate) Fracture Surface Layers," *Journal of Polymer Science: Part A*, Vol. 2, 4165-4168, 1964.
5. Kambour, R.P., "Refractive Indices and Composition of Crazes in Several Glassy Polymers," *Journal of Polymer Science: Part A*, Vol. 2, 4159-4163, 1964.
6. Kambour, R.P., "Structure and Properties of Crazes in Polycarbonate and Other Glassy Polymers," *Polymer*, Vol. 5, 143-155, 1964.
7. Lauterwasser, B.D. and Kramer, E.J., "Microscopic Mechanisms and Mechanics of Craze Growth and Fracture," *Philosophical Magazine A*, Vol. 39, No. 4, 469-495, 1979.
8. Donald, A.M. and Kramer, E.J., "The Entanglement Network and Craze Micromechanics in Glassy Polymers," *Journal of Polymer Science: Polymer Physics Edition*, Vol. 20, 1129-1141, 1982.
9. Maestrini, C. and Kramer, E.J., "Craze Structure and Stability in Oriented Polystyrene," *Polymer*, Vol. 32, No. 4, 609-618, 1991.
10. Weidmann, G.W. and Döll, W., "Some Results of Optical Interference Measurements of Critical Displacements at the Crack Tip," *International Journal of Fracture*, Vol. 14, R189- R193, 1978.

11. Döll, W., Seidelmann, U., and Könczöl, L., "On the Validity of the Dugdale Model for Craze Zones at Crack Tips in PMMA," *Journal of Materials Science*, Vol. 15, 2389-2394, 1980.

12. Döll, W., Schinker, M.G., and Könczöl, L., "Direct Measurements of Craze Zones at Crack Tips in Glassy Thermoplastics During Fatigue Crack Growth," in *Deformation, Yield and Fracture of Polymers,* pp. 20.1-20.6, The Plastics and Rubber Institute, London, 1982.

13. Döll, W., Könczöl, L., and Schinker, G., "Size and Mechanical Properties of Craze Zones at Propagating Crack Tips in Poly(methylmethacrylate) During Fatigue Loading," *Polymer*, Vol. 24, 1213-1219, 1983.

14. Schinker, M.G., könczöl, L., and Döll, W., "Micromechanics of Fatigue Crack Propagation in Glassy Thermoplastics," *Colloid and Polymer Science*, Vol. 262, 230-235, 1984.

15. Döll, W., "Optical Interference Measurements and Fracture Mechanics Analysis of Crack Tip Craze Zones," in *Advances In Polymer Science: Crazing in Polymers,* H. Kausch, Editor, Volume 52/53, pp. 105-168, Springer-Verlag, Berlin, 1983.

16. Döll, W. and Könczöl, L., "Micromechanics of Fracture under Static and Fatigue Loading: Optical Interferometry of Crack Tip Craze Zones," in *Advances in Polymer Science: Crazing in Polymers,* H.H. Kausch, Editor, Volume 91/92, pp. 137-214, Springer-Verlag, Berlin, 1990.

17. Elinck, J.P., Bauwens, J.C., and Homes, G., "Fatigue Crack Growth in Poly (Vinyl Chloride)," *International Journal of Fracture Mechanics*, Vol. 7, 277-287, 1971.

18. Gonzalez, R.C. and Wintz, P., *Digital Image Processing,* 2nd Edition, Addison-Wesley, Reading, 1987.

19. Marion, J.B. and Heald, M.A., *Classical Electromagnetic Radiation,* Second Edition, Academic Press, New York, 1980.

20. Doyle, M.J., "The Optical Interference Pattern in a Polystyrene Craze Layer," *Journal of Polymer Science: Polymer Physics Edition*, Vol. 13, 2429-2434, 1975.

21. Könczöl, L., Döll, W., and Bevan, L., "Mechanisms and Micromechanics of Fatigue Crack Propagation in Glassy Polymers," *Colloid and Polymer Science*, Vol. 268, No. 9, 814-822, 1990.

22. Dugdale, D.S., "Yielding of Steel Sheets Containing Slits," *Journal of the Mechanics and Physics of Solids*, Vol. 8, 100-104, 1960.

23. Goodier, J.N. and Field, F.A., "Plastic Energy Dissipation in Crack Propagation," in *Fracture in Solids,* D.C. Drucker and J.J. Gilman, Editor, pp. 103-118, Interscience Publishers, New York, 1963.

24. Rice, J.R., "Mathematical Analysis in the Mechanics of Fracture," in *Fracture; an Advance Treatise,* H. Liebowitz, Editor, Volume 2, pp. 191-311, Academic Press, New York, 1968.

25. Ungsuwarungsri, T. and Knauss, W.G., "A Nonlinear Analysis of an Equilibrium Craze: Part I- Problem Formulation and Solution," *Journal of Applied Mechanics*, Vol. 55, No. 1, 44-51, 1988.

26. Tada, H., Paris, P.C., and Irwin, G.R., *The Stress Analysis of Cracks Handbook,* Del Research Corporation, Hellertown, 1973.

27. Ungsuwarungsri, T., *The Effect of Strain-Softening Cohesive Material on Crack Stability*, Doctoral Thesis, California Institute of Technology, Pasadena, 1986.

28. Imai, Y. and Ward, I.M., "A Study of Craze Deformation in the Fatigue Fracture of Polymethylmethacrylate," *Journal of Materials Science*, Vol. 20, 3842-3852, 1985.

29. Press, W.H., et al., *Numerical Recipes: The Art of Scientific Computing,* Cambridge University Press, Cambridge, 1986.

30. Brown, N. and Wang, X.-q., "Direct Measurements of the Strain on the Boundary of Crazes in Polyethylene," *Polymer*, Vol. 29, 463-466, 1988.

31. Suresh, S., *Fatigue of Materials,* Cambrigde Solid State Science, R.W. Cahn, E.A. Davis, andI.M. Ward, Editor, Cambrigde University Press, Cambrigde, 1991.

32. Lu, X., Qian, R., and Brown, N., "Discontinuous Crack Growth in Polyethylene Under a Constant Load," *Journal of Materials Science*, Vol. 26, No. 4, 917-924, 1991.

Appendix: Stress-Displacement Relation for an *N*-segment Linear Craze Stress Distribution

In this appendix are outlined the steps required for obtaining the displacement of the craze/crack boundary when the distribution of stress along the craze is an *N*-segment linear distribution as shown in figure 9.

Within each segment the non-dimensional stress is given by

$$Q(x) = \frac{Q_{i+1} - Q_i}{x_{i+1} - x_i}(x - x_i) + Q_i. \tag{A.1}$$

If one defines A_i and B_i such that

$$A_i \equiv \frac{Q_{i+1} - Q_i}{x_{i+1} - x_i}; \qquad B_i = \frac{Q_i x_{i+1} - Q_{i+1} x_i}{x_{i+1} - x_i} \tag{A.2}$$

then

$$Q(x) = A_i x + B_i. \tag{A.3}$$

The integral in the constraint condition (equation 23) becomes

$$\frac{1}{2s}\int_0^s \frac{Q(T)}{\sqrt{1-T/s}}dT = \sum_{i=0}^{N-1} A_i \frac{1}{2s}\int_0^s \frac{T}{\sqrt{1-T/s}}dT + B_i \frac{1}{2s}\int_0^s \frac{dT}{\sqrt{1-T/s}}. \tag{A.4}$$

If one defines

$$\begin{aligned} &\xi(T,s) \equiv \xi(T) \equiv \xi_T \equiv \sqrt{1-T/s} \\ &fq2(T,s) \equiv fq2(T) \equiv fq2_T \equiv T\xi(T) - \frac{2s}{3}\xi^3(T) \end{aligned} \tag{A.5}$$

then the constraint condition (equation 23) becomes

$$\sum_{i=0}^{N-1} A_i fq2_T\Big|_{x_i}^{x_{i+1}} + B_i \xi_T\Big|_{x_i}^{x_{i+1}} = -1. \tag{A.6}$$

Upon defining

$$\Delta_i \equiv x_i - x_{i-1} \tag{A.7}$$

equation A.6 can be written as

$$\sum_{i=0}^{N-1} Q_{i+1} \frac{\left(fq2_T - x_i\xi_T\right)_{x_i}^{x_{i+1}}}{\Delta_{i+1}} - Q_i \frac{\left(fq2_T - x_{i+1}\xi_T\right)_{x_i}^{x_{i+1}}}{\Delta_{i+1}} = -1. \tag{A.8}$$

and collecting like terms, one obtains

$$-Q_0 \frac{\left(fq2_T - x_i\xi_T\right)_0^{x_1}}{x_1} + \sum_{i=1}^{N-1} Q_i \left[\frac{\left(fq2_T - x_{i-1}\xi_T\right)_{x_{i-1}}^{x_i}}{\Delta_i} - \frac{\left(fq2_T - x_{i+1}\xi_T\right)_{x_i}^{x_{i+1}}}{\Delta_{i+1}} \right]$$

$$+Q_N \frac{\left(fq2_T - x_{N-1}\xi_T\right)_{x_{N-1}}^{s}}{\Delta_N} = -1 \tag{A.9}$$

Finally one solves for Q_N and obtains

$$\frac{2}{3}\xi_{N-1}Q_N = 1 - Q_0\left(1 - \frac{2s}{3}\left(1 - \xi_1^3\right)\right) + \sum_{i=1}^{N-1} Q_i \left[\frac{fq2_i - x_{i-1}\xi_i}{\Delta_i} + \frac{fq2_i - x_{i+1}\xi_i}{\Delta_{i+1}} - \frac{2s}{3}\left(\frac{\xi_{i-1}^3}{\Delta_i} + \frac{\xi_{i+1}^3}{\Delta_{i+1}} \right) \right] \tag{A.10}$$

If one defines

$$\xi \equiv \sqrt{1 - x/s} \tag{A.11}$$

then the stress-displacement relation (equation 27) can be written as

$$\frac{2v(x)}{2v_D} = 2\xi - \frac{1}{2s}\int_0^s Q(T) \ln\left|\frac{1+\xi/\xi_T}{1-\xi/\xi_T}\right| dT. \tag{A.12}$$

Substituting for $Q(T)$ using equation A.3 we get

$$\frac{2v(x)}{2v_D} = 2\xi - \frac{1}{2s}\sum_{i=0}^{N-1}\int_{x_i}^{x_{i+1}} \left(A_i T + B_i\right) \ln\left|\frac{1+\xi/\xi_T}{1-\xi/\xi_T}\right| dT \tag{A.13}$$

and upon expanding there results

$$\frac{2v(x)}{2v_D} = 2\xi - \frac{1}{2s}\sum_{i=0}^{N-1}\left(A_i \int_{x_i}^{x_{i+1}} T \ln\left|\frac{1+\xi/\xi_T}{1-\xi/\xi_T}\right| dT + B_i \int_{x_i}^{x_{i+1}} \ln\left|\frac{1+\xi/\xi_T}{1-\xi/\xi_T}\right| dT \right).$$

(A.14)

Define

$$\begin{aligned} fv1(x,T,s) \equiv fv1_T &\equiv \xi\xi_T - \frac{x-T}{2s}\ln\left|\frac{1+\xi/\xi_T}{1-\xi/\xi_T}\right| \\ fv2(x,T,s) \equiv fv2_T &\equiv \frac{x+T}{2} fv1(x,T,s) + \frac{s}{3}\xi\xi_T^3 \end{aligned} \qquad \text{(A.15)}$$

so that equation A.14 becomes

$$\frac{2v(x)}{2v_D} = 2\xi + \sum_{i=0}^{N-1}\left(A_i fv2_T\Big|_{x_i}^{x_{i+1}} + B_i fv1_T\Big|_{x_i}^{x_{i+1}} \right) \qquad \text{(A.16)}$$

and using equation A.2 one writes

$$\frac{2v(x)}{2v_D} = 2\xi + \sum_{i=0}^{N-1}\left(Q_{i+1}\left(\frac{fv2_T - x_i fv1_T}{\Delta_{i+1}} \right)_{x_i}^{x_{i+1}} - Q_i\left(\frac{fv2_T - x_{i+1} fv1_T}{\Delta_{i+1}} \right)_{x_i}^{x_{i+1}} \right).$$

(A.17)

Finally, expand equation A.17 into

$$\begin{aligned} \frac{2v(x)}{2v_D} = 2\xi - Q_0 \frac{fv2_T - x_1 fv1_T\Big|_0^{x_1}}{x_1} + \sum_{i=1}^{N-1} Q_i \left(\frac{fv2_T - x_{i-1} fv1_T\Big|_{x_{i-1}}^{x_i}}{\Delta_i} - \frac{fv2_T - x_{i+1} fv1_T\Big|_{x_i}^{x_{i+1}}}{\Delta_{i+1}} \right) \\ + Q_N \frac{fv2_T - x_{N-1} fv1_T\Big|_{x_{N-1}}^{s}}{\Delta_N} \end{aligned}$$

(A.18)

and substitute for Q_N to obtain

$$\frac{2v(x)}{2v_D} = 2\xi + \frac{3}{2\xi_{N-1}} \frac{fv2 - x_{N-1} fv1}{\Delta_N}\Bigg|_{x_{N-1}}^{s} +$$

$$Q_0 \left\{ -\frac{fv2 - x_1 fv1}{\Delta_1}\Bigg|_0^{x_1} - \frac{3}{2\xi_{N-1}} \left(1 - \frac{2s}{3x_1}(1 - \xi_1^3) \left(\frac{fv2 - x_{N-1} fv1}{\Delta_N} \right)^{s}_{x_{N-1}} \right) \right\} +$$

$$\sum_{i=1}^{N-1} Q_i \left\{ \begin{array}{l} \dfrac{fv2 - x_{i-1} fv1}{\Delta_i}\Bigg|_{x_{i-1}}^{x_i} - \dfrac{fv2 - x_{i+1} fv1}{\Delta_{i+1}}\Bigg|_{x_i}^{x_{i+1}} \\ + \dfrac{3}{2\xi_{N-1}} \dfrac{fv2 - x_{N-1} fv1}{\Delta_N}\Bigg|_{x_{N-1}}^{s} \left(\dfrac{fq2_i - x_{i-1}\xi_i}{\Delta_i} + \dfrac{fq2_i - x_{i+1}\xi_i}{\Delta_{i+1}} - \dfrac{2s}{3} \left(\dfrac{\xi_{i-1}^3}{\Delta_i} + \dfrac{\xi_{i+1}^3}{\Delta_{i+1}} \right) \right) \end{array} \right\}$$

(A.19)

which is equation 28, the stress-displacement relation given in the body of the text.

APPENDIX: CLOSED-LOOP CONTROL OF CONSTANT STRESS INTENSITY FACTORS[1]

Abstract

A new way of obtaining a constant stress intensity factor is achieved for any test specimen geometry subjected to closed-loop control loading. In contrast to using only load or displacement control the method draws on combined feedback from both displacement and load sensing, reducing the variation in the stress intensity factor by two decades compared to that if tested under load or displacement control alone. A change in the signal mix ratio for a rectangular compact tension specimen is equivalent to changing the angle of a tapered compact tension specimen. This method can eliminate the need for the use of "complex" geometries or for geometries in which measured crack lengths are used in conjunction with a computer or some other means to adjust the loading continuously for achieving a constant stress intensity factor.

[1]This is the title of a Solid Mechanics Galcit report (SM 92-32) written in September 1992 and submitted for publication to the International Journal of Fracture.

1. Introduction

Today fracture mechanics is able to deal rather effectively with material situations which require nonlinear material descriptions. Although under these circumstances the crack tip characterization in terms of a linearized stress field is of limited usefulness, there are many situations in engineering applications when a stress intensity factor is an important parameter for the description of crack propagation behavior. Notable are those conditions involving low stress failures such as fatigue in many materials, as well as failure of time dependent materials when low stress levels lead to long term fracture. Even in cases when local crack tip conditions seem to violate the assumptions of the linearized field equations, an approximate characterization in terms of a stress intensity factor provides an important reference evaluation.

In engineering situations requiring the study of crack propagation rates as a function of specimen loading is usually desirable to provide material data in terms of the stress intensity factor. For efficient use of test time and to assert the validity of crack propagation models it is then also desirable that the stress intensity factor remain constant during crack growth. An additional important consideration in the case of rate sensitive materials may be that one wants or needs to eliminate transients in crack growth resulting from changes in load or stress intensity factor.

Because in most practical test geometries crack enlargement produces continual changes in the stress intensity factor, special efforts are necessary to generate conditions for constancy of this quantity; these efforts have proceeded along two paths: First, by designing a test geometry so that the stress intensity factor changes minimally as the crack length increases during a test. Examples of these geometries are the modified double cantilever beam (DCB) specimen of Mostovoy and Ripling [1] and the "strip

biaxial specimen" used first by Rivlin and Thomas for compliant materials [2]. Additional solutions to deal with this problem are alluded to in references [3-9].

Efforts along the second path to obtain constant stress intensity factors have been to monitor the crack length and, together with the theoretical dependence of the stress intensity factor on crack length, to reduce the loading in a stepwise fashion to compensate for crack enlargement. Swanson et al. [10] reduced the load manually at fixed increments of crack length, while more recently, Zuidema and Mannesse [11] used a computer to control the load reduction. Using a computer to record both the load and displacement, and knowing the theoretical displacement-crack-length relation for a DCB specimen, Nicholson bypassed the crack length measurement [12] while still being able to calculate the necessary load reduction (see the discussion section below). In a somewhat different approach to the problem Dillard developed more recently a nonlinear loading mechanism for a DCB specimen under constant load which just compensates for the change in stress intensity factor due to crack enlargement [13].

The present work is the outgrowth of a study concerned with the details of crack growth in polymers under fatigue loading. Part of that study was the construction of a servohydraulically controlled micro-loading device which may be viewed as a miniature MTS or Instron machine completely interfaced with a digital computer for control purposes.[2] Part of that equipment design was the automatic computer acquisition of crack tip location with a precision of $\pm 1\mu m$; although it would have been possible to use that rather precise information for feedback control and to then continually correct for the changing geometry, an alternate means which has more general applicability even when such monitoring of the crack extension is not feasible was found to provide an excellent means of controlling the stress intensity factor at constant levels.

---

[2] This loading device was designed and constructed at Caltech with maximal load capability of 700 N and symmetric displacement capability to keep the crack tip stationary in front of a microscope; displacement can be controlled to $\pm$ 1 μm.

The method consists in principle of controlling both the load and the displacement imposed on a test specimen in a suitably proportioned manner. Superficially it may appear on the basis of elasticity considerations that it is not feasible to prescribe both forces and displacements simultaneously at the same point; however, it turns out that this simultaneous prescription of force and displacement can be imposed effectively. In essence the method makes use of the continuously sensed stiffness of the specimen and employs that information to also continuously control the loading in such a manner so as to achieve a constant stress intensity factor while the crack length changes.

In the sequel we describe first the analysis underlying this method applied to a compact tension specimen as an example and indicate by comparison with experiments how well that control has been achieved. We find this method readily applicable to any closed-loop loading device so long as it can use the load or displacement for feedback.

2. Theory

The stress intensity factor K_I for cracked plates of width W and thickness t with a crack length a can be expressed, with P as the applied load, as

$$K_I = \frac{P}{t\sqrt{W}} Y(\alpha) \tag{1}$$

where

$$\alpha = a / W \tag{2}$$

is the non-dimensional crack length and $Y(\alpha)$ is a function (usually called the calibration factor or geometry correction factor) that depends on the geometry and the location where the load is applied. The compliance of the cracked plate is defined as

$$C = \frac{u}{P} \tag{3}$$

with u as the displacement at the load point. Using equations (1) and (3), the stress intensity factor for prescribed displacement is

$$K_I = \frac{u}{t\sqrt{W}} \frac{Y(\alpha)}{C(\alpha)}. \tag{4}$$

For a linearly elastic body the compliance C is related to $Y(\alpha)$ through the energy release rate

$$\mathcal{G} = \frac{P^2}{2t} \frac{\partial C}{\partial a} = \frac{K_I^2}{\tilde{E}} \tag{5}$$

where $\tilde{E} = E$ (Young's Modulus) for plane stress and $\tilde{E} = E / (1 - \upsilon^2)$ for plane strain. Thus, one has

$$Y(\alpha) = \sqrt{\frac{\tilde{E} t}{2} \frac{\partial C}{\partial \alpha}} \tag{6}$$

and equation (4) becomes

$$K_I = \sqrt{\frac{\tilde{E}}{2tW}}\, u \frac{\sqrt{\partial C/\partial \alpha}}{C(\alpha)}. \qquad (7)$$

Equations (1) and (7) give the stress intensity factor for a prescribed load or displacement, respectively. Equation (1) has been the motivation behind past work to obtain constant K_I by means of designing a geometry for which $Y(\alpha)$ is constant over some range of α [1-4, 6-9, 14] while the load is kept constant with time or, knowing the function $Y(\alpha)$ and measuring the crack length a, by adjusting the load P (either by hand or through the use of a computer) so as to keep K_I constant.

For most geometries used in fracture studies the calibration factor $Y(\alpha)$ is a monotonically increasing function of α so that under a constant load, the stress intensity factor K_I will increase with crack enlargement. On the other hand, one can see from equation (7) that K_I will decrease with crack propagation under a constant displacement u (for any particular α, $C(\alpha) \sim C_0 \alpha^b$ with $b > 0$, and $K_I \sim K_0 \alpha^d$ with $d = -(b+1)/2 < 0$). One might expect thus, that a feedback signal which is somewhere between a displacement and a load feedback may yield constant stress intensity factors.

We consider, therefore, crack propagation testing using a combined feedback, that is, a feedback which is a linear combination of load and displacement in the form

$$(1-R)u^* + RP^* = V_{FB} \equiv V_C \qquad (8)$$

where R is called the mixing ratio, V_{FB} is the feedback voltage, and by definition of a servomechanism, equal to the command voltage V_C, and

$$u^* = u g_u \qquad (9a)$$

$$P^* = P g_P \qquad (9b)$$

are the normalized displacement and load, respectively, with g_u and g_P being the d.c. gains (Volts/meter and Volts/Newton) of the displacement and load transducers.

At this point a few comments are in order: First, we shall consider initially mixing ratios between 0 and 1 inclusively; the possibility of using mixing ratios greater than 1 will be discussed later. Second, this type of feedback reduces to displacement feedback when the mixing ratio equals 0 and it reduces to load feedback when the mixing ratio reaches 1. Third, we expect that for geometries in which the stress intensity factor increases with crack growth, the mixing ratio yielding constant stress intensity factors lies between 0 and 1. Fourth, the loading device will be stable under combined feedback if it was stable under both displacement feedback and load feedback.

There are two issues one must address with regards to this new type of feedback namely whether or not it is feasible to test a geometry under combined feedback and then, what the behavior of the stress intensity factor is under combined feedback. The overall feasibility issue must be addressed in terms of the performance[3] and stability of the loading device.

The performance of a position servomechanism depends normally on its loop velocity gain [15], which is proportional to the gain of the displacement transducer g_u. When the loads involved are small compared to the maximal load of the loading device, the performance of the system under load feedback (or in this case under combined feedback) will depend on the gain of the equivalent displacement transducer g_R^u. The gain of the equivalent displacement transducer g_R^u is the ratio of the feedback voltage and the displacement: from equation (8) one obtains

$$g_R^u = (1-R)g_u + Rg_P / C. \qquad (10)$$

It is clear that as R is varied from 0 to 1 the gain g_R^u varies linearly from g_u to g_P / C which is the gain of the equivalent displacement transducer under load control. Thus if the system is stable and the performance is acceptable at the end points (displacement

[3]In this context, the performance of the servomechanism refers to the uncertainty in the position output, the "following" error (error in the output when the input is one with constant velocity) and the closed-loop stiffness. All of these quantities are optimized when the loop velocity gain is maximized.

feedback and load feedback), so will it be under combined feedback. If one assumes that g_u was chosen to optimize the performance and stability of the loading device without a specimen, and if g_P is chosen such that it equals $C g_u$, then the gain of the equivalent displacement transducer is independent of R and the performance and stability of the system will be optimized for all possible types of feedback. It is worthwhile to note that as the crack propagates and the compliance increases the performance of the system will be degraded for any type of feedback except displacement feedback. However, this degradation in performance for combined feedback is no worse than that when the loading device is operated under load feedback.

We now address the second issue with regard to this new type of feedback: the behavior of the stress intensity factor under combined feedback. Using equations (3), (8) and (9), we solve for the load and substitute for it in equation (1), to obtain

$$K_{\mathrm{I}} = \frac{\hat{P}}{t\sqrt{W}} Y_R(\alpha;\gamma) \tag{11}$$

where

$$\hat{P} = \frac{V_{FB}}{g_P} \equiv \frac{V_C}{g_P} \tag{12}$$

is the interpretation of the command signal as a load and

$$\mathrm{Y}_R(\alpha;\gamma) = \frac{\mathrm{Y}(\alpha)}{(1-R)\gamma\overline{C}(\alpha)+R} \tag{13}$$

is the calibration factor for the combined feedback, with

$$\overline{C}(\alpha) = \tilde{E}tC(\alpha) \equiv 2\int_{\alpha_0}^{\alpha} \mathrm{Y}^2(x)dx + \overline{C}(\alpha_0) \tag{14}$$

being the non-dimensional compliance and

$$\gamma = \frac{1}{\tilde{E}t}\frac{g_u}{g_P} \tag{15}$$

is a non-dimensional parameter related to the test geometry and the transducers; from the previous discussion it depends on the (optimized) performance of the loading device.

At this point, it is useful for demonstration purposes to choose a specific geometry and examine the behavior of the stress intensity factor under combined feedback. Let us consider the geometry of a compact tension specimen with a half-height-to-width ratio h/W of 0.4. The function $K_I t\sqrt{W} / \hat{P}$ for this case is plotted in figure 1a for several mixing ratios R. In order to compare the results of the present process with those achieved by tapering the upper and lower edges of the specimen, figure 1b shows boundary collocation data of Srawley and Gross [14] for an edge-cracked tapered plate possessing several values of h/W and taper angle θ.

It is clear that the use of the combined feedback for a rectangular specimen has a similar effect to the taper of the edges for a specimen tested under load feedback. In both cases one can "shape" the calibration factor and obtain regions where the stress intensity factor remains approximately constant for some ranges of crack length. We now focus on finding the mixing ratio which will minimize the variation of the stress intensity factor for a particular range of crack lengths.

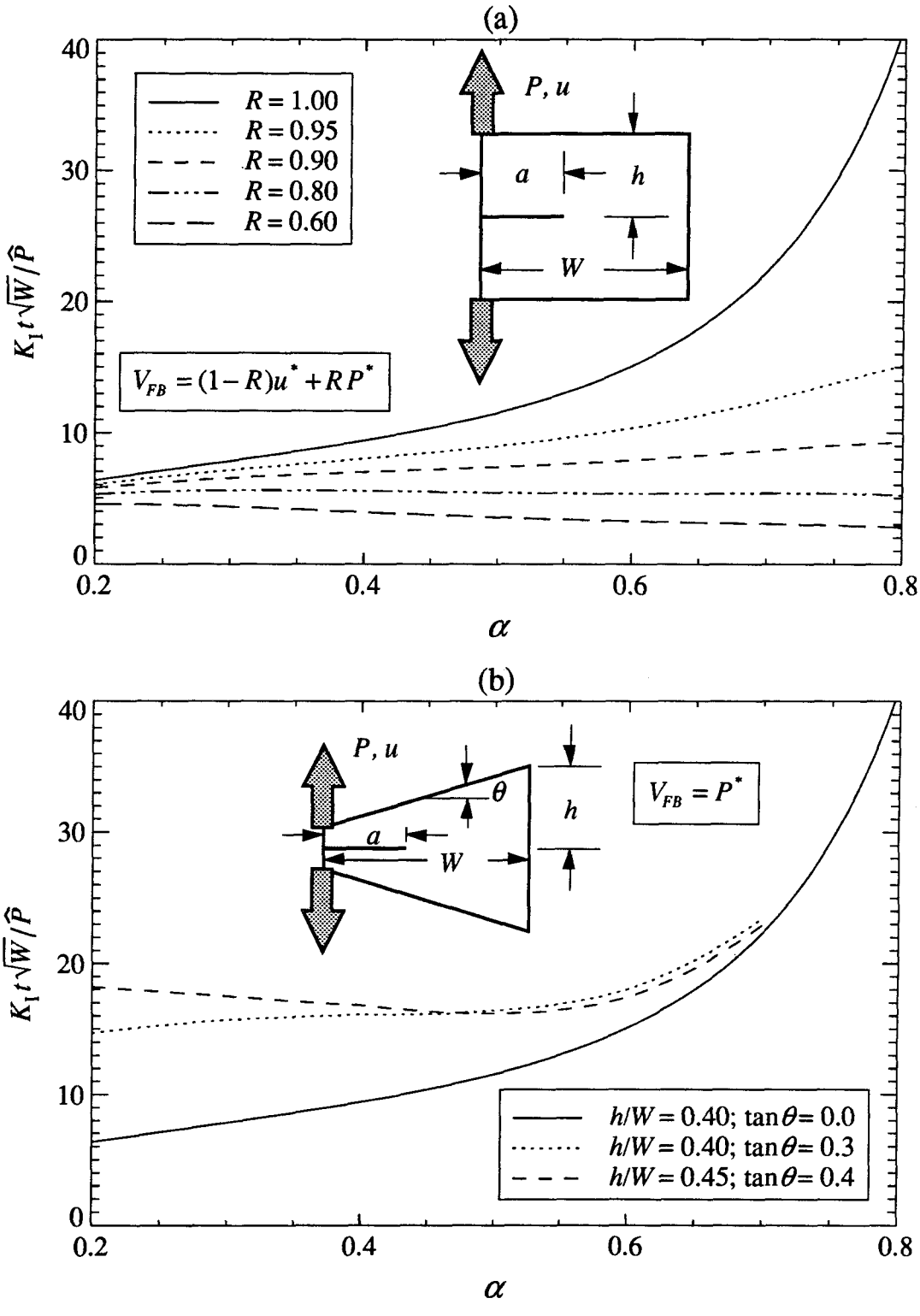

FIGURE 1 Comparison of calculated stress intensity factors K_I in a rectangular edge-cracked plate under combined feedback (a) and a tapered edge-cracked plate under load feedback (b) ($\alpha = a / W$).

For any given range of crack lengths one finds the mixing ratio that minimizes the variation in the stress intensity factor by looking for the maximum and minimum stress intensity factors in that given range of crack lengths as the mixing ratio is varied from 0 to 1. This optimum mixing ratio can then be plotted against the crack length in the center of the range to see its dependence on crack length. An analytical relation of this dependence can be obtained if one assumes that the calibration factor for the optimum mixing ratio will have an extremum at the center of the range of crack lengths considered; this is the case as the range is reduced to zero. Setting the partial derivative of $Y_R(\alpha;\gamma)$ with respect to α equal to zero produces

$$\frac{((1-R)\gamma\overline{C}+R)Y' - Y(1-R)\gamma\overline{C}'}{((1-R)\gamma\overline{C}+R)^2} = 0. \qquad (16)$$

Since $\gamma\overline{C} > 0$, the denominator will be zero only for values of $R > 1$ or $R < 0$, whereas we only admit mixing ratios between 0 and 1; denoting the mixing ratio that produces an extremum for the calibration factor by R_K leads to

$$R_K = \frac{\gamma\overline{C}(\overline{C}'Y/\overline{C}Y'-1)}{1+\gamma\overline{C}(\overline{C}'Y/\overline{C}Y'-1)}. \qquad (17)$$

In order to gain a better understanding into the behavior of the optimum mixing ratio obtained from a search procedure and its comparison to R_K we again choose the same particular geometry as before: the compact tension specimen with a half-height-to-width ratio *h/W* of 0.4. Figure 2 shows the behavior of R_K and the optimum mixing ratio for several ranges of crack lengths. It appears that the approximation of R_K to the mixing ratio that minimizes the variation in the stress intensity factor is excellent for crack length ranges less than 5% of the width of the specimen. The difference between the mixing ratios becomes noticeable only when the range of crack lengths exceeds 10%. In terms of typical dimensions of W= 10 cm, this means crack growth of 1/2 to 1 cm.

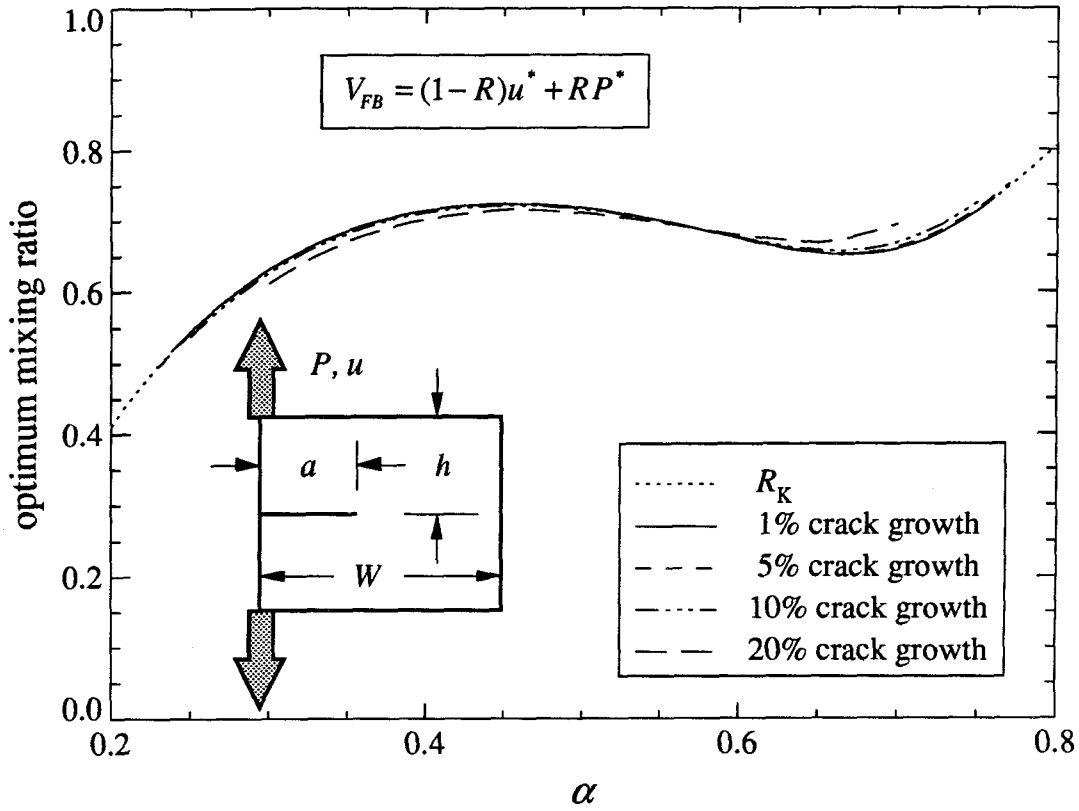

Figure 2 Mixing ratio (R) of load and displacement needed to minimize the variation of the stress intensity factor during crack propagation under combined feedback ($\alpha = a / W$).

3. Experimental Results

After incorporating the capability of using the combined feedback into our loading device, some experiments were performed to examine the effects of the mixing ratio on the stress intensity factor. The geometry of the specimens is the same as used above for illustrative purposes. The experiments were conducted under cyclic (fatigue) loading with the prescribed command signal, and hence the feedback signal, a time-varying sinusoidal of constant amplitude and mean.

The stress intensity factors are calculated according to equation 1 after obtaining a load and crack length record. The maximum stress intensity factor and the amplitude of the stress intensity factor were calculated for each loading cycle by using the maximum load, load amplitude and crack length in the cycle. Both the maximum and the amplitude of the stress intensity factor exhibit the same behavior however, because it is more common in fatigue experiments to characterize fracture behavior in terms of the amplitude, figure 3 shows the resulting amplitude of the stress intensity factor for several mixing ratios. The material is poly(methylmethacrylate) (PMMA) with E= 3.4 GPa and the dimensions of the specimen were: W= 40.0 mm, h= 16.0 mm and t= 2.85 mm; the d.c. gains of the transducer were such that the resulting value for γ was 0.052.

When the feedback follows the displacement or load only the variation in ΔK_I is about 10 to 15% for a crack length increase of 5% of the width. On the other hand the use of a mixing ratio of 0.65 and 0.70 reduces the variation in ΔK_I to about 1/4 to 1/2% for the same 5% increment in crack length. These mixing ratios that produced nearly constant stress intensity factors correspond very well to the optimum mixing ratios of figure 2 when the value for γ was 0.05.

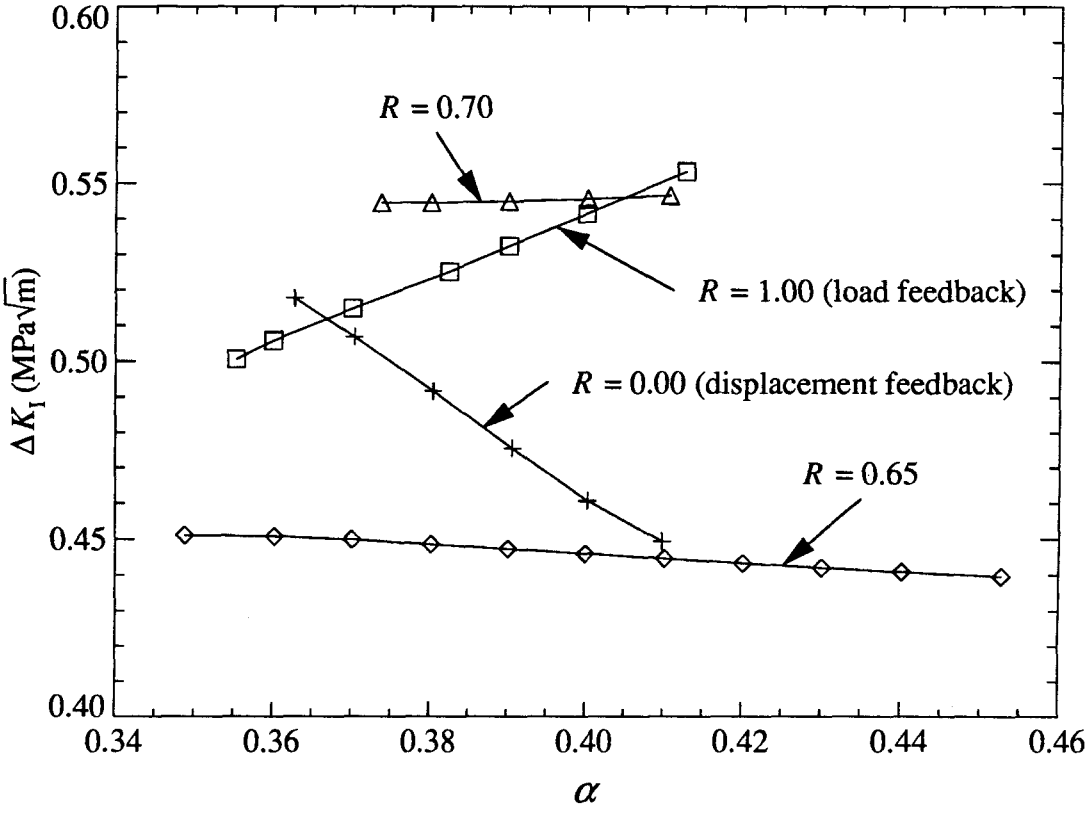

FIGURE 3 Experimentally obtained[4] stress intensity factor amplitudes ΔK_I^{exp} for different mixing ratios R under combined feedback ($\alpha = a / W$).

[4]Only a few data points are used for display purposes; however, the number of points in each plot ranges from 2500 to 6000.

4. Discussion

We have seen that combining the load and displacement signals for control purposes provides a means of holding the stress intensity factor at constant levels. The mixing of the displacement into the feedback cannot only be viewed as a combined feedback, but upon rewriting equation (8) as

$$\hat{V}_{FB} = RP^* = V_C - (1-R)u^* \qquad (18)$$

one can interpret the additional displacement signal as a reduction in the command signal of a loading device operating under load feedback (with an effective d.c. gain of Rg_P). This interpretation is then similar to the work of Nicholson [12] in which a computer was used to acquire the load and displacement, and after some real time calculations,[5] based on the analytical relation between load and crack length for the specimen under consideration the command signal is modified so as to keep the stress intensity factor constant. In the present case, however, the specimen acts as its own computer in calculating the load reduction. Any change in the compliance is sensed through the displacement and, being interpreted as a crack enlargement, results in a reduction in load accordingly to the preset mixing ratio.

The testing at constant stress intensity factor levels under a combined feedback can be accomplished with the use of a constant command signal or a time varying sinusoid with constant amplitude and mean in the case of fatigue. The use of a constant command signal eliminates the steps in the loading which may cause transient crack growth behavior in rate sensitive materials. In addition, a measurement of the crack length is not required, thus simplifying the testing at constant levels of the stress intensity factor. Eliminating the need for a crack length measurement offers two advantages: First, the crack length can be recorded (if one still wants an additional measurement) at a slower

[5] The load and displacement are acquired 10 times/second, and the average rate of change of these quantities with respect to time is used to control the crosshead speed of the test machine.

rate since it does not enter the feedback loop, thus allowing the use of high precision albeit slower, techniques. Second, the decision as to what the correct crack length should be, in cases where there is a substantial amount of tunneling, is deferred until the test is finished. Determining the equivalent (straight crack front) crack length is made easier since more information is available, such as observations of the fracture surface and recordings of the internal crack opening displacement in transparent specimens.

In order to determine more precisely how well this technique maintains the stress intensity factor at constant levels, one can examine the relative variation in K_I when the crack propagates a given amount. The relative variation in this case is defined as the maximum change in stress intensity factors when the crack propagates by 5% of the width W of the specimen divided by the stress intensity factor at the center of the range. Shown in figure 4a is the relative variation of the stress intensity factor for different crack lengths as the mixing ratio R varies from 0 (displacement feedback) to 1 (load feedback). The ratio corresponding to the cusps in these curves is the optimum mixing ratio previously shown in figure 2; the new information here is the variation of K_I. The bottom graph, figure 4b, shows the relative variation of K_I against the non-dimensional crack length for several mixing ratios. The top two curves in this figure correspond to displacement feedback ($R= 0$) and load feedback ($R= 1$) with a variation in K_I of approximately 10%. The other curves correspond to combined feedback; the solid line is the result for the optimum mixing ratio calculated to 3 significant figures, while the dotted curve (R= opt2) corresponds to the optimum mixing ratio calculated to 2 significant figures. The dotted curve intersects the solid one when the mixing ratio (expressed to 2 significant figures) matches the optimum mixing ratio. This curve can be used to estimate the sensitivity of the mixing ratio: When it is "tuned" from 2 to 3 significant figures the variation may be reduced anywhere from a factor of 2 to a factor of 10. The remaining two curves correspond to constant mixing ratios, and intersect the

solid curve at a discrete number of places namely when those mixing ratios correspond to the optimum.

When testing under combined feedback at the optimum mixing ratio the variation of K_I is reduced on the average by a factor of 2 decades compared to the situation when testing under load or displacement feedback. While it is clear that the variation of K_I will depend on the amount of crack enlargement, the graph in figure 4b shows that the variation of K_I at the optimum mixing ratio depends also on the crack length itself. In this particular example of a rectangular edge-cracked plate with a half-height-to-width ratio h/W of 0.4, the smallest variation is obtained when the crack length is about 45% of the width W; this crack length corresponds to the point at which the optimum mixing ratio (figure 2) has the largest radius of curvature.

It is also clear from figure 4a and also from the dotted curve in the figure 4b that one must be rather precise in choosing the mixing ratio in order to obtain the highly reduced variation in the stress intensity factor; any deviation from the optimum mixing ratio will result in a more sizable increase in the variation of K_I due to the large slopes of the curves near the cusps.

The combined feedback used in this work is a very simple one: the addition of the displacement to the load feedback. It is also clear why this type of feedback can be used to obtain constant stress intensity factors: the increase of displacement (due to the increase of compliance) derived from crack propagation, achieves the necessary load reduction when the sum of load and displacement is kept constant. The mixing ratio determines for a particular geometry (height-to width ratios, crack length, etc.), the amount of displacement that must be mixed in so that the load reduction is inversely proportional to the load calibration factor.

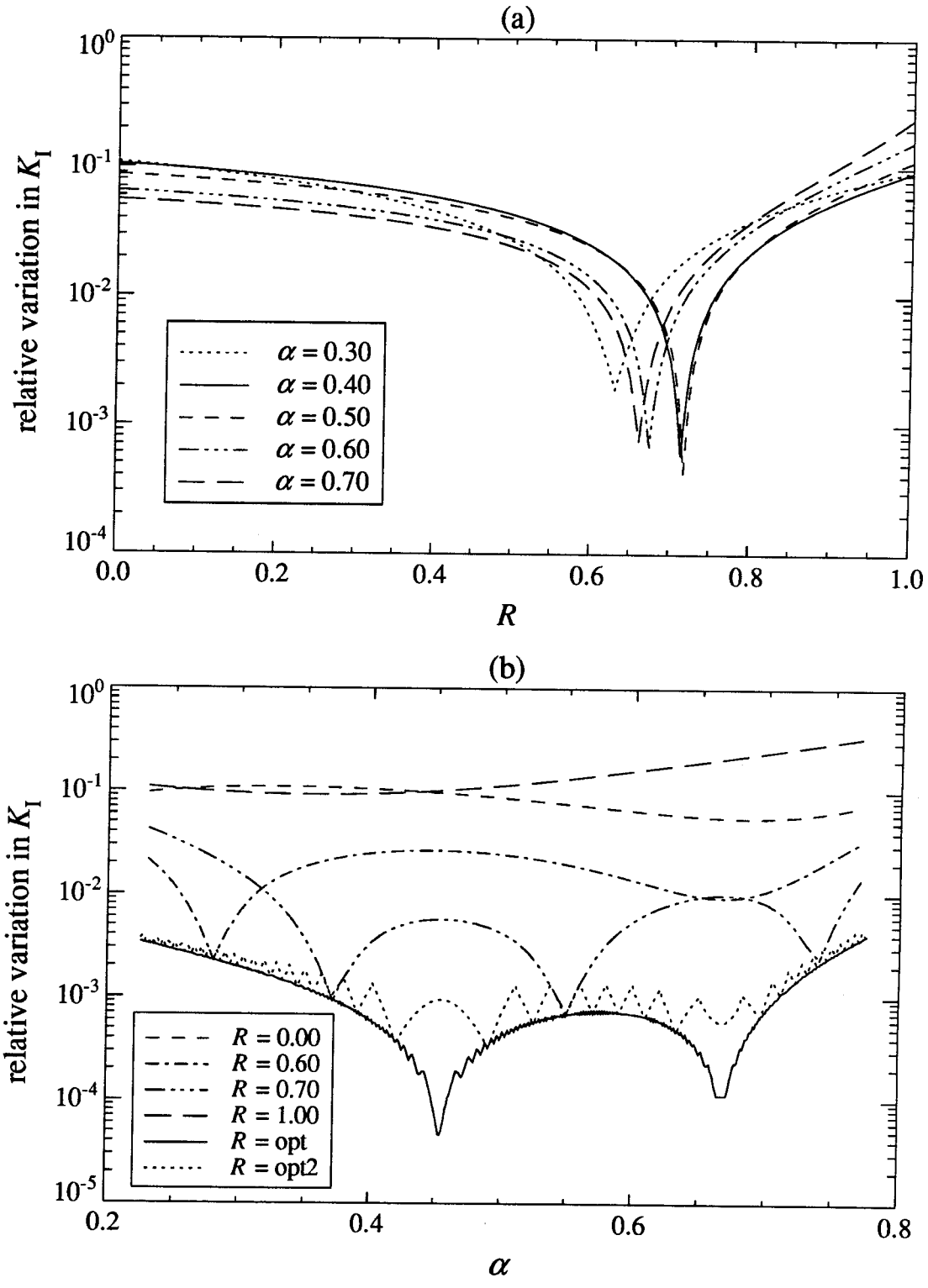

FIGURE 4 Relative deviation of the Stress Intensity Factor over a 5% crack length increase in a rectangular edge-cracked plate under combined feedback. The deviation is plotted versus the mixing ratio (a) and versus the crack length (b) ($\alpha = a/W$).

In addition, having a displacement proportional to the load allows this type of feedback to be used in fatigue studies: the mixing of the displacement into the load feedback does not introduce any phase lags nor does it distort the shape of the command signal even when it is a time-varying sinusoidal.

5. Other Types of Feedback

Once the realization is made that both the load and displacement can be used simultaneously in the feedback loop, it opens the door to additional types of feedback: multiplying the load and displacement together in the feedback loop can be used to test under conditions of constant elastic strain energy; adding this non-linear term to the feedback discussed in this work would provide an additional parameter which could be used to obtain even better control of the stress intensity factor levels by providing an inflection point at a single crack length or an extremum at two different crack lengths.

The underlying assumption made to obtain nearly constant stress intensity factors using the combined feedback technique (in conjunction with a constant command signal) has been that the calibration factor for the geometry under consideration must be a monotonically increasing function of the crack length. As the geometry is tested with a mixing ratio equal to 0 (displacement feedback) K_I decreases with crack growth, but by the time the mixing ratio has reached 1 (load feedback) K_I is increasing with crack growth; hence, the condition for constant K_I placed somewhere between displacement feedback and load feedback ($0 < R < 1$). However, for a geometry in which the calibration factor is a monotonically decreasing function of the crack length, K_I is still decreasing when the mixing ratio reaches 1; and one must go beyond "load control" ($R > 1$) in order to obtain a constant stress intensity factor.

Increasing the mixing ratio beyond 1 reverses the sign of the displacement term in the combined feedback equation (equation 8). This reversal of sign makes the contribution of the displacement term in equation 18 an additive one, so that the command signal now increases as the crack grows as it was expected in order to obtain constant stress intensity factors from a monotonically decreasing calibration factor. However, testing a geometry with a mixing ratio > 1, may degrade the performance of the

loading device. This degradation in performance is due to the decrease in the gain of the equivalent displacement transducer with crack enlargement.

Rewriting equation 10 in the form

$$g_R^u = [1 - R(1 - 1/\gamma\overline{C})]g_u \qquad (10a)$$

and assuming that the d.c. gains were optimized before the testing starts by setting $\gamma\overline{C} = 1$ and thus making the gain of the equivalent transducer independent of the mixing ratio it is clear that the gain of the equivalent transducer will decrease as the crack length increases due to the increase in compliance. The decrease in gain is directly proportional to the mixing ratio and thus, while a loss of performance in the loading device is always present for any non-zero mixing ratio, it is aggravated when the testing geometry requires a mixing ratio > 1. The testing of geometries with monotonically decreasing calibration factors also demands a re-evaluation of the steps required to arrive at equation 17; however, this turns out to be of no consequence since equation 17 becomes invalid only when the gain of the equivalent transducer becomes 0.

In view of these remarks, it is clear that the testing at constant levels of the stress intensity factor using combined feedback involves a trade-off between the amount of crack propagation and the performance of the loading device. The use of this technique demands attention not only to the test geometry but also to the loading device.

6. Conclusions

Using a combined feedback of load and displacement allows the testing of fracture specimens at constant (or nearly constant) stress intensity factors. This technique offers several advantages over previous methods: it is not restricted to any particular specimen geometry; any geometry amenable to analysis where the stress intensity factor increases under constant load can be tested at constant levels of stress intensity factor using the combined feedback. Geometries for which the stress intensity factor decreases with crack propagation can also be employed, but its use requires additional attention to the response and performance of the loading device.

The load is reduced automatically by the specimen as a result from a change in its compliance, which is interpreted as a change in crack length. The load reduction occurs inside the feedback loop in a stepless fashion and at a rate and resolution determined by the response of the displacement transducer, which together with the specimen, act as a crack length measuring device which then changes the load according to the externally prescribed mixing ratio.

The choice of a mixing ratio so that at a particular crack length the stress intensity factor has an extremum, bears resemblance to the tapered compact tension specimen in which the taper angle and the height-to-width ratio are used to control the location of the extremum. The main difference in the calibration factor for the two cases is that in the tapered specimen the calibration factor will eventually grow unbounded as the crack length approaches the width of the specimen, since it is under load control; while under combined feedback, the calibration factor (equation 13) will tend to zero since the compliance in the denominator is growing at a faster rate than the load calibration factor.

7. Acknowledgments

This work was made possible largely through the support of the E.I. DuPont de Nemours Company through initial contact with Dr. Manuel Panar. The authors are also grateful for the support of Caltech's Program in Advanced Technologies, which was sponsored by Aerojet General, General Motors and TRW. In addition some support derived during the final stages of research from ONR grant # N00014-91-J-1427, with Dr. Peter Schmidt as the technical monitor.

8. References

1. S. Mostovoy, P.B. Crosley and E.J. Ripling, *Journal of Materials* 2 (1967) 661-681.
2. R.S. Rivlin and A.G. Thomas, *Journal of Polymer Science* 10 (1953) 291-318.
3. J. Schijve and A.U. De Koning, *Engineering Fracture Mechanics* 9 (1977) 331-340.
4. P. Huculak, *Journal of Testing and Evaluation* 14 (1986) 200-206.
5. S.W. Freiman, D.R. Mulville and P.W. Mast, *Journal of Materials Science* 8 (1973) 1527-1533.
6. J.O. Outwater and D.G. Gerry, *Journal of Adhesion* 1 (1969) 290-298.
7. J.A. Kies and B.J. Clark, *Proceedings of the Second International Conference on Fracture* (Brighton), (1969) 483-491.
8. D.A. Dillard and Y. Bao, *Journal of Adhesion* 33 (1991) 253-271.
9. D. Munz, R.T. Bubsey and J.E. Srawley, *International Journal of Fracture* 16 (1980) 359-374.
10. S.R. Swanson, F. Cicci and W. Hoppe, in *Fatigue Crack Propagation,* American Society for Testing and Materials, (1967) 312-362.
11. J. Zuidema and M. Mannesse, *Engineering Fracture Mechanics* 34 (1989) 445-456.
12. P.S. Nicholson, *Journal of The American Ceramics Society* 73 (1990) 1800-1802.
13. D.A. Dillard, personal communication, (July 1992).
14. J.E. Srawley and B. Gross, *Materials Research and Standards* 7 (1967) 155-162.
15. T.P. Neal, Performance Estimation for Electrohydraulic Control Systems. Technical Bulletin 126, Moog Inc. Controls Division, East Aurora (1974).